Automatic Quantitative Analysis of Pulmonary Vessels in CT: Methods and Applications

Zhiwei Zhai

Colophon

About the cover:

The cover was designed from a tree photo taken in the Japanese Garden, Den Haag, which was made into lung-like shape. The front one is in gray, which looks like a vessel tree in medical images, and the back is in color, expressing the hope that patients suffering from diseases will recover to a colorful life.

Automatic Quantitative Analysis of Pulmonary Vessels in CT: Methods and Applications

Proefschrift

ter verkrijging van

de graad van Doctor aan de Universiteit Leiden,

op gezag van Rector Magnificus prof.mr. C.J.J.M. Stolker,

volgens besluit van het College voor Promoties

te verdedigen op dinsdag, 10 maart, 2020

klokke 11:15 uur

door

Zhiwei Zhai

geboren te Taian Shandong, China in 1989

Promotor: Prof. dr. ir. B. P. F. Lelieveldt

Co-promotor: Dr. ir. B. C. Stoel
                               Dr. ir. M. Staring

Leden promotiecommissie: Prof. dr. M. de Bruijne
                               Erasmus Medical Center, Rotterdam
                               Prof. dr. W. Kraaij
                               Prof. dr. P.E. Postmus

Contents

1

Introduction

1.1   Pulmonary anatomy and respiratory physiology

The human lungs consist of a right and left lung, located in the thoracic cavity on either side of the heart [1]. The right lung, with three lobes, is generally larger than the left, which consists of two lobes. The lungs are surrounded by a thin tissue layer called the pleura. Pulmonary blood vessels and airways pass into the lungs at the root, a central recession called the hilum [2]. Pulmonary blood vessels can be divided into arteries and veins, as shown in Figure 1.1. Pulmonary arteries deliver oxygen-poor blood from heart to the lungs, and the pulmonary veins drain oxygen-rich blood from the lung to the heart. The main pulmonary artery is connected to the right ventricle of the heart by the pulmonary trunk, and branches into the right and left pulmonary artery. There are four main pulmonary veins, two for each lung, connected to the left atrium of the heart. The pulmonary airways, called bronchi, branch out from the trachea into lungs. The bronchi divide into smaller and smaller branches, and eventually end in cluster of small sacs, called alveoli, where gasses are exchanged. The thin layer of cells between the alveoli is called the interstitium, which contains blood vessels and cells that help support the alveoli.

The lungs are the major organs of the respiratory system, and their primary function is gas exchange [1]. With each breath, air first enters the nose or mouth, passes through the larynx and the trachea, and splits into the bronchi. Within the lungs, the bronchial trees deliver the air to the terminals of the alveoli [3]. In the alveoli, oxygen from the air diffuses through the walls of the alveoli into the blood of the pulmonary capillaries. Carbon dioxide, a waste production of the metabolism, transfers from the blood to the alveoli, where it can be breathed out through the airway [4], as shown in Figure 1.2. Oxygenated blood is collected from the capillaries through the pulmonary veins back to the heart, and deoxygenated blood is carried by
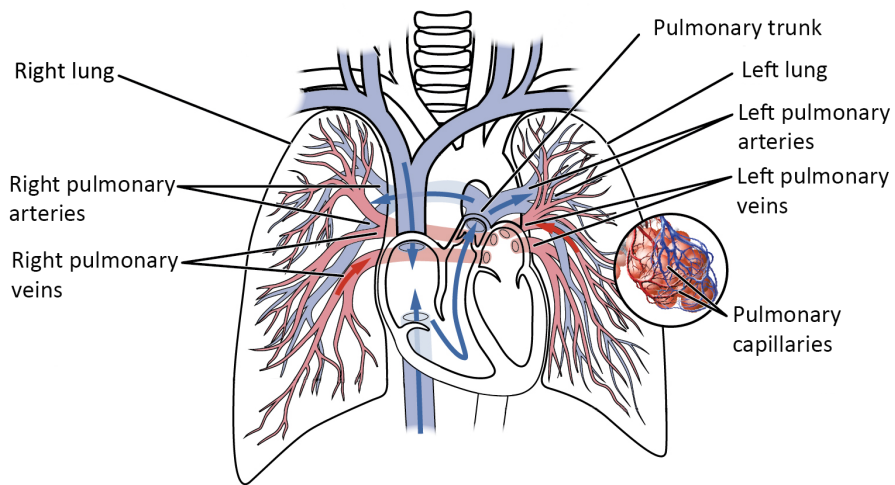
Figure 1.1: Lung anatomy which (modified and adopted from the website of `https://en.wikipedia.org/wiki/File:2119_Pulmonary_Circuit.jpg`)

the pulmonary arteries from the heart to the lungs. This makes the pulmonary blood circulation unique [5]. since blood circulation in all other organs carries oxygenated blood through the arteries and deoxygenated blood through the veins.

1.2 Pulmonary diseases

The lung is an organ with a complex structure, expanding and shrinking thousands times a day, during inhalation and exhalation [6]. The lung can be affected by a variety of diseases in specific parts of the complex system influencing its function. There are several diseases, such as asthma, bronchiectasis, bronchitis and chronic obstructive pulmonary disease, that affect the airways and obstruct gas delivery [7]. Some lung diseases, like pneumonia and asbestosis, could can cause the damage of in alveoli [8]. Various lung diseases, for example interstitial lung disease, affect the interstitium, which is the thin layer between the lungs' alveoli. Diseases, such as pulmonary embolism, pulmonary hypertension and chronic thromboembolic pulmonary hypertension, affect the pulmonary blood vessels. Gas exchange and blood circulation can be influenced by damage in any structure of the lungs. Two diseases that can affect the lungs have a special focus in this thesis: systemic sclerosis and chronic thromboembolic pulmonary hypertension.

Systemic sclerosis (SSc) is an autoimmune connective tissue disease that can involve multiple organs, including skin, musculoskeletal, pulmonary, renal and other complications [9]. Pulmonary disease, which is the leading cause of mortality in patients with SSc [10], mainly consist of interstitial lung disease (ILD) and pulmonary
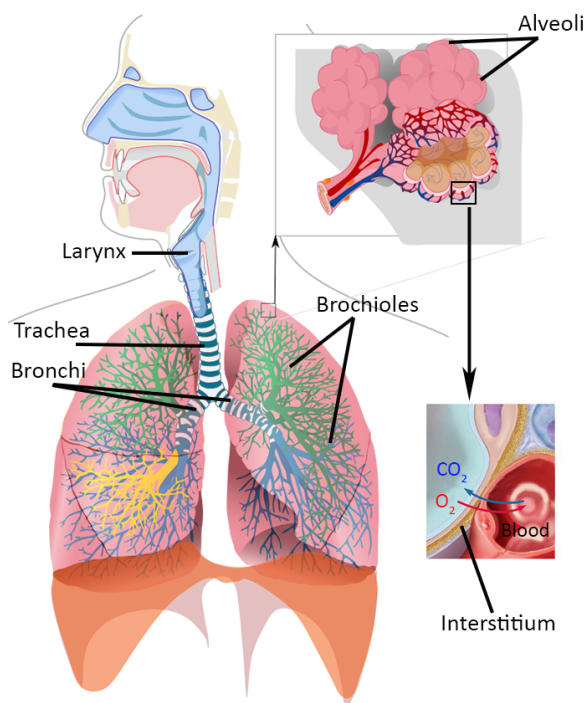
Figure 1.2: Respiratory physiology (modified and adopted from `https://commons.wikimedia.org/wiki/File:Respiratory`

hypertension (PH) [11]. In SSc-related ILD, structural changes in the parenchyma, i.e. fibrosis, is known to affect pulmonary function. For assessing ILD, pulmonary function tests, such as diffusion capacity for carbon monoxide (DLCO) and forced vital capacity, and high-resolution chest computed tomography (HRCT) are commonly used. PH is characterized by abnormally high blood pressure in the pulmonary vessels, which can cause remodeling of pulmonary arteries [12]. In SSc-related PH, DLCO decreases years before diagnosis of PH [13]. Conversely, gas transfer can be mildly or moderately impaired in the absence of detectable pulmonary fibrosis and pulmonary hypertension.

Chronic thromboembolic pulmonary hypertension (CTEPH) is characterized by the occurrence of unresolved thromboembolism undergoing fibrotic organization [14], which is caused by persistent obstruction of pulmonary arteries after pulmonary embolism [15]. The mechanical obstruction of pulmonary arteries is produced by fibrotic transformation of pulmonary thrombius, which canould lead to pulmonary hypertension and increasing pulmonary vascular resistance (PVR) [16]. CTEPH patients have poor prognoses: 2-years survival rate is 20% in patients with mean

3

pulmonary artery pressure higher than 50 mmHg [17, 18, 19]. The prognosis can be improved by pulmonary endarterectomy [20] or balloon pulmonary angioplasty (BPA) [21], combined with optimal medication. Pulmonary endarterectomy is a curative treatment for CTEPH, leading to nearly normalized hemodynamics in the majority of patients [22]. However, for patients with inoperable CTEPH, BPA can be an alternative treatment to improve the clinical status and hemodynamics with a low mortality [23].

1.3 Clinical measurements for assessing SSc and CTEPH

Evaluation of the disease severity and assessment of treatment effects play an important role in the diagnosis and therapy of any disease. The higher risk patients, who may benefit from treatment, could be selected by accurate prognostic evaluation [11, 24]. There are several clinical measurements for evaluating the severity of diseases and response to treatment, such as 6-minute walk distance, pulmonary function tests, invasive right-sided heart catheterization (RHC) and chest computed tomography (CT).

Pulmonary function tests, such as the diffusion capacity for carbon monoxide (DLCO) and force vital capacity (FVC), are key measures for evaluating the response to treatment of interstitial lung disease [25]. DLCO is a measurement of the extent of gas transfer in the lungs. As the affinity and absorption capacity of red blood cells for carbon monoxide (CO) is strong, gas uptake by the capillaries are less dependent on cardiac output [26]. Generally DLCO is measured in 'ml/min/mmHg', which involves measuring the rate of CO uptake (ml/min) divided by the alveolar pressure (mmHg). FVC (L) which is the volume of air that can forcibly be expired after full inspiration, as demonstrate in Figure 1.3 (b) [27]. The FVC can be influenced by many factors, including body mass index (BMI), physical condition, and smoking status. FVC can be compared to the normal value standardized for age, sex, height, etc. For follow-up studies the raw FVC measurements are used to compare with previous measurements to determine whether a pulmonary condition improved or deteriorated.

Right heart catheterization (RHC) is the gold standard for measuring the pulmonary artery pressure (PAP) [28]. For monitoring the right sided pressure, a catheter is inserted into the pulmonary artery. The hemodynamic parameters are examined via RHC, including (systolic, diastolic and mean) PAP, systolic right ventricular pressure, right atrial pressure, cardiac output, cardiac index and pulmonary capillary wedge pressure [16]. According to the European society of cardiology (ESC) guideline on diagnosis and treatment of PH, RHC is the diagnostic gold standard for pulmonary hypertension (PH), defined by a mean PAP $\geq$ 25 mm Hg [29, 30]. In evaluating the severity of CTEPH and assessing treatment effects, the invasive RHC serves as the standard criterion [31].

4
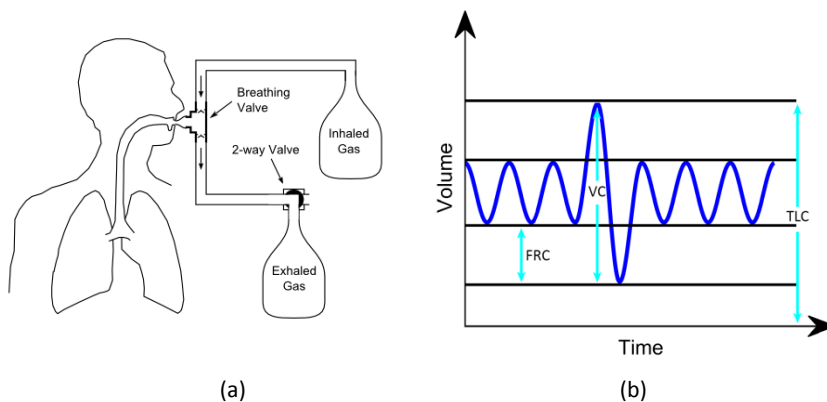
Figure 1.3: (a) DLCO test (adopted from `https://www.pftforum.com/blog/`), (b) breathing curve, VC is vital capacity, TLC is total lung capacity and FRC is functional residual capacity.
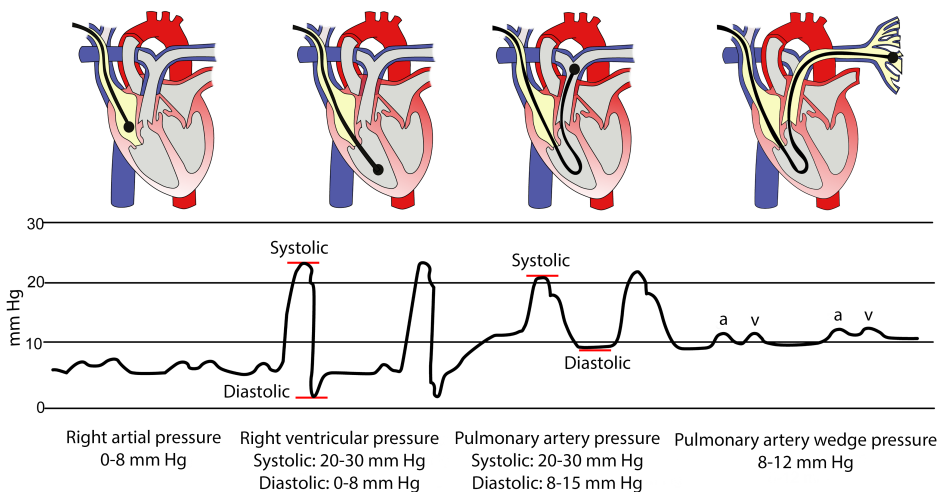
Figure 1.4: Illustration of right heart catheterization. The normal pressure waves with normal value is demonstrated, which is measured at the pulmonary artery during right heart catheterization. (adopted and modified from `https://www.pcipedia.org/wiki/Right_heart_catheterization`
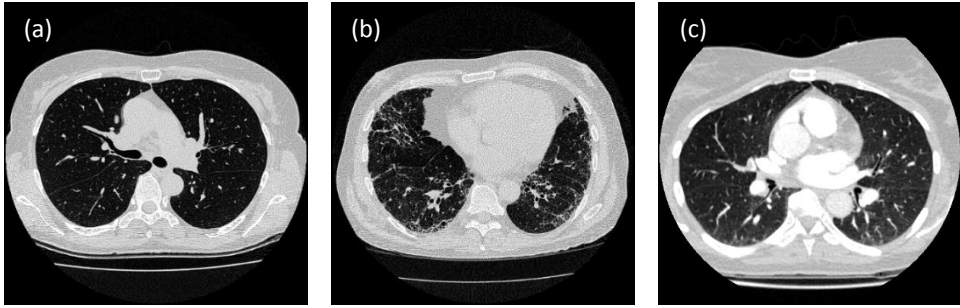
Figure 1.5: Slices of HRCT scans from a normal case (a), a patient with ILD (b), and a slice of CTPA from a patient in CTEPH.

1.4   Chest CT

Currently, non-invasive imaging techniques play a key role in both diagnosis the lung diseases and assessment of treatment effects [11, 32, 33]. High-resolution computed tomography (HRCT) of the chest is considered the most accurate imaging method for assessing ILD [25]. Computed tomography pulmonary angiography (CTPA) is used in diagnosis and evaluation the severity of CTEPH [34]. A chest CT scan, which is a more detailed type of chest X-ray, takes many projections of lungs, and a computer can combine these projections to create three-dimensional cross-sectional images to show the organs' size, shape, and structures. CT allows imaging of the entire chest during a single breath hold [35]. The multiple parallel rows of x-ray detector of CT scanners increases from 4, 16, 64 to 320.

Dual-energy CT can be performed with a dual-source scanner or with a single-source scanner with fast kilovoltage switching [36], which has ushered in the ability of material differentiation and tissue characterization beyond the traditional CT [37]. Radiographic contrast agents, such as injected iodine media or inhaled xenon gas, can be specified at two different energies, subsequently, the specific content of contrast agents in tissues can be visualized and quantified in the dual-energy CT [38]. Both anatomical and functional information about the lungs can be provided with dual-energy CT, in a variety of pulmonary diseases. Applications in the thorax, including detection and prognostication of acute or chronic pulmonary embolism (PE), and characterization of parenchymal disease, benefit from this imaging technique [37, 19, 39].

1.5   Outline of the thesis

With the development of CT scanners, nowadays, a high-resolution CT scan may contain around 500 slices, which significantly improves the accuracy of diagnosis. However, the huge amount of data from CT obviously increases the diagnostic

workload for clinicians and is difficult to interpret in some cases, e.g. SSc patients without fibrosis in CT who still suffer from impaired gas transfer, and CTEPH patients with CTPA before and after treatment are difficult to quantify objectively by clinicians. Therefore, developing automatic computer aided methods is important in order to investigate pathology of pulmonary vascular diseases and quantitatively assess treatment effects.

The aim of this thesis is to develop these methods focusing on quantifying pulmonary vascular diseases and assessing treatment effects, based on CT images. Particularly, the following objectives have been pursued in this thesis: 1) to develop an accurate lung vessel segmentation method; 2) to propose and validate an automatic method for quantifying pulmonary vascular morphology; 3) to investigate pulmonary vascular remodeling in SSc patients with impaired DLCO, but in the absence of pulmonary fibrosis; 4) to investigate changes in the pulmonary vascular densitometry and morphology in patients with CTEPH, treated with BPA. These objectives are described in this thesis, with the following structure:

Chapter 2 presents a method for extracting lung vessels, based on graph-cuts, where the appearance and shape features are combined into a newly designed cost function. To cope with memory requirements of a graph representation for voxels in chest CT, an efficient strategy was proposed by extracting sparse graphs with a low threshold and generating an adjacency matrix with diagonal vector assignments.

In **Chapter 3** an automatic method is proposed and validated, for the quantification of pulmonary vascular morphology in CT images. The proposed method consists of pulmonary vessel extraction and quantification, where the vessel extraction method from Chapter 2 was extended, by incorporating CT intensity, vesselness and the distance map to airways, and the quantification method is based on a radius histogram analysis. The proposed method was validated with a public data set, a data set of a 3D-printed vessel phantom and a clinical data set.

Chapter 4 investigates the association between pulmonary vascular morphology and gas exchange in patients in systemic sclerosis without lung fibrosis. Pulmonary vessels were detected and quantified automatically in CT images, and subsequently two images biomarkers (α and β) were calculated, where α reflects the relative contribution of small vessels compared to large vessels and β represents the vessel tree's capacity. The correlations between imaging biomarkers and gas transfer (DLCO) were evaluated with Spearman's correlation.

Chapter 5 presents a method for visualizing and quantifying changes in pulmonary perfusion by automatically comparing CTPA before and after BPA treatment. Fourteen CTEPH patients were involved in the study, who underwent CTPA and RHC, before and after BPA treatment. The quantification of perfusion changes was validated against hemodynamic changes.

In **Chapter 6** a method is proposed for quantifying morphological changes, which consists of three processing steps: constructing vascular trees from the detected pulmonary vessels, matching vascular trees with preserving local tree topology and quantifying local morphological changes based on Poiseuille's law. The vascular tree matching method was validated with a data set of synthetic trees and the relation between the quantification of morphological changes and clinical RHC parameters was investigated in CTEPH patients.

Chapter 7 summarizes and discusses the overall achievements of this thesis.

2

Lung vessel segmentation in CT images using graph-cuts

This chapter was adapted from:

Abstract

Accurate lung vessel segmentation is an important operation for lung CT analysis. Filters that are based on analyzing the eigenvalues of the Hessian matrix are popular for pulmonary vessel enhancement. However, due to their low response at vessel bifurcations and vessel boundaries, extracting lung vessels by thresholding the vesselness is not sufficiently accurate. Some methods turn to graph-cuts for more accurate segmentation, as it incorporates neighbourhood information. In this work, we propose a new graph-cuts cost function combining appearance and shape, where CT intensity represents appearance and vesselness from a Hessian-based filter represents shape. Due to the amount of voxels in high resolution CT scans, the memory requirement and time consumption for building a graph structure is very high. In order to make the graph representation computationally tractable, those voxels that are considered clearly background are removed from the graph nodes, using a threshold on the vesselness map. The graph structure is then established based on the remaining voxel nodes, source/sink nodes and the neighbourhood relationship of the remaining voxels. Vessels are segmented by minimizing the energy cost function with the graph-cuts optimization framework. We optimized the parameters used in the graph-cuts cost function and evaluated the proposed method with two manually labeled sub-volumes. For independent evaluation, we used 20 CT scans of the VESSEL12 challenge. The evaluation results of the sub-volume data show that the proposed method produced a more accurate vessel segmentation compared to the previous methods, with F1 score 0.76 and 0.69. In the VESSEL12 data-set, our method obtained a competitive performance with an area under the ROC curve of 0.975, especially among the binary submissions.

2.1 Introduction

Lung vessel detection is a key research topic in pulmonary CT image processing, since accurate vessel segmentation is an important step in extracting imaging bio-markers of vascular lung diseases. For example, systemic sclerosis (SSc) is related to pulmonary hypertension (PH) [40], which is related to narrowing of the small vessels, and therefore vessel analysis could be used as an imaging bio-marker for PH analysis in SSc. A few methods have been proposed for lung vessel segmentation. According to the VESSEL12 challenge [41], Hessian-based methods are popular and perform well in lung vessel enhancement. Hessian-based filters, such as the Frangi filter [42] and Sato filter [43], enhance tube-like structures by modeling the eigenvalues of the Hessian matrix with cylindrical properties. However, these filters tend to give a low response at the vessel bifurcations and at the vessel boundaries. In our previous work, a strain energy filter [44] overcomes the problem in detecting bifurcations to some degree by analyzing the shape-tuned strain energy density. However, thresholding the strain energy filter's vesselness does not provide accurate binary results either. In order to improve vessel segmentation, we turn to graph-cuts where we can more easily combine different sources of information via the cost function, and additionally include neighboring information.

Graph-cuts methods consider the segmentation a labeling problem [45, 46, 47]. The voxel nodes are labeled to object or background, according to nodes neighbor connections and their weights [48]. Several approaches using graph-cuts for vessel segmentation have been proposed. Chen et al. [49] proposed a regional graph-cuts based method for liver vessel segmentation with quick shift clustering for initialization. Bauer et al. [50] proposed a tube detection filter for a rough vessel segmentation, then the shape prior from centerline and radius of the initial vessel trees were used to constrain the graph-cuts. Freiman et al. [51] proposed a graph-cuts based method for carotid artery segmentation by coupling Frangi's vesselness and intensity into cost function. In order to cope with memory and computational challenges, they divided the scan volume into several block regions with a small overlap, computed graph-cuts for each block independently, and merged the binary segmentations results.

In this paper, an automatic lung vessel segmentation method is proposed based on graph-cuts. The Hessian-based strain energy filter is adopted to enhance vessels. A conservative threshold is applied on the vesselness to label voxels that are certainly part of the background, the remaining voxels are included as nodes in the graph. Instead of using vesselness as the vessel data cost term directly [51], we take it as a shape feature and compute the vessel data term with prior distribution. CT intensity represents appearance. Combining appearance and shape, the cost function is calculated. To deal with memory requirements of graph structure representations, we removed those

11

voxel nodes that are considered clearly background and employed a low overhead sparse matrix implementation to record the remaining voxel nodes neighborhood connections and their weights. After the graph structure is established, the graph-cuts optimization framework is applied for vessel segmentation. The proposed lung vessel segmentation method was optimized and evaluated on two manually labeled sub-volumes and evaluated independently on the VESSEL12 challenge data-set.

2.2 Methods

Our segmentation method consists of three steps: 1) application of the strain energy filter for lung vessels enhancement, 2) construction of the graph structure representation, and 3) vessels segmentation based on graph-cuts.

2.2.1 Vessel enhancement filter

The response of traditional Hessian-based vesselness filters is low at the vessel bifurcations and boundaries, due to an overly simplified cylindrical model. The strain energy filter, which is based on strain energy density theory from solid mechanics, aims to remedy this. The Hessian matrix is considered a stress tensor, and three tensor invariants (measures) can be derived from orthogonal tensor decomposition, each measuring an independent descriptor of material distortion. Turning to images, they can be used to formulate distinctive functions for shape discrimination, brightness contrast and structure strength. Based on an intensity continuity assumption, and a relative Hessian strength measure to ensure the dominance of second-order over first-order derivatives to suppress undesired step edges, the final vesselness was calculated as follow:

$$\varphi(\sigma, x) = \begin{cases} 0, & \text{if } \frac{1}{3}(\lambda_1 + \lambda_2 + \lambda_3) > -\zeta \lambda_m \\ \exp\left(-\eta \frac{\|\nabla I\|}{\lambda_m}\right) V^\kappa(x) \rho(H, \nu), & \text{otherwise,} \end{cases} \tag{2.1}$$

in which σ is scale, λ_i are the eigenvalues with λ_m the maximum eigenvalue, $\lambda_1 + \lambda_2 + \lambda_3$ is the brightness contrast term, $\frac{\|\nabla I\|}{\lambda_m}$ measures relative Hessian strength, $V^\kappa(x)$ is a measure for vessel shape and $\rho(H, \nu)$ measures structure strength. The parameters $0 < \zeta < 1, \eta > 0, \kappa > 0$ and $-1 < \nu < 0.5$ are user-defined. More details can be found in the original paper [44].

2.2.2 Graph representation

For high resolution pulmonary CT scans, there are around 500 slices per patient with 512*512 voxels per slice. Even when only considering the lung region for computing, the graph would consist of almost ten million nodes and hundred million edges (26-connectivity in a 3D grid). To cope with memory requirements, previous works used a block region strategy [49, 51]. However, this introduces discontinuities in the merged part of detected vessel. Therefore we used an alternative method to reduce the graph
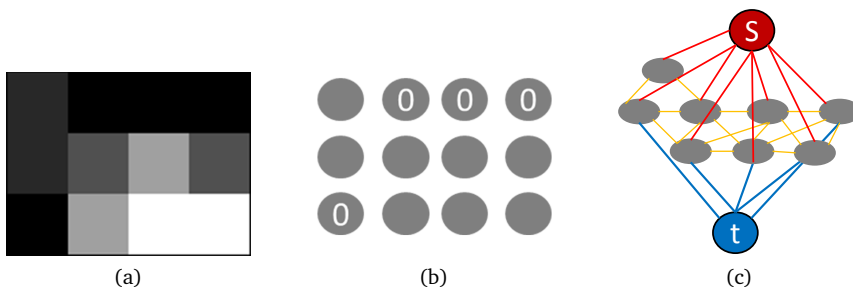
Figure 2.1: Graph structure representation of this method, (a) original image, (b) pre-labeling the background with the threshold strategy, (c) graph structure construction of the remaining voxel nodes.

size by a thresholding strategy. As illustrated in Figure 2.1a, there are several voxels with lowest gray values that are certainly part of the background. Then, we can use a low threshold to label these voxels as background, see Figure 2.1b. The graph structure can be established using the remaining voxels (unlabeled voxels).

In Figure 2.1c, the nodes of the graph consist of the remaining voxels, source and sink nodes. The edges between the source/sink node and voxel nodes are called t-edges and the edges between neighboring voxel nodes are n-edges. The t-edges and their weights can be represented easily with a dense matrix. For the n-edges, a sparse matrix was adopted to record the adjacent connections and their weights. If we use 1 and 0 to represent the relationship 'adjacency' and 'non-adjacency' of the voxels respectively, all the 1s locate in several diagonals of the sparse adjacency matrix. The sparse adjacency matrix can be determined memory efficiently by assigning the diagonal vectors. The diagonal vectors can be generated easily by analyzing the type of adjacency. Then, the n-edge's adjacency matrix can be extracted from the whole 3D grid sparse adjacency matrix with the remaining voxels' indices.

To illustrate the sparse adjacency matrix analysis method, we take a 3 by 4 2D image as an example and only consider 4-connectedness. For 4-connectedness, there are only two types of adjacency (if considering adjacency with direction, there would be four types of adjacency), up-down adjacency and left-right adjacency, see Figure 2.2b. Taking the up to down adjacency, the sparse matrix can be generated efficiently by assigning the single diagonal with one vector. The vector can be determined by a rule that the $(k \times 3)$th element is zero. The left to right adjacency sparse matrix can be calculated in a similar way. After combining these two sparse adjacency matrices, and making the combined matrix symmetric, so that the down to up adjacency and right to left adjacency are included, we obtain the final sparse adjacency matrix, Figure 2.2c. For a 3D image, the calculation of a sparse adjacency matrix is similar.

	1	2	3	4	5	6	7	8	9	10	11	12
1	0	1	0	1	0	0	0	0	0	0	0	0
2	1	0	1	0	1	0	0	0	0	0	0	0
3	0	1	0	0	0	1	0	0	0	0	0	0
4	1	0	0	0	1	0	1	0	0	0	0	0
5	0	1	0	1	0	1	0	1	0	0	0	0
6	0	0	1	0	1	0	0	0	1	0	0	0
7	0	0	0	1	0	0	0	1	0	1	0	0
8	0	0	0	0	1	0	1	0	1	0	1	0
9	0	0	0	0	0	1	0	1	0	0	0	1
10	0	0	0	0	0	0	1	0	0	0	1	0
11	0	0	0	0	0	0	0	1	0	1	0	1
12	0	0	0	0	0	0	0	0	1	0	1	0
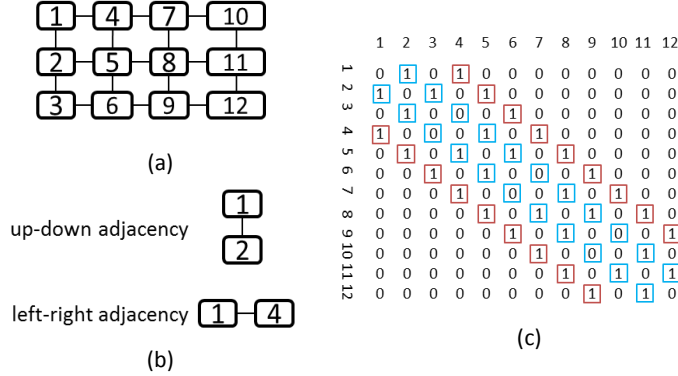
Figure 2.2: 2D image sparse adjacency matrix, (a) is a 3 by 4 2D matrix with the value of the voxel index inside, (b) is the adjacency type analysis, (c) is the sparse adjacency matrix of the 2D image.

2.2.3   Proposed cost function for the graph-cuts

In this work, we present a method for lung vessel segmentation based on graph-cuts, by combining appearance and shape features. Segmentation is treated as a labeling problem, solved by graph-cuts $L = \{L_p | p \in \mathscr{P}\}$. The energy function of a labeling problem can be optimized by finding the max-flow/min-cut algorithms [46]. The energy function of our method is:

$$E(L) = \sum_{p \in \mathscr{P}} \left(w D_p^{CT}(L_p) + (1-w) D_p^{vsl}(L_p) \right) + \gamma \sum_{(p,q) \in \mathscr{N}, L_p \neq L_q} V_{p,q}(L_p, L_q), \tag{2.2}$$

where the data term consists of appearance (CT intensity) $D_p^{CT}(L_p)$ and shape (vesselness) $D_p^{vsl}(L_p)$) and w is a weight balancing the two parts. $V_{p,q}(L_p, L_q)$ is the cost function for cutting the edge (p, q) and γ is a user-defined positive coefficient for adjusting the smoothness.

Commonly Gaussian functions are used in the data term [51], but this would cause voxels with high intensity or vesselness, i.e. far away from the center of the Gaussian distribution, to obtain a low vessel probability. Therefore we employed a sigmoid function for both the appearance term and the shape term. So, voxels with high a intensity or vesselness obtain a high vessel likelihood, as follows:

$$D_p^{CT}(I_p|L_p = l) = \frac{1}{1 + e^{-\alpha_l^{CT}(I_p - \beta_l^{CT})}} \tag{2.3}$$

$$D_p^{vsl}(I_p|L_p = l) = \frac{1}{1 + e^{-\alpha_l^{vsl}(I_p - \beta_l^{vsl})}}. \tag{2.4}$$

The choice for the free parameters of the sigmoid function in Equation (2.3) and (2.4), is given in Sec. 2.3.1. The cost function $V_{p,q}(L_p, L_q)$ for the n-edge (p, q) is calculated based on the similarity in appearance of two voxels nodes $p\ q$, and weighted by their spatial distance:

$$V_{p,q}(L_p, L_q) = \begin{cases} e^{-|I_p - I_q| \cdot dist(p,q)}, & \text{if } L_p \neq L_q \quad \text{and} \quad (p,q) \in \mathcal{N} \\ 0, & \text{otherwise} \end{cases} \tag{2.5}$$

If two nodes of the n-edge (p, q) have similar appearance but are labeled differently, the boundary cost of this n-edge will be high, weighted by the spatial distance of nodes p and q.

2.3 Experiments and results

This work were implemented in Matlab for the graph structure construction and mixed with C++ for the cost function optimization, which is benefiting from GCmex 1.9 ([1]). The source code of the vessel enhancement filters is publicly available via the toolkit ITKTools ([2]), see the tool pxenhancement. The entire processing pipeline was designed in MeVisLab 2.7.1 (VC12-64). The runtime of the proposed method for a typical $400 \times 512 \times 512$ size 3D CT image is around 650s on our computer, configured with a 2.67 GHz CPU, 24 GB memory and a 64-bit Windows 7 operating system.

2.3.1 Parameter estimation

The parameters used in the strain energy vesselness filter were set according to the literature [44]: $\zeta = 0.5$, $\eta = \kappa = 0.2$, $\nu = 0.0$, and using scales $\sigma \in \{1, 2, 3\}$. After construction of the graph structure, the parameters in the graph-cuts energy function were trained with sub-volume data which was labeled by an expert. More details about the sub-volume data can be found in Sec. 2.3.2. Due to the complex structure of the vessel trees, the smoothness parameter γ was set to 0.01. After optimizing

---

[1]http://www.wisdom.weizmann.ac.il/~bagon/matlab_code/GCmex1.9.tar.gz
[2]https://github.com/ITKTools/ITKTools

on the training data, the appearance and shape balance parameter w in the data term was set to 0.6. For the parameters of the sigmoid function in the data term, we designed an algorithm to estimate them automatically. Before estimation, we removed voxels that had high vesselness or intensity, because these voxels can affect the parameters estimation severely. Afterwards, the mean value was taken as the initial threshold to separate the initial background and foreground. The Gaussian distribution of the intensity of the foreground can be estimated by calculating the mean μ and the standard deviation std. Then, we fitted the sigmoid function to the Gaussian function in the way that $Sigmoid(\beta) = Gaussian(\beta) = 0.5$. For estimating the fuzziness parameter α we did several experiments and finally found that the best fitting curve was obtained by: $Sigmoid(\mu) = 0.95$. So, all the parameters used in the sigmoid function for the foreground intensity term are estimated, and the parameters used in the cost function for the vesselness term can be calculated similarly.

2.3.2 Data and results

Clinical image data was acquired of two patients on a Toshiba Aquilion 16 detector row CT scanner without contrast media. Due to the complexity of the pulmonary vessel trees, it is unrealistic to manually extract the entire vessel trees. In order to evaluate the proposed lung vessel segmentation method, we chose two sub-volumes on the boundary of pulmonary lobes, where the bright plane-shaped fissure and plenty of vessel details make it a challenging detection task. Subsequently, a technical expert and a pulmonologist were asked to manually label the data, using the interactive tools of ITK-snap [52]. In total, two reference segmentations, Data1 with size 65*60*120 and Data2 with size 91*70*121, were extracted. The original CT and extracted sub-volume region of Data1 is shown in Figure 2.3.

Centerline-based evaluation was applied to these two sub-volumes. The vessel centerlines were extracted from the binary masks using a skeletonization method based on the distance transform [53]. As shown in Figure 2.4, the centerline of the segmentation result was compared with the centerline of the reference standard. If the distance between the voxels on the two centerlines are less than the vessel radius at that point, i.e. the voxels on the segmentation centerline fall inside the reference standard vessel region, they would be counted as true positive. The number of false negatives was calculated by the number of voxels on the reference standard centerline minus the number of true positives. The number of false positives was calculated using the number of voxels on segmented centerlines minus the number of true positives, i.e. the number of voxels falls outside the vessel regions of the reference standard. The $precision = TP/(TP + FP)$ and $recall = TP/(TP + FN)$ were calculated, and the $F1$ score, $2\frac{precision*recall}{precision+recall}$, was taken as the main evaluation measurement. We compared the performance of the proposed graph-cuts vessel segmentation method with the
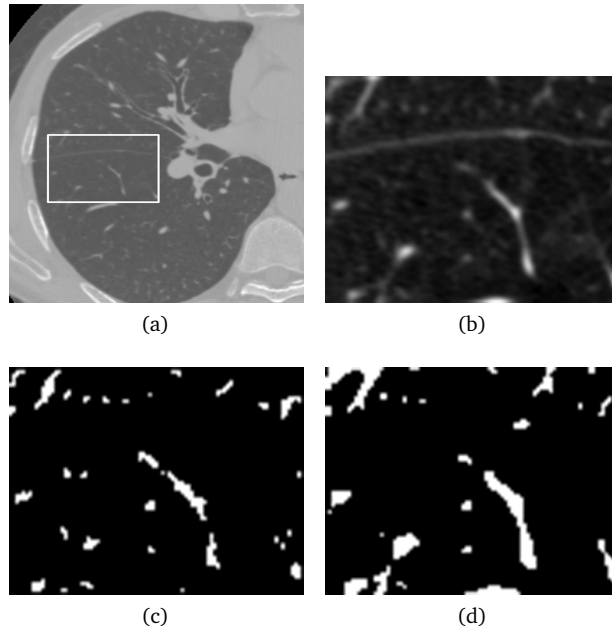
Figure 2.3: Segmentation result on a reference region, (a) reference region in the CT, (b) one slice of the extracted region, (c) manually segmented reference standard, (d) segmentation result of the proposed method.
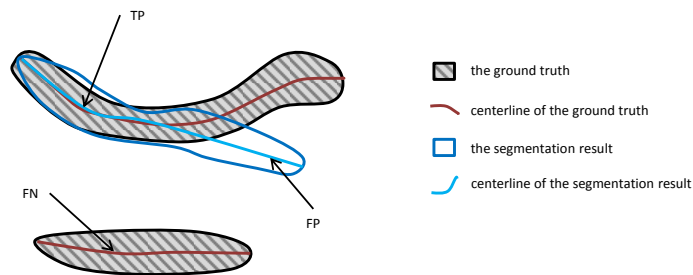
Figure 2.4: Centerline-based evaluation method.

result from thresholding the Frangi's vesselness [42], thresholding the strain energy filter's vesselness [44] and the Freiman's based method [51]. For the optimization of the threshold-based vesselness methods, 70 thresholds ranging from the minimum to the maximum vesselness were used and the best evaluation result was selected. For the Freiman's based method, we implemented the method according to the literature [51] and optimized the parameters with the sub-volume Data1. The evaluation results are shown in Table 2.1. According to the evaluation results, our proposed method achieved a better segmentation.

17

Table 2.1: Evaluation results of methods on reference standard data sets

Methods		Data1			Data2		
Enhancement	binarization	Recall	Precision	**F1 score**	Recall	Precision	**F1 score**
Frangi [42]	threshold	0.7344	0.5082	0.6007	0.6285	0.5147	0.5660
Freiman's method [51]	graph-cuts	0.8233	0.4781	0.6048	0.6428	0.4868	0.5541
Strain energy [44]	threshold	0.7082	0.7287	0.7183	0.6223	0.7119	0.6641
Strain energy	graph-cuts	0.7331	0.7917	**0.7613**	0.6673	0.7145	**0.6901**

Table 2.2: Evaluation results of the VESSEL12 data-set: Az score, Specificity and Sensitivity of our submission across all categories. (Categories 1: Principal, 2: Small Vessels, 3: Medium Vessels, 4: Large Vessels, 5: Vessel/Airway Wall, 6: Vessel/Dense Lesion, 7: Vessel/Mucus-filled bronchi, 8: Vessel-in-lesion/Lesion, 9: Vessel/Nodules).

	1	2	3	4	5	6	7	8	9
Az	0.975	0.953	0.977	0.993	0.867	0.481	0.331	0.661	0.238
Spe	0.910	0.865	0.910	0.979	0.588	0.239	0.112	0.451	0.038
Sen	0.929	0.966	0.953	0.960	0.929	0.929	0.929	0.829	0.929

Az, for area under ROC cure; Spe, for specificity; Sen, for sensitivity.

For an independent evaluation, we used the VESSEL12 challenge data-set, which consists of 20 anonymized CT scans from three hospitals [41]: University Medical Center Utrecht, the University Clinic of Navarra and Radboud University Nijmegen Medical Center. The scans have been selected such that in approximately half of the scans contrast agent was used. About half of the scans contained abnormalities such as nodules, emphysema or pulmonary embolisms. The CT scan size was around $512*512*400$, with voxel size around $0.7*0.7*0.7 mm^3$. This represents a variety of CT scanner types and image acquisition settings, and a wide range of clinical images. The scan data and lung masks were provided by the organizers. The manual labeling was performed on pre-generated points, and only those points were kept when the labels from three independent observers were the same. There were nine categories in the reference standard to perform a comprehensive evaluation of vessel segmentation. The vessel segmentation result from the participating algorithms were evaluated against the manually annotations.

For our study, we downloaded the CT scans and lung mask data, we applied the graph-cuts vessel segmentation, after shape feature extracting with the strain energy filter. We submitted our binary segmentation results to the VESSEL12 organizers, and the organizers made the independent evaluation and sent the evaluation results to us. Our method obtained an area under the ROC curve (Az) of 0.975 score, which is a competitive performance on VESSEL12, especially among the binary submissions. The evaluation results of our method is shown in Table 3.1. The evaluation results of the other submissions can be found in the VESSEL12 study paper [41] and the VESSEL12 website `http://vessel12.grand-challenge.org`.

2.4 Conclusion and discussion

A graph-cuts based segmentation method was proposed to extract the pulmonary vessels in thoracic CT images. By combining appearance and shape features, a new cost function was designed. An efficient strategy was adopted to cope with

the memory requirements of a graph representation. We performed training and evaluation with own sub-volume data, and independently evaluated our method with the VESSEL12 challenge data. From the evaluation results, the proposed method obtained a competitive performance.

From the results on the in-house data, see Table 2.1, the F1 score of our method was higher than the threshold-based vesselness methods and the Freiman's based method. The performance of strain energy filter was better than Frangi's filter, which has been reported in literature [44], and we reproduced the previous results. The Freiman's based method was not a lot better than the threshold-based Frangi's method. This is likely caused by the fact that the Freiman's based method uses a Gaussian as a cost function. This means that high intensity and vesselness values produce low vessel likelihood, which may cause under-segmentation. Additionally, the Freiman's based method does not use a parameter to balance between appearance and shape features. In our method, we designed a new cost function in the graph-cuts for vessels segmentation, which is better than the threshold-based strain energy method. In general, the graph-cuts could perform better than the thresholding, but one should be careful with designing this, since the graph-cuts may give poorer results by a suboptimal choice of cost function (as seen in Data2 in Table 2.1). From the results on the VESSEL12 data (Table 3.1), the proposed method obtained a good performance on the overall categories 1-4. However, the segmentation method did not perform very well in distinguishing airway walls from vessels (category 5), because some airway walls had similar intensities as vessels and parts of the airway walls were attached to the pulmonary artery. The lower score in category 7 was caused by mucus-filled bronchi that have similar appearance and shape features as vessels. To compensate for this, a separate algorithm would be needed for detecting the bronchial tree and extending this tree by mucus-filled bronchi, to be used as an exclusion method. Because in categories 6, 8 and 9, lesions and nodules are mostly attached to vessel trees, the graph-cuts method was not able to separate them from vessel trees. For the other participating methods in the VESSEL12, distinguishing these bronchi, lesions and nodules were also challenges for pulmonary vessel segmentation. Comparing with the other submissions, we obtained a competitive score, which was the highest compared to the other binary submissions. This method could be improved by combining more information in the data term, such as a distance map to vessel centerlines of initial segmentation, and designing a more precise boundary cost function with multiple features.

Acknowledgment

3

Automatic quantitative analysis of pulmonary vascular morphology in CT images

Abstract

Purpose Vascular remodeling is a significant pathological feature of various pulmonary diseases, which may be assessed by quantitative CT imaging. The purpose of this study was therefore to develop and validate an automatic method for quantifying pulmonary vascular morphology in CT images.

Methods The proposed method consists of pulmonary vessel extraction and quantification. For extracting pulmonary vessels, a graph-cuts based method is proposed which considers appearance (CT intensity) and shape (vesselness from a Hessian-based filter) features, and incorporates distance to the airways into the cost function to prevent false detection of airway walls. For quantifying the extracted pulmonary vessels, a radius histogram is generated by counting the occurrence of vessel radii, calculated from a distance transform based method. Subsequently, two biomarkers, slope α and intercept β, are calculated by linear regression on the radius histogram. A public data set from the VESSEL12 challenge was used to independently evaluate the vessel extraction. The quantitative analysis method was validated using images of a 3D printed vessel phantom, scanned by a clinical CT scanner and a micro-CT scanner (to obtain a gold standard). To confirm the association between imaging biomarkers and pulmonary function, 77 scleroderma patients were investigated with the proposed method.

Results In the independent evaluation with the public date set, our vessel segmentation method obtained an area under the ROC curve of 0.976. The median radius difference between clinical and micro-CT scans of a 3D printed vessel phantom was (0.062±0.020 mm), with interquartile range of (0.199±0.050 mm). In the studied patient group, a significant correlation between diffusion capacity for carbon monoxide and the biomarkers, α (R=-0.27, p-value=0.018) and β (R=0.321, p-value=0.004), was obtained.

Conclusion In conclusion, the proposed method was highly accurate, validated with a public data set and a 3D printed vessel phantom data set. The correlation between imaging biomarkers and diffusion capacity in a clinical data set confirmed an association between lung structure and function. This quantification of pulmonary vascular morphology may be helpful in understanding the pathophysiology of pulmonary vascular diseases.

3.1 Introduction

Pulmonary vascular remodeling is a significant characteristic of pulmonary diseases, such as chronic obstructive pulmonary disease, interstitial lung disease (ILD), and pulmonary hypertension (PH) [54, 55, 14, 56, 57, 12, 29, 58]. Systemic sclerosis (SSc, also called scleroderma), is an autoimmune connective tissue disease affecting several organs, and its pulmonary involvement can cause ILD or PH, which may involve pulmonary vascular alterations [25, 59]. Pulmonary vascular alterations have been described as narrowing and pruning of distal vessels, which increases vascular resistance and cause hypertension [60, 61, 62]. The dilation of proximal vessels is also an essential morphological feature, as increasing pulmonary vascular resistance affects proximal vessels [63]. Investigation of changes in pulmonary vascular morphology, such as pruning of small vessels or dilation of large vessels, may provide assessments of pulmonary vascular remodeling.

Some studies based on the analysis of computed tomography (CT) images have shown promising results for quantifying pulmonary vascular remodeling in pulmonary diseases, using different approaches. Matsuoka et al. [12, 60] introduced a CT measurement by quantifying the 2D cross-sectional area of small pulmonary vessels for assessing vessel pruning of COPD. Estepar et al. [64, 62] extended the pruning measurement into 3D by quantifying the volume ratio between small vessels and the total vessels, and applied these measurements within each lobe. Rahaghi et al. [65, 63] introduced the concepts of imaging biomarkers, the volume ratio of small vessels to total vessels and ratio of proximal vessels to total vessels, for quantifying pruning of distal vessels and dilation of proximal vessels, respectively. Rather than assessing vascular morphology based on vessel size, Helmberger et al. [66] calculated tortuosity as well as 3D fractal dimension of segmented pulmonary vessels for characterizing vascular remodeling of patients with pulmonary hypertension.

In the pulmonary vessel quantification methods mentioned above, accurate pulmonary vessel segmentation is an important step. A few approaches have been proposed for extracting pulmonary vessels, and a challenge called VESSEL12 with a public data set and independent evaluation has been organized for comparing vessels extraction methods, among which Hessian-based methods have shown a good performance [67, 68, 69]. Tube-like structures can be enhanced by Hessian-based methods, such as the Frangi filter [70] and the Sato filter [71], where the eigenvalues of the Hessian matrix describe cylindrical properties. However, the response of Hessian-based filters is low at vessels' edges and bifurcations [72]. The 'strain energy' filter [68] can partly overcome this problem of low responses at vessels' bifurcations by analyzing the shape-tuned strain energy density. According to the VESSEL12 challenge [69], simply using a threshold or local thresholds [73] on the vesselness map (which is the

vessel likelihood map enhanced with Hessian-based methods) can not extract binary vessels accurately. In our previous work [74], a graph-cuts based method was proposed for accurately extracting lung vessels by combining the appearance (CT intensity) and shape (vesselness) features into a single cost function, and achieved a competitive performance among the submitted methods of VESSEL12 that produce binary results. Nevertheless, the separation between airway wall and vessels was still inaccurate, which could also affect the quantification of pulmonary vascular morphology, due to the similar CT intensities of airway walls and vessels.

Validating pulmonary vessel quantification methods is a challenging task, as manually annotating the ground-truth in patient images is extremely time consuming and it is hard to determine the quality and robustness of the annotated data quantitatively. As a possible alternative to validate the quantification methods, anthropomorphic phantoms containing known distributions of vessels can be considered. These phantoms can be created using 3D printing, a technique with applications in different imaging modalities, including CT, for imaging and dosimetry purposes [75, 76, 77, 78, 79, 80]. In this work, a 3D printed phantom with vessel-like structures designed in a similar way to the lung, was used to validate the proposed method for quantifying vessel morphology. A sufficiently high-resolution micro-CT scan of the lung phantom was acquired and used as the ground truth for the vessel distribution.

In this study, we present an automatic and quantitative approach to assess pulmonary vascular morphology alternations, based on an adjusted graph-cuts vessel segmentation and a novel histogram-based quantitative analysis. The automatic method consists of two steps: pulmonary vessel extraction and pulmonary vessel quantification. For pulmonary vessel extraction, we extended our previous graph-cuts based method [74] by incorporating the distance map to airways into the cost function, for separating airway walls from vessels. For pulmonary vessel quantification, a method is proposed by quantifying the radius histogram of pulmonary vessels, where all pulmonary vessels are included in the analysis, instead of only a specific part. The accuracy and robustness of the automatic method were validated with three data sets: (1) a public data set of the VESSEL12 challenge to test the accuracy of the vessel segmentation; (2) a data set of a 3D printed vessel phantom to evaluate the accuracy of vessel sizing and robustness to protocol settings of the CT scanner; (3) and finally a data set of SSc patients to confirm the correlation between pulmonary vessel morphology and pulmonary function.

3.2   Materials and Methods

3.2.1   Pulmonary vessel extraction

The segmentation task can be treated as a labeling problem $L = \{L_p | p \in \mathscr{P}, L_p \in \{0, 1\}\}$, where $\mathscr{P}$ is the set of voxels from an image and $p \in \mathscr{P}$ [81]. A voxel is labeled as object

or background according to its own properties and the connections with its neighbors. In the labeling problem of graph-cuts, the general energy function formulates the connection weights of voxel nodes, object (source) node and background (sink) node, as described in Equation (3.1). The energy function can be optimized by finding the max-flow/min-cut [82, 83]. To extract pulmonary vessels, we developed a graph-cuts based method by combining appearance features, shape features and the distance map to airway (as shown in Fig. 1(a)). The energy function of the proposed method is specified by formulating the data term $D_p(L_p)$ and neighbor term $V_{p,q}(L_p, L_q)$, with a weight γ:

$$E(L) = \sum_{p \in \mathscr{P}} D_p(L_p) + \gamma \sum_{(p,q) \in \mathscr{N}} V_{p,q}(L_p, L_q). \tag{3.1}$$

The data term $D_p(L_p)$ consists of three parts:

$$D_p(L_p) = w D_p^{\mathrm{CT}}(L_p) + (1-w) D_p^{\mathrm{VSL}}(L_p) + w_a D_p^{\mathrm{DTA}}(L_p). \tag{3.2}$$

The appearance term $D_p^{\mathrm{CT}}(L_p)$ is calculated based on the CT intensity; the shape term $D_p^{\mathrm{VSL}}(L_p)$ is calculated based on the vesselness of the strain energy filter [68]; and the distance-to-airway (DTA) term $D_p^{\mathrm{DTA}}(L_p)$ is determined by the distance map to the airways. These three terms are then balanced with weights w and w_a, where w is a global balance between appearance and shape terms, and w_a is the weight for airway wall elimination.

Since voxels with a high CT intensity or vesselness obtain a high vessel likelihood, sigmoid functions are employed for both the appearance term and the shape term. The appearance term $D_p^{\mathrm{CT}}(L_p)$ and the shape term $D_p^{\mathrm{VSL}}(L_p)$ are formulated as follows:

$$D_p^{\mathrm{CT}}(I_p^{\mathrm{CT}} | L_p = l) = \frac{1}{1 + e^{-\alpha_l^{\mathrm{CT}}(I_p^{\mathrm{CT}} - \beta_l^{\mathrm{CT}})}};$$
$$D_p^{\mathrm{VSL}}(I_p^{\mathrm{VSL}} | L_p = l) = \frac{1}{1 + e^{-\alpha_l^{\mathrm{VSL}}(I_p^{\mathrm{VSL}} - \beta_l^{\mathrm{VSL}})}}, \tag{3.3}$$

where I_p^{CT} and I_p^{VSL} represent the CT intensity and vesselness of voxel p, respectively; α_l^{CT}, β_l^{CT}, α_l^{VSL} and β_l^{VSL} are the parameters of the corresponding sigmoid function. The determination of the parameters in these sigmoid functions is described in Section 2.D.1.

The distance-to-airway map is employed in order to eliminate false detection of airway walls. Therefore, the lumen of the airway of each chest CT scan is detected by a region-growing method where a seed point was searched in the trachea and an optimal threshold was selected by iteratively growing before the leakage of airway volume [84]. Then, a Euclidean distance transform is applied for generating the distance map. The thickness of airway walls is approximately 2 mm [73, 85], thus, the response range of the distance-to-airway term is limited to (0, 3) mm. For determining
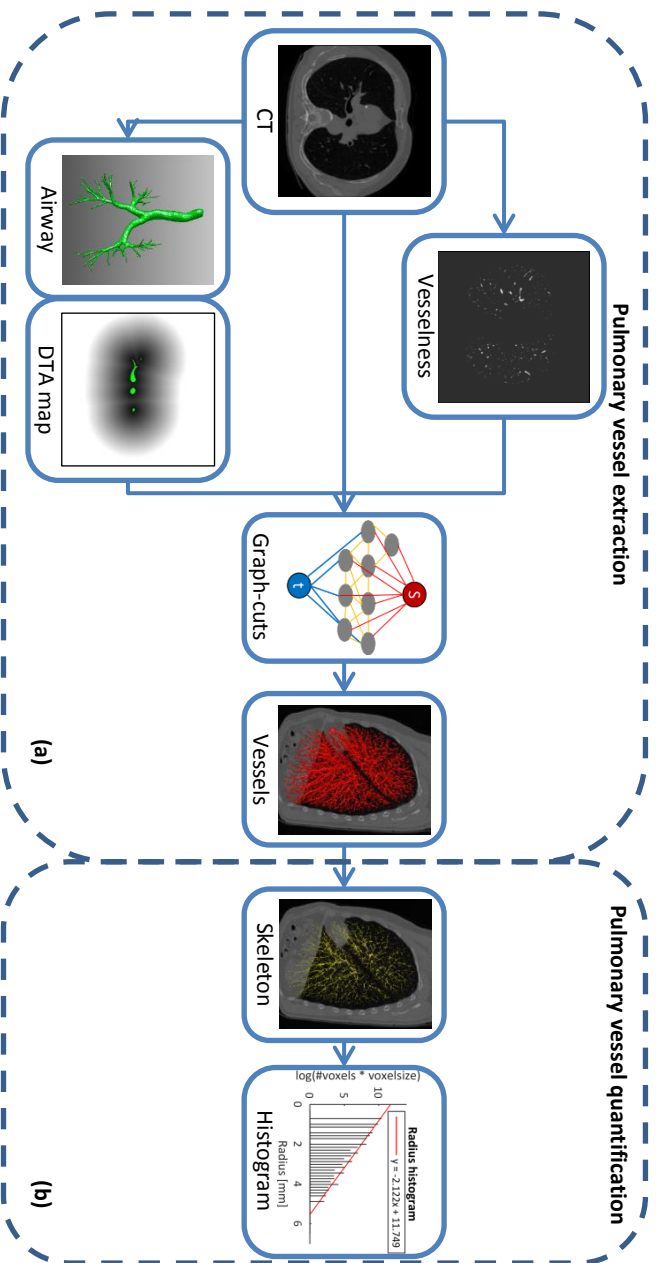
Figure 3.1: An overview of our proposed method which contains two main steps: 1) pulmonary vessel extraction and pulmonary vessel quantification. To extract pulmonary vessels, the vesselness, CT intensity and distance map to airways were incorporated into the graph-cuts cost function, as shown in (a). The vessel skeletons and radii are calculated based on the segmented vessels, and the radius histogram is counted and quantified with the proposed method, as illustrated in (b).

the response to airway walls, a Gaussian function is adopted as the kernel that centers on μ and scales with σ, as follows:

$$D_p^{\text{DTA}}(d_p|L_p = l) = \begin{cases} (-1)^l \cdot e^{-\frac{(d_p-\mu)^2}{2\sigma^2}}, & \text{if } 0 < d_p < 3\text{mm} \\ 0, & \text{otherwise.} \end{cases} \qquad (3.4)$$

The neighbor term $V_{p,q}(L_p, L_q)$ from Equation (3.1) is the cost for cutting a neighborhood edge (p, q) on the basis of their similarity and γ is a positive coefficient for controlling the smoothness of detected objects. It is calculated based on the similarity in CT intensity of two neighborhood voxels ($p, q \in \mathcal{N}$), and corrected by the spatial distance between them:

$$V_{p,q}(L_p, L_q) = \begin{cases} e^{-d_{p,q} \cdot |I_p^{\text{CT}} - I_q^{\text{CT}}|}, & \text{if } L_p \neq L_q \\ 0, & \text{otherwise,} \end{cases} \qquad (3.5)$$

where $d_{p,q}$ represents the spatial distance between voxels p and q. In other words, if two neighboring voxels (p, q) have similar CT intensities and are close together but are labeled differently, the cost of the n-edge (p, q) will be high.

3.2.2 Pulmonary vessel quantification

Based on the segmented pulmonary vessels, the centerlines of vessel trees are extracted using a skeletonization method [86]. This method successively erodes the border voxels for locating the vessel centerline where a refinement step was adapted for eliminating the side branches; the distance between boundary voxels and central voxel are calculated and the minimum distance is used to estimate the corresponding radius. This estimated radius is subsequently assigned to that central voxel, producing a 3D skeleton map with radius value embedded in the centerline voxels, as illustrated in Fig. 3.1(b).

The number of voxels in the vessel skeleton with a specific radius on the vessel skeleton are counted as N_r. The vessel radius frequency is normalized for voxel size (V_l) to make the histogram comparable across CT scans, i.e. instead of simply using the counted number, the accumulated length was estimated with the number of voxels and their size. In order to obtain a linear relation between frequency and radius, a logarithmic transformation is applied to the normalized frequency in the histogram. Afterwards, a 'radius histogram' is generated for pulmonary vessels of each CT scan, in which the ith bin' index represents the vessel radius, r_i, and its height characterizes the logarithm of the normalized frequency of occurrence, $log(N_{r_i} \cdot V_l)$.

$$y = \alpha \cdot x + \beta$$
$$\text{where } y = log(N_r \cdot V_l) \text{ and } x = r. \qquad (3.6)$$

For quantifying the pulmonary vessel morphology, the 'robustfit' method (in MATLAB R2016a Mathworks, Natick, MA [87]) was applied to solve the linear regression in Equation (3.6). For each patient, two biomarkers, α and β, are calculated, which correspond to the slope and intercept of the linear regression, respectively, see Fig. 3.1 (b). The slope parameter α quantifies the occurrence of vessels with small radius relative to those with large radius, which may indicate pruning of small vessels and/or dilation of larger vessels. The intercept parameter β is an extrapolation of the radius histogram to radius 0, which estimates the number of pulmonary capillaries and may relate to the pulmonary vascular tree's capacity.

3.2.3 Implementation and parameter settings

The graph-cuts based vessel segmentation method was implemented in Matlab and its cost function was optimized with a mixed C++ code [1]. This proposed vessel segmentation method was made publicly available by the authors [2]. The strain energy filter for vessel enhancement is also open source and can be found via ITKTools [3]. The quantitative method for analyzing the pulmonary vascular morphology benefited from the DtfSkeletonization module of MeVisLab and the robust linear regression method in MATLAB. The entire processing pipeline was completed in MeVisLab 2.7.1 (VC12-64), on a personal computer configured with 24 GB of memory, a 2.67 GHz CPU (Intel Xeon W3520) and a 64-bit Windows 7 operating system.

The parameters used in the segmentation method were optimized on the VESSEL12 training set. The appearance and shape features were normalized to ranges of [0, 1], before incorporation in the cost function. The strain energy filter's parameters were set according to the literature [68, 74]. Before construction of the graph, a very low threshold of 0.0009 was used on the vesselness map to exclude voxels that almost certainly belong to the background. This resulted in a relatively small sparse graph structure, which was constructed with the remaining voxel nodes, object and background nodes, and allowed processing of high resolution CT scans.

The balance parameter w between appearance and shape terms was set to 0.6 [74], and the parameter w_a of the distance to airway term was set to 0.4, optimized with a grid search approach on the training data set. Because the response region of the distance to airway term was limited to a local region around the airways, the parameter w_a was not set as a global balance, in comparison to the global balance parameter w. The parameters of the sigmoid function in the appearance term $D_p^{\mathrm{CT}}(L_p)$ and shape term $D_p^{\mathrm{VSL}}(L_p)$ were automatically estimated with the following algorithm. The mean value of the appearance feature was picked as the initial threshold to initially separate the background and object. The appearance feature inside the object region was fitted

---

[1]http://www.wisdom.weizmann.ac.il/ bagon/matlab_code/GCmex1.9.tar.gz
[2]https://github.com/chushan89/Lung-Vessel-Segmentation-Using-Graph-cuts
[3]https://github.com/ITKTools/ITKTools

with a Gaussian distribution, by calculating the mean μ and standard deviation std. Then, the parameters of the sigmoid function were estimated by fitting a Gaussian distribution, such that $Sigmoid(\beta) = Gaussian(\beta) = 0.5$ and $Sigmoid(\mu) = 0.95$. The parameters used in the cost function for the shape term were calculated in a similar way.

For the parameters of the DtfSkeletonization module, the 'object min value' parameter was set to 1, as the graph-cuts output was set to binary. The 'cavity value', which controls the closing of cavities in binary objects before detecting the skeleton, was set to 10 voxels (default value). The limitation of maximum erosion distance (by 'max distance' parameter) was turned off. The 'skeleton only' option was checked, therefore, only the voxels on the vessel skeleton were coded with the estimated radius in the output image. A vessel radius can obtain a value from only a limited number of possible distances, due to the limited and constant voxel size. To capture all these unique radii in the histogram, the bin size was set to as small as 0.001. To calculate the imaging biomarkers α and β, a linear regression was applied to the radius histogram. In the regression analysis, the first non-empty bin was excluded as this might be influenced by the noise of small branches in vessel skeleton extraction.

3.2.4 Data sets used for validation

3.2.4.1 Data set of VESSEL12

The proposed pulmonary vessel segmentation method was validated on the VESSEL12 challenge data set [69], which contains three CT scans in a training set and 20 CT scans in a testing set. These anonymous scans were collected from three hospitals: the University Medical Center Utrecht (Utrecht, The Netherlands), the University Clinic of Navarra (Pamplona, Spain), and the Radboud University Nijmegen Medical Centre (Nijmegen, The Netherlands). In the 20 testing CT scans, points of interest were annotated individually by three trained medical students with four possible labels: vessel, lung parenchyma, airway wall or lesion [69]. Only the points on which all three annotators agreed were included in the ground truth. In the three training CT scans, the annotations were labeled in a similar way, however, there were only two label categories (vessel and non-vessel). Furthermore, the lung masks for each of these scans were provided by the VESSEL12 challenge organizers.

For the three CT training scans, we performed lung vessel segmentation and the corresponding evaluation results can be found in the Appendix. For the 20 CT scans in the testing data set, the binary pulmonary vessels, which were extracted using the graph-cuts based method, were uploaded to the VESSEL12 challenge website and independent evaluation results were calculated by the organizers. The area under the ROC curve (Az) was used as the main score for validation. Binary segmentations were applied to a distance transform for generating probabilistic maps, subsequently, the
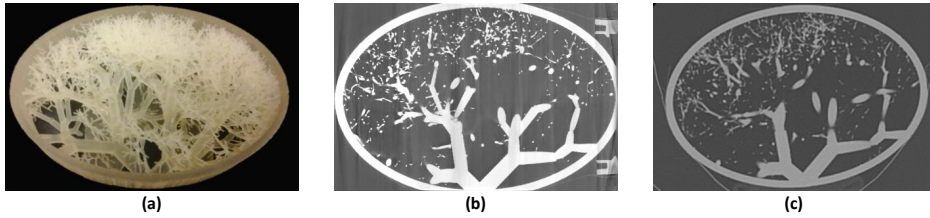
Figure 3.2: 3D printed vessel phantom (a), together with one slice of the micro-CT scans (b) and one slice of a clinical CT scan (c).

ROC curve was calculated based on the probabilistic maps.

3.2.4.2 Data set of vessel phantom

To validate the proposed method for quantifying vessel morphology, a 3D printed phantom, representing vessel-like structures with similar sizes as in the lung, was used. This phantom was designed based on the work by Weibel et al. who performed a microscopic study of lungs from human cadavers [88, 89]. An algorithm was developed in MATLAB (Mathworks, Natick, MA) to generate a model of a vessel tree structure, with decreasing length and diameter for the vessels, modelled as cylinders, in each vessel generation iteration [90, 91]. The model was constrained to an elliptically shaped frame (150x103x26 mm), as it was intended for manufacturing a small phantom for image quality in CT [90, 91]. The vessel tree started growing at the center of one of the sides of the ellipse (Fig. 3.2 (a)). At each vessel segment ending, there could be a bifurcation or an elongation. The bifurcation chance increased after each elongation step. The direction of the two generated branches after a bifurcation was randomly taken but limited within 45°, with regard to the parent vessel direction. The lung model was printed using a ProJet HD 3000 3D printer with multi jet modeling (MJM) technique in ultrahigh definition mode, selecting Visijet EX200 as material. This mode enables to print very thin layers (32 μm) of material. The total number of generated vessel segments was in the order of 20000 being the biggest 10 mm diameter and the smallest in the order of 0.2 mm [91].

The 3D printed vessel phantom was imaged with a clinical CT scanner (Aquilion ONE, Toshiba Medical Systems, Otawara, Japan) with the following acquisition parameters: 0.5×64 mm collimation, 120kV, pitch 0.828, 0.5 s rotation time, FOV of 195.1 mm, and various tube currents (10, 20, 50, 100 mA). Images were reconstructed with 0.5 mm slice thickness and interval, selecting FC30 as convolution kernel with two reconstruction methods, filtered back projection (FBP) and AIDR3D standard. The voxel dimensions were $0.38 \times 0.38 \times 0.5$ mm. In total, 8 CT scans were available to be analyzed (4 dose levels, 2 reconstruction methods). To obtain the ground truth of

the 3D printed vessel phantom, the phantom was scanned with a Zeiss Xradia 520 Versa micro-CT scanner, selecting 80 kV, 7 W and a 0.4 X objective and no additional filtration. The total scanning time was 36 hours and vertical stitching was applied to obtain the image volumes (1894 × 1903 px by 2922 images). The voxel size was $52 \times 52 \times 52$ μm and the micro-CT images, in TIFF format, were 8-bits depth. The images were reformatted and rotated in MeVisLab, in order to obtain the same cross-sections as in the CT scans.

3.2.4.3 Data set of SSc patients

Patients with systematic sclerosis (SSc) were selected from the biobank of the Leiden Combined Care in SSc (77 patients; 67 women and 10 men; mean age ± STD, 49.9 ± 14.2 years). The images were obtained with a thorax protocol and the patients took pulmonary function tests (PFT) [92]. All patients were scanned with the same CT scanner (Aquilion 64, Toshiba Medical Systems, Otawara, Japan), during full inspiration and without contrast medium. The CT protocol settings were: tube current 140 mA without modulation; tube voltage 120kV; rotation time = 0.4 s; collimation = 64×0.5 mm; images were reconstructed with 0.5 mm slices [25]. The local Medical Ethical Committee approved the protocol. Written informed consent was obtained from each patient prior to enrollment. The fibrosis scorings of these patients were established by two experts (a radiologist, L.K. and a rheumatologist, A.S.) on the basis of CT scans and blinded to the clinical information [11]. PFTs were tested including total lung capacity (TLC), forced vital capacity (FVC), forced expiratory volume in 1 second (FEV_1) and single-breath diffusion capacity for carbon monoxide corrected for haemoglobin concentration (DLCOc), and the PFT results were expressed as a percentage of the predicted value [93, 94]. Patients who had no fibrosis were selected, however the gas transfer (DLCOc %predicted) of them were impaired. Thus, we hypothesized that pulmonary vascular changes could partly explain the impaired gas transfer, for patients without lung fibrosis.

3.3 Results

The proposed graph-cuts based method obtained an Az of 0.976, which is a competitive performance among 31 submitted methods and the best result among binary submissions of VESSEL12, where the average and range for Az were 0.83 and (0.671, 0.976), respectively. The evaluation results of three binary submissions with top ranking performance are shown in Table 3.1: the binary submissions (LT) of van Dongen et al. [73] who extracted vessels with local thresholds on Frangi filter's vesselness and excluded airway walls by dilating the airway segmentation; the binary submissions (AS) of our previous method which segmented vessels with a graph-cuts based method by combining only appearance and shape features into the cost function; the binary submissions (ASD) of the newly proposed method which detected vessels

Table 3.1: Area under the ROC curve (Az) score of three binary submissions to the VESSEL12 challenge across all categories (Categories 1: Principal, 2: Small Vessels, 3: Medium Vessels, 4: Large Vessels, 5: Vessel/Airway Wall, 6: Vessel/Dense Lesion, 7: Vessel/Mucus-filled bronchi, 8: Vessel-in-lesion/Lesion, 9: Vessel/Nodules). The binary submission using local threshold on Frangi's vesselness (LT, [73]), the graph-cuts based method combining the appearance and shape feature (AS, [74]), and the method proposed in this work incorporating appearance, shape and distance to airway (ASD).

Categories	1	2	3	4	5	6	7	8	9
LT	0.932	0.885	0.954	0.955	0.912	0.688	0.404	0.649	0.517
AS	0.973	0.952	0.973	0.992	0.861	0.485	0.297	0.658	0.255
ASD	0.976	0.958	0.977	0.993	0.930	0.484	0.305	0.661	0.254

with a graph-cuts based techniques by incorporating appearance and shape features and distance to airway. The evaluation results of all submissions are also available online on the VESSEL12 website [4].

The vessels in the 8 CT scans of the phantom were segmented with the proposed graph-cuts based method. The supporting oval frame surrounding the 3D printed vessels in the phantom was removed using a cylinder mask. As there were no airways designed in this phantom, the distance map to the airway was set to zero. The vessels in the micro-CT scan were extracted using a threshold, which was determined by density histogram analysis, see Fig. 3.3(a). The distribution of the voxel density in the micro-CT scan had two peaks, the peak with lower density value corresponds to the background (air) and the peak with higher density value corresponds to the vessels. Thus, the density value with minimum frequency between these two peaks was selected as threshold to extract vessels from the micro-CT scan. The threshold $T = 156$ was used to segment vessels in this study. The 3D and 2D view of the extracted vessels are illustrated in Fig. 3.3 (b) and (c). For testing the robustness of this ground truth vessel extraction, we selected a range of thresholds (156 ± 4) to extract vessels (see Appendix).

Based on the extracted vessels in the micro-CT scan and the 8 CT scans, the corresponding vessel size was calculated with the DtfSkeletonization module of MeVisLab, where the estimated radius was recorded at the vessel centerlines. The micro-CT scan was registered to the 8 CT scans of the phantom using Elastix registration [95], separately, with the following settings: four-level pyramid, adaptive stochastic optimizer, B-spline interpolator, Euler transformation, and maximum number of iterations 250. The skeletons in the micro-CT scan were extended into a 'radius tube' by assigning the voxels on each cross section with the radius that was recorded on its

---

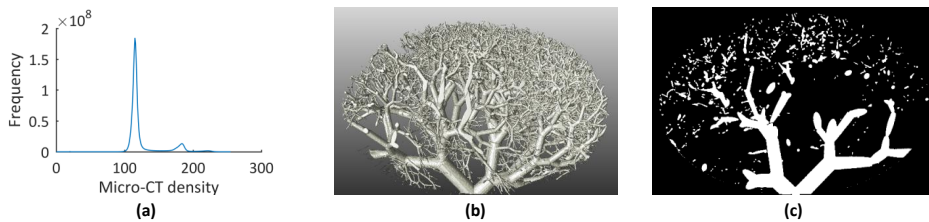[4]https://vessel12.grand-challenge.org/results/

Figure 3.3: Histogram and extracted vessels of the vessel phantom in the micro-CT scan, (a) the histogram of the micro-CT scan of 3D printed vessel phantom, (b) 3D view of the extracted vessels in the micro-CT scan, (c) 2D view of the extracted vessels.

centerline, in order to overcome the mismatching between skeletons of micro-CT scan and clinical CT scans. With the transformation parameters, the radius tube obtained in micro-CT scan was transferred to each CT scan. For each CT scan, we got a mapping vector with two columns: one contained the radius value of vessels in the clinical CT scan and the other contained the radius value of the corresponding vessels in the micro-CT scan. The median (M) and IQR of radius differences (radius of CT - radius of micro-CT) were on average of 0.062 and 0.199, with STD of 0.02 and 0.05, respectively, which shows high robustness. The correlations (R) between radius in CT and micro-CT scans were calculated with Pearson's correlation. The correlations are presented in Table 3.2. The correlations were all statistically significant and the average correlation was 0.909 (p-value< 0.001). Furthermore, linear regression was applied to the radii from the clinical CT scans and those from the micro-CT scan. All regression analysis results are shown in Table 3.2, with an average slope and intercept of 1.018 and -0.058, respectively. The 2D histograms and linear regressions between radius of CT scans and micro-CT scan are shown in Fig. 3.4.

The vascular morphology in the clinical CT scans of the phantom was studied with the proposed radius histogram analysis method, based on the extracted vessels. For each CT scan, two imaging biomarkers (α and β) were obtained for quantifying the vascular morphology of the phantom, where the intercept β estimates the number of small vessels and the slope α quantifies the relative contribution between small and large vessels. The results of the biomarkers are presented in Table 3.2. The STD (average) of biomarker α is 0.034 (-1.785), and the STD (average) of biomarker β is 0.049 (7.03), which implies that the proposed method is robust against CT scanner settings, in particular variation in dose (mAs) and for two reconstruction methods (FBP and AIDR 3D). The vascular morphology was investigated in the micro-CT scan with the proposed method, based on the vessels extracted with a threshold of 156. The imaging biomarkers α and β were -1.803 and 7.265, respectively. The average of difference in α and β between micro-CT scan and clinical CT scans was -0.019 and

Table 3.2: Results of comparing radius analysis between CT scans and micro-CT scan, and results of quantifying vessel morphology of vessel phantom. The metrics median (M), interquartile range (IQR), correlation (R) are presented.

CT setting	Comparison with micro-CT scan				Biomarkers	
	M (IQR) [mm]	R (p-value)	slope	intercept	α	β
10mA, FBP	0.028 (0.281)	0.869 (< 0.001)	0.980	0.040	-1.780	7.035
20mA, FBP	0.031 (0.275)	0.874 (< 0.001)	0.986	0.031	-1.780	7.034
50mA, FBP	0.073 (0.172)	0.922 (< 0.001)	1.029	-0.088	-1.817	7.062
100mA, FBP	0.072 (0.179)	0.921 (< 0.001)	1.031	-0.091	-1.795	7.058
10mA, AIDR3D	0.074 (0.168)	0.921 (< 0.001)	1.030	-0.090	-1.709	6.918
20mA, AIDR3D	0.073 (0.169)	0.920 (< 0.001)	1.027	-0.087	-1.783	7.011
50mA, AIDR3D	0.073 (0.170)	0.921 (< 0.001)	1.029	-0.088	-1.817	7.062
100mA, AIDR3D	0.072 (0.179)	0.920 (< 0.001)	1.032	-0.092	-1.795	7.058
Average	0.062 (0.199)	0.909	1.018	-0.058	-1.785	7.030
STD	0.020 (0.050)	N.A.	0.022	0.058	0.034	0.049

0.235, respectively.

With regard to the patient images from the Leiden Combined Care biobank, the lung masks were detected with a multi-atlas based method and pulmonary vascular morphology was investigated with the proposed method. The imaging biomarkers (α, β) were collected for all these patients. The average $\pm$ STD of α and β are (-1.49 ± 0.2) and (9.58 ± 0.61), respectively. The correlations between imaging biomarkers and DLCOc %predicted were studied with Spearman's rho correlation. In the studied patient group, the imaging biomarkers, α (R=-0.27, p-value=0.018) and β (R=0.321, p-value=0.004), were significantly correlated with DLCOc %predicted (with average $\pm$ STD, 70.4 ± 16.7). The processing results of two patients in this SSc patient group, who were quantified with the proposed method, are illustrated in Fig. 3.5.

3.4 Discussion

In this work, we proposed an automatic method, which consisted of two processing steps: a graph-cuts based pulmonary vessel extraction and a radius histogram based pulmonary vessel quantification, for investigating pulmonary vascular morphology in CT images. The accuracy of the graph-cuts based vessel segmentation method was validated with a public data set, and a competitive result was obtained among other submissions. The robustness of the pulmonary vessel quantification method was validated with a 3D printed vessel phantom data set, demonstrating a robust measurement by comparing CT and micro-CT scans. The pulmonary vascular morphology in each CT scan was quantified into two biomarkers, α and β. The association between pulmonary vascular morphology and gas transfer was investigated with a data set of 77 patients in SSc. The biomarkers, α and β, were significantly correlated with DLCOc % predicted, indicating that the impaired gas transfer is associated with the remodeling of pulmonary vascular morphology.

Extracting pulmonary vessels accurately is an essential processing step for quantifying pulmonary vascular morphology. In this work, a graph-cuts based method was proposed for vessel segmentation, by including voxel's appearance and shape features into a cost function. In comparison with methods using simply threshold or local-threshold on vesselness, the proposed vessel segmentation method performed well according to the independent validation of VESSEL12. This might be due to the fact that the graph-cuts based method considers multiple features for each voxel and assigns voxel's label incorporating its neighbouring information. For separating the airway walls and vessels, the distance map was integrated into the graph-cuts cost function. In the method proposed by van Dongen et al. [73], the airway walls were excluded by dilating the airway with a spherical element with a specific size, which might remove partially vessels touching airway walls. Our method obtained slightly better performance in separating the airway walls, as illustrated in Table 3.1, category
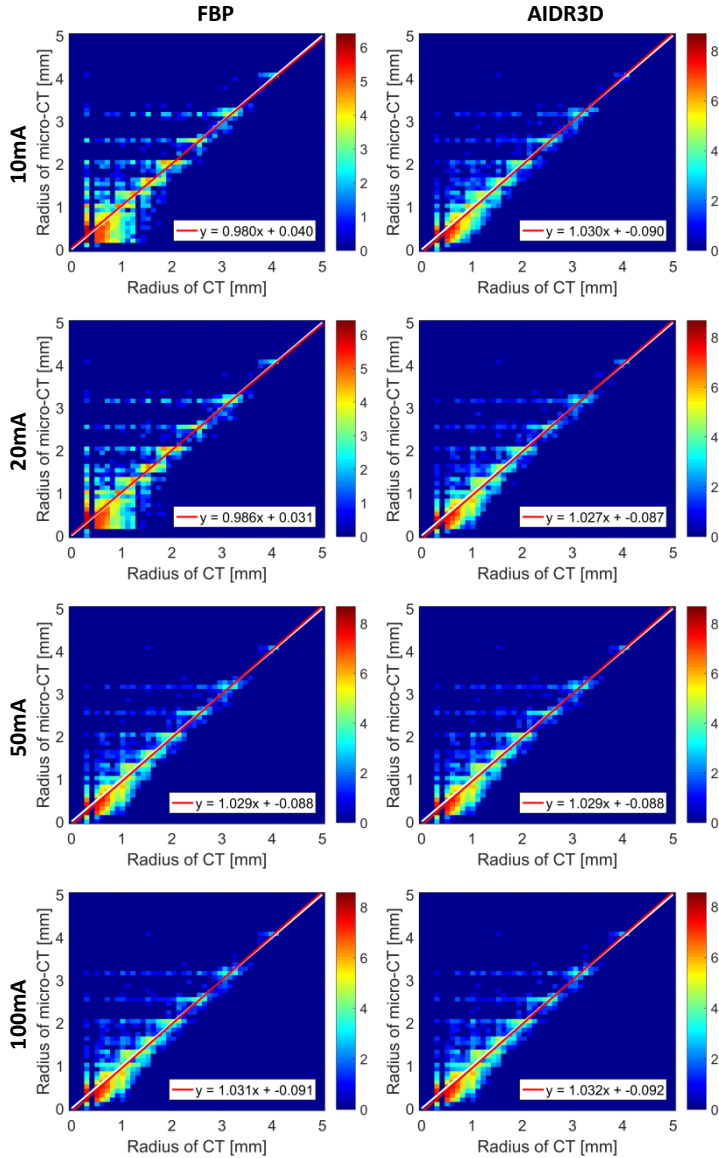
Figure 3.4: Comparison between the vessel radius estimated from the micro-CT scan and those from the clinical CT scans, for a range of dose levels and two reconstruction algorithms (FBP and AIDR3D). In each sub-figure, the x-axis contains the radii from the clinical CT and y-axis contains the radii from the micro-CT scan; the color scale implies the logarithm transformed frequency of the joint histogram; the white line is the identity line and the red line is the line of linear regression.
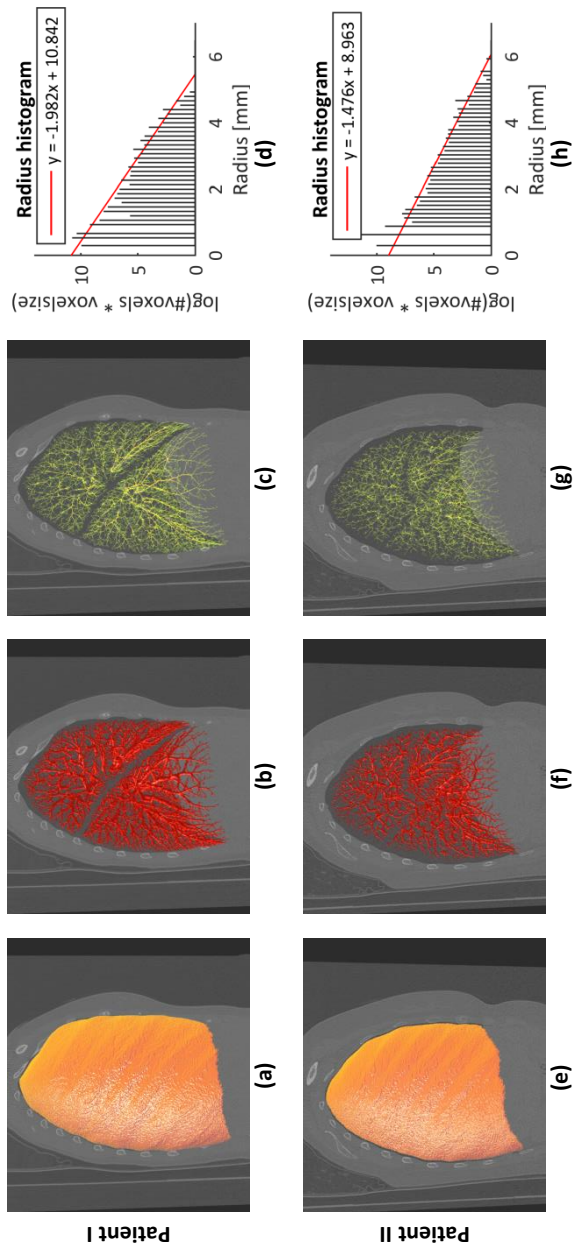
Figure 3.5: The pulmonary vascular morphology of two patients in SSc were quantified with the proposed method, and the DLCOc %predicted of patient I and II were 101.5 % and 44.6 %, respectively. (a, e) the detected lung mask; (b, f) the extracted pulmonary vessels; (c, g) the pulmonary vessel skeleton; (d, h) the radius histogram.

5. Our method performed slightly worse, on the other hand, in distinguishing vessels from dense lesions or nodules, categories 6 and 9, which may be due to the fact that intensity of lesions and nodules are similar to vessels. These are however not expected in patients with SSc.

The quantitative analysis of the extracted pulmonary vessels was performed on the radius histogram, where the vessel radii were calculated by a distance transform based method. The accuracy of vessels sizing and the robustness of vessel morphology quantification were validated using a data set of a 3D printed vessel phantom, which was scanned with a micro-CT scanner and a clinical CT scanner. The geometry model of the phantom was not used as a gold standard or ground truth for comparisson, because the accuracy of the 3D printing process (which depends on the printer, technique and selected material) can introduce differences between the model and the actual final printed object. Establishing robust methods to determine the accuracy and reproducibility of 3D printing, in particular for phantoms is still under investigation [91]. The characteristics and limitations of the material used in the lung phantom compared to human vessels were discussed elsewhere [91]. The use of 3D printing has grown in the past years in different areas in medicine, such as biocompatible prosthesis development, surgery planification with models based on patient images and educational purposes [5]. One of its applications is the development of affordable customized test objects or phantoms that can be used in image quality assessment in different medical imaging modalities [96, 76]. O'Dell et al. validated the accuracy of sizing vessels using a 3D printed vascular phantom made of acrylonitrile butadiene styrene plastic. The vessel sizes (with diameters ranging from 1.2 to 7 mm) were evaluated by manual measurements at 64 branches [77]. Due to the complexity of our 3D printed vessel phantom, however, the vessel sizes were not manually measurable.

For out study, a micro-CT scan with sufficiently high resolution was used for calculating the ground truth of vessel sizes. Thus, we validated the accuracy of sizing vessels by comparing clinical CT scans with micro-CT scan, and evaluated the vessel size in all vessel trees by matching the clinical and micro- CT scans. The differences of vessel radii calculated from clinical CT scans and micro-CT scan were very small; therefore, these radii were highly correlated; and the regression analysis between radius from clinical CT scans and micro-CT scan obtained average slope approximated to 1 and average intercept approximated to 0, implying that the radii detected in CT scans and in micro-CT scan are almost equal. As presented in Table 3.2, the IQR of radius differences is smaller by increasing the dose (mA) for reconstruction kernel FBP, while it is much more stable for the kernel AIDR3D, which implies the kernel AIDR3D performed well for reconstructing images, with low mA settings.

---

[5]AAPM Special Interest Group in 3D printing (https://www.rsna.org/3D-Printing-SIG/)

The vascular morphology of the extracted vessels was characterized by two biomarkers, α and β. The biomarker α, which is the slope of the radius histogram, reflects the related contributions between small vessels and large vessels, quantifying small vessels pruning and large vessel dilation. The intercept β, which was calculated by extrapolation to radius 0, estimates the vascular tree capacity, without actually detecting pulmonary capillaries. The robustness of the automatic quantification method was validated with CT scans acquired with various settings, while the variation in biomarkers was quite small. The average difference in between micro-CT scan and clinical CT scans is 0.025 by $|\alpha_{micro-CT} - \alpha_{CT}|$ and 1.4 % by $|(\alpha_{micro-CT} - \alpha_{CT})/\alpha_{micro-CT}| * 100$, while that in β is 0.235 and 3.2 %, respectively, i.e., comparing clinical CT scans to micro-CT scan, the biomarker about relative contribution between small vessels and large vessels were similar, in comparison with the biomarker of vessel tree capacity, which might be due to the fact that the micro-CT performed better in detecting small vessels. The relation between gas transfer and biomarkers was validated with a data set of 77 SSc patients. The α and β showed significant correlations with DLCOc % predicted, which implied that the vascular remodeling (pruning/dilation and vascular tree capacity) is associated with impaired gas transfer. Vascular remodeling as assessed in HRCT may precede changes in gas transfer and may therefore be important in the clinical evaluation and treatment decisions of SSc patients. Although, the correlations between imaging biomarkers and gas transfer were moderate, these were comparable results in the relevant study [62].

There are some limitations in this work. The lung vessel segmentation method did not work well for separating vessels and lung nodules, as the latter are mostly attached to vessel trees and have a high intensity, eliminating the response of nodules by considering the shape properties may be helpful for separating vessels and nodules, however, detecting / extracting lung nodules is not the goal of this study. The 3D printed vessel phantom used in this study contained a wide range of vessel radii and lengths. A future development in using this type of phantoms to test algorithms could be to control the number of vessels that are generated per diameter or length, during the design process. In this way, a robust ground truth based on the model could be compared. One of the limitations for the phantom is that the attenuation of the material used to print the vessels is slightly higher compared to human vessels [90, 91]. Nonetheless, when comparing the the relative contrast between the lung phantom vessels and the background (air) with values measured in vessels and parenchyma in patients, the difference is relatively small (around 10%). This limitation could be overcome in the future if other materials become available that could be printed with the required resolution and a lower attenuation. Nonetheless, these differences in attenuation don't influence the results in the present study, as the presented method for pulmonary vascular morphology analysis can be adapted to assess the target

characteristics, in this case. In this work, the automatic quantification method was applied on both lungs together. Applying the quantification method on separate lungs or lung lobes may allow more localized assessments of vascular remodeling. In the future, we will investigate deep-learning techniques in pulmonary analysis, as these techniques generally perform well in medical images analysis. We did not separate the arteries and veins for specific analysis. Developing a deep-learning based method for separating arteries and veins is also a challenging but interesting topic for our future work [97, 98, 99], as pulmonary vascular diseases may affect arteries and veins differently. For validating the association between biomarkers and gas transfer, only the SSc patient group was involved without a control group. Quantifying the vascular morphology of healthy people may improve the detection of lung vasculopathy in SSc patients. However, even without these specific analyses or a control group, we already found a significant association between vascular morphology and gas transfer.

3.5   Conclusions

In conclusion, an automatic method has been proposed for quantifying pulmonary vascular morphology in CT images. The accuracy of vessel segmentation has been evaluated independently with the public data set of VESSEL12, and the robustness of the quantification method has been validated with the image data set of a 3D printed vessel phantom. The imaging biomarkers for quantifying pulmonary vessel morphology in CT images are correlated with gas transfer in the studied SSc patients.

Acknowledgements

Supplementary

Evaluation with three CT scans of VESSEL12 training set

In the VESSEL12 challenge, there are three CT scans in the training set, with the corresponding lung masks and annotations files. In each CT scan, points were annotated into 0 or 1 by three annotators, where 0 means non-vessel and 1 means
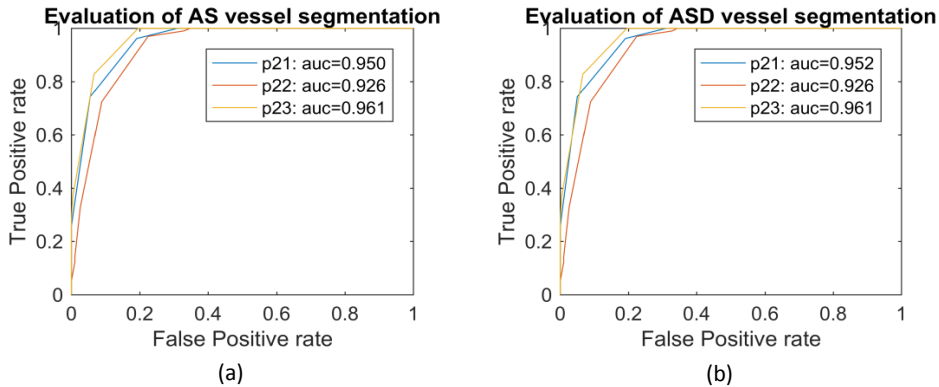
Figure 3.6: A1. ROC evaluation of method AS and ASD. The cure of p21, p22 and p23 are corresponding to three CT scans in training set.

vessel. Only points which 3 annotators agreed on the label were included in the annotation file. Finally, there are around 300 points with positions <x, y, z> and labels included in the annotation file, for each CT scan.

For each CT scan, the AS and ASD methods were used for segmenting lung vessels within lung region, separately. For these binary segmentation results, a signed distance transform was applied to for generating a probabilistic mask. Finally, the ROC cure were calculated based on the probabilistic mask and annotated points, see Figure, 3.6. The method ASD obtained an average AZ of 0.946 which is slightly better than method As, 0.945. Furthermore, the AZ of vessel segmentation in training set is worse than that in testing set, which might because that the in-house used distance transform method is not exactly the same with the method used by VESSEL12 organizers, and the annotation categories are not the same between training and testing sets.

Vessel extraction in micro-CT scan

As presented in the Fig 3 (a). of main text, there are two clear peaks in the density histogram of the micro-CT scan, where the peak with lower density corresponds to the background, and the one with higher density corresponds to the vessels. The density value (T=156) is the minimum frequency and selected as threshold to segment vessels. For testing the robustness of vessel extraction, we selected a range of thresholds 156±4 to extract vessels, and the segmentation results was compared with the reference segmentation (T=156). The radius difference histogram between vessels of threshold i and reference were presented in Figure 3.7. The results of comparing radius analysis between threshold i and reference were presented in Table 3.3, where the median M radius difference is 0, IQR is also 0, the average correlation (R) is 0.980, and slope (intercept) is 1.018 (0.003).
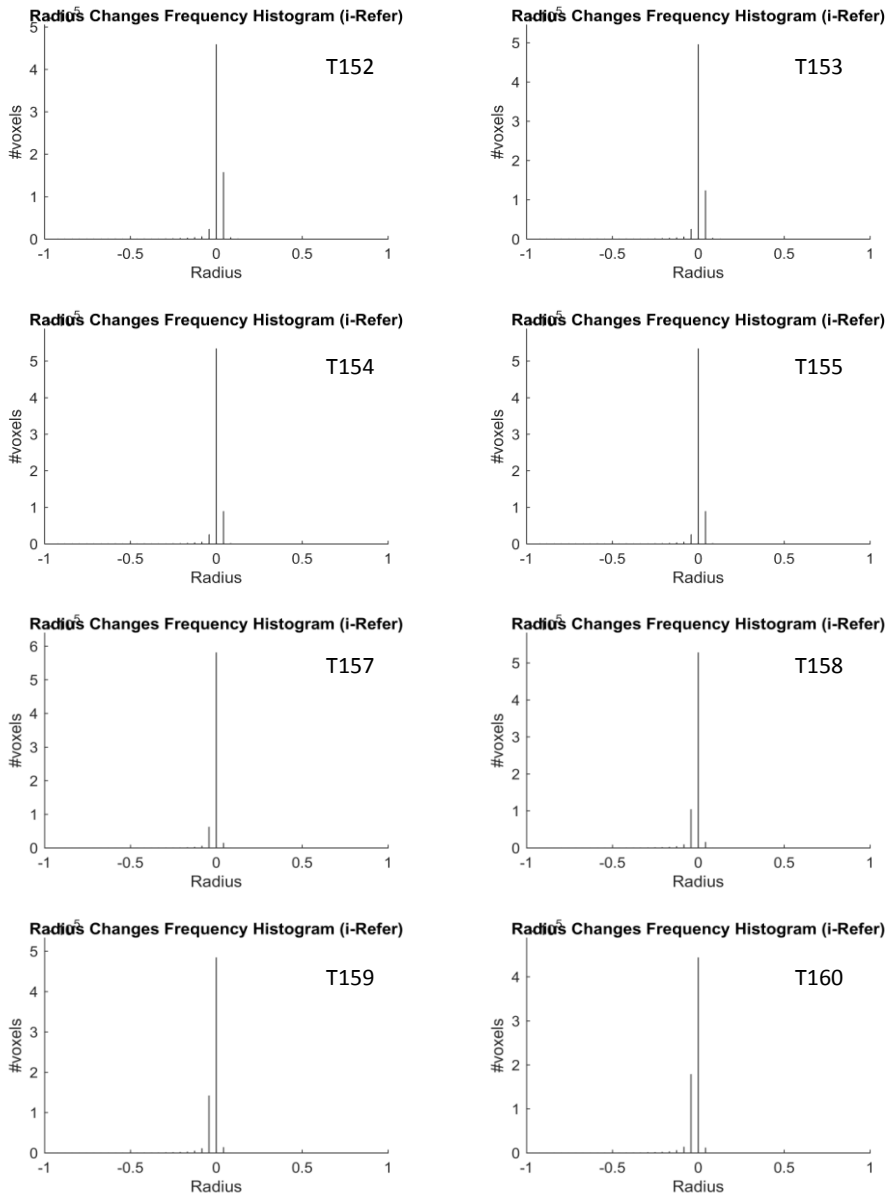
Figure 3.7: A2. Radius difference frequency histogram between threshold i and reference threshold.

Table 3.3: Results of comparing radius analysis between threshold i and reference threshold

T i	M (IQR)	R (p-value)	slope	intercept
		T reference		
152	0 (0)	0.981 (0.000)	1.015	-0.006
153	0 (0)	0.978 (0.000)	1.019	-0.004
154	0 (0)	0.979 (0.000)	1.020	-0.004
155	0 (0)	0.987 (0.000)	1.013	-0.001
157	0 (0)	0.986 (0.000)	1.014	0.004
158	0 (0)	0.981 (0.000)	1.018	0.008
159	0 (0)	0.975 (0.000)	1.021	0.011
160	0 (0)	0.976 (0.000)	1.025	0.013
Average	0	0.980	1.018	0.003
STD	0	0.004	0.004	0.007

4

Pulmonary vascular morphology associated with gas exchange in systemic sclerosis without lung fibrosis

Abstract

Purpose Gas exchange in systemic sclerosis (SSc) is known to be affected by fibrotic changes in the pulmonary parenchyma. However, SSc patients without detectable fibrosis can still have impaired gas transfer. We aim to investigate whether pulmonary vascular changes could partly explain a reduction in gas transfer of systemic sclerosis (SSc) patients without fibrosis.

Materials and Methods We selected 77 patients, whose visual CT scoring showed no fibrosis. Pulmonary vessels were detected automatically in CT images and their local radii were calculated. The frequency of occurrence for each radius was calculated, and from this radius histogram two imaging biomarkers (α and β) were extracted, where α reflects the relative contribution of small vessels compared to large vessels and β represents the vessel tree capacity. Correlations between imaging biomarkers and gas transfer (DLCOc %predicted) were evaluated with Spearman's correlation. Multivariable stepwise linear regression was performed with DLCOc %predicted as dependent variable and age, BMI, sPAP, FEV1 %predicted, TLC %predicted, FVC %predicted, α, β, voxel size and CT-derived lung volume as independent variables.

Results Both α and β were significantly correlated with gas transfer (R=-0.29, p-value=0.011 and R=0.32, p-value=0.004, respectively). The multivariable step-wise linear regression analysis selected sPAP (coefficient=-0.78, 95%CI=[-1.07, -0.49], p-value<0.001), β (coefficient=8.6, 95%CI=[4.07, 13.1], p-value<0.001) and FEV1 %predicted (coefficient=0.3, 95%CI=[0.12, 0.48], p-value=0.001) as significant independent predictors of DLCOc %predicted (R=0.71, p-value<0.001).

Conclusions In SSc patients without detectable pulmonary fibrosis, impaired gas exchange is associated with alterations in pulmonary vascular morphology.

4.1 Introduction

Systemic sclerosis (SSc) is an autoimmune connective tissue disease that involves multiple organs [9]. Pulmonary disease in SSc mainly consists of interstitial lung disease (ILD) and pulmonary hypertension (PH) [10]. For evaluating severity of disease and response to treatment, pulmonary function tests (PFTs), such as diffusion capacity for carbon monoxide (DLCO) and forced vital capacity (FVC), are key outcome measures which play an important role as a surrogate for ILD and PH-related mortality [100]. In SSc-related ILD, structural changes of lung parenchyma, i.e. fibrosis, is known to affect PFTs [10, 101, 102, 103, 104]. In SSc-related PH, DLCO decreases years before diagnosis of PH [13]. Conversely, gas transfer can be mildly or moderately impaired in the absence of detectable pulmonary fibrosis and pulmonary hypertension. Since gas transfer studies measure the alveolar capillary membrane gas exchange efficiency [105], we hypothesized that pulmonary vascular changes might partly explain this impaired DLCO, in the absence of pulmonary fibrosis.

Chest CT is considered the most accurate non-invasive imaging method for pulmonary disease assessment [106]. Some studies on quantifying vascular tree morphology based on CT show promising performances for assessing pulmonary vascular disease [12, 60, 62, 66, 63, 58]. Understanding the relation between vascular structure and pulmonary function may provide specific measurements for evaluating the response to treatment or measuring the severity of pulmonary vascular disease. The aim of this study was to test whether vascular changes were related to impaired gas transfer in SSc patients without fibrosis. To this end, we developed an objective and automatic method to quantify the pulmonary vascular morphology and studied the association between these CT-derived imaging biomarkers and pulmonary function.

4.2 Materials and Methods

4.2.1 Patients

We studied a cohort of 333 consecutive patients who had participated in our annual care program, between April 2009 and October 2015 [92]. The local Medical Ethical Committee approved the protocol and all patients gave written informed consent for collection of clinical and diagnostic data contributing to the biobank of the Leiden Combined Care in SSc (CISS) cohort. From this cohort, 83 patients had a chest CT scan where visual CT scoring showed no fibrosis and had PFTs measured within 8 days of the CT scan. Among these patients, image quality was insufficient for six patients to perform an accurate vascular analysis. Thus, 77 patients were selected for this study. Based on the degree of skin involvement, three subtypes of patients were classified: diffuse cutaneous SSc (DcSSc) with skin involvement proximal to the elbows and knees; limited cutaneous SSc (LcSSc) with skin involvement distal to the elbows and

knees; limited non-cutaneous SSc (LSSc) without skin involvement [107]. The group consisted of 43 never-smokers, 31 ex-smokers and three current smokers.

PFTs were performed under ERS/ATS guidelines [94, 93], including total lung capacity (TLC), forced vital capacity (FVC), forced expiratory volume in 1 second (FEV1) and single-breath diffusion capacity for carbon monoxide corrected for haemoglobin concentration (DLCOc). PFT results were expressed as a percentage of the predicted value (%predicted) [94, 93]. The DLCOc percentage of predicted (DLCOc %predicted) was selected as key outcome measure of gas transfer.

The systolic pulmonary artery pressure (sPAP) was estimated using echocardiography with a commercially available system (Vingmed Vivd7, General Electric Vingmed Ultrasound, Milwaukee, WI, USA). The sPAP was calculated from the tricuspid regurgitation peak gradient and the addition of right atrial pressure [108]. Patients with suspected pulmonary hypertension (PH, echocardiographic sPAP>40 mmHg) were tested by right heart-catheterization (RHC). If the mean pulmonary artery pressure (mPAP) was > 25 mmHg, the individual was diagnosed with PH [109, 110]. Furthermore, the mPAP, cardiac output (CO), pulmonary vascular resistance (PVR) and pulmonary artery wedge pressure (PAWP) were collected and used for determining the type of PH, under the 2015 ESC/ERS guidelines [29]. All patients were scanned with the same CT scanner (Aquilion 64, Toshiba Medical Systems, Otawara, Japan), with full inspiration and without contrast enhancement. The CT settings were: tube voltage = 120kV; tube current=140mA without modulation; rotation time = 0.4s; collimation = 64Ö0.5mm; helical beam pitch = 0.8; images were reconstructed with 0.5 mm slices [25]. Two observers (L.K. and A.S.), who were blinded to the patients' clinical information, scored the CT scans in consensus [11], at five levels: 1) origin of the aortic arch branches; 2) main carina; 3) pulmonary venous confluence; 4) halfway between the third and fifth section; 5) immediately above the right hemi-diaphragm. At each level, six variables were scored as percentages: total disease extent; proportion of ground-glass; extent of reticular pattern; coarseness of reticular disease; extent of emphysema; and presence of bronchiectasis. Patients with 0 percent in all 30 variables were considered to have no parenchymal abnormalities. Patients involved in this study were without any suspicion of pulmonary veno-occlusive disease (PVOD), as the CT scans did not show any signs of ground glass opacities, septal thickening or lymphadenopathy.

4.2.2   CT analysis

For lung segmentation, we employed multi-atlas based methods to flexibly capture anatomical variations, using Elastix registration toolbox [95]. Details on the atlas-based segmentation method can be found in the online supplements. The final segmentation included both left and right lungs. Within each lung, the vascular

Table 4.1: Patient group characteristics

Number of subjects	77
Female n [%]	67 [87]
Age (year)	49.9 ± 14.2
BMI (kg/m^2)	24.6 ± 5.24
sPAP (mmHg) <n=77>	26.9 ± 10.4
mPAP (mmHg) <n=3>	40.3 ±11
CO (L/min) <n=3>	5.17 ± 0.9
PVR (dyn·s/cm^5) <n=3>	405.3 ± 149
PAWP (mmHg) <n=3>	11 ± 2.6
MRSS	3.38 ± 4.28
Type of SSc n [%]	
DcSSc	8 [10.4]
LcSSc	51 [66.2]
LSSc	18 [23.4]
Autoantibodies, n [%]	
ANA	74 [96.1]
Anti-Scl-70 #	4 [4.2]
Anticentromere *	53 [68.8]
RNA polymerase III	1 [1.3]
Pulmonary function (% predicted)	
DLCOc	70.4 ± 16.7
FVC	107 ± 17.4
FEV$_1$	98.9 ± 16.8
TLC	95.7 ± 12.2
CT-derived measurements	
α	-1.44 ± 0.2
β	10.1 ± 0.62
Lung Volume (L)	4.73 ± 1.24

1 patient with doubtful Anti-Scl-70; * 1 patient with missing data; sPAP, systolic pulmonary arterial pressure, obtained from echocardiography; DcSSc, diffuse cutaneous SSc; LcSSC, limited cutaneous SSc; LSSC, limited non-cutaneous SSc; ANA, antinuclear antibody; Anti-Scl-70, nti-topoisomerase; DLCOc, single-breath diffusion capacity for carbon monoxide corrected with the haemoglobin concentration; FVC, forced vital capacity; FEV$_1$, forced expiratory volume in 1 second; TLC, total lung capacity.

trees were detected by a graph-cuts method [83], where 'vesselness' and CT intensity were combined into a single cost function. Previously, we evaluated this graph-cuts method using the public data-set from VESSEL12 [69] and obtained accurate vessel segmentation results [111]. 3D views of extracted pulmonary vascular trees are shown in Figure 4.1 (a-c). The entire vascular tree, i.e. both arteries and veins, was automatically extracted and subsequently analysed. In this automatic analysis, the distribution of the different radii of the entire vascular tree was quantified by first calculating the radius within each vessel, then construct a histogram from these data and finally analyse the shape of this histogram, as detailed below.

At each location in the vascular tree, the radius was calculated by a skeletonization method (DtSkeletonization method of Mevislab 2.7 [53]). This method selects voxels that are located at the centre of a blood vessel by eroding the extracted vessels, and the corresponding radius is estimated by measuring the distance between the vessel boundary and the centre. Examples of 'skeletonized' vascular trees are shown in Figure 4.1 (d-f). Subsequently, the number of voxels in the vascular skeleton with a specific radius were counted, producing a histogram of the measured vascular radii. A logarithmic transformation was applied to the frequency of occurrence in order to obtain a linear relation between frequency and radius [112] (Figure 4.1 (g-i)). Thus, the index of each histogram bin represents the vessel radius and the height of the bin represents the logarithm of the number of voxels with that specific radius. We used robust linear regression (robustfit method of MATLAB R2016b [87]) to analyse each radius histogram, and obtained two biomarkers (α, β) corresponding to the slope and intercept of the linear regression, respectively. The slope parameter α reflects the relative contribution of small vessels compared to large vessels (quantifying pruning of small vessels and dilatation of larger vessels) and the intercept β is related to the number of pulmonary capillaries estimated by extrapolation to radius 0, which reflects the vascular tree's capacity. To normalize for inspiration level and lung size, CT-derived lung volume was measured from the lung segmentations. As the vessel radius calculation might be affected by voxel size, the voxel size was also recorded for each patient.

4.2.3   Statistical analysis

For patient characteristics, continuous variables were expressed as means with standard deviations (SD) unless stated otherwise, and categorical variables were expressed as frequencies and percentages. Correlation between DLCOc %predicted or FVC %predicted and age, BMI, sPAP, α, β, CT-derived lung volume were expressed in terms of Spearman's rho correlation. Multivariable linear regression was used to determine independent predictors of DLCOc %predicted. DLCOc %predicted was entered as a dependent variable; age, BMI, sPAP, FEV1 %predicted, TLC %predicted, FVC %
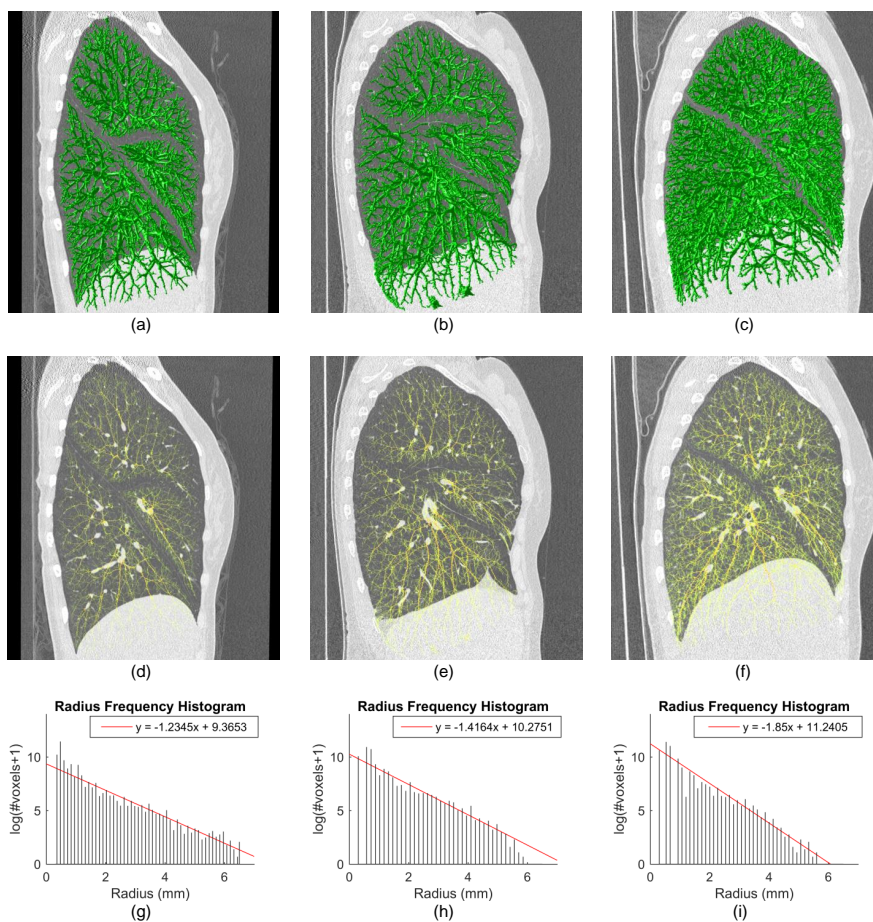
Figure 4.1: Three examples of vascular tree segmentation (a-c), vascular skeleton extraction from the corresponding vascular tree (d-f) and radius frequency histogram analysis of the vascular skeleton trees (g-i). Patient A, B and C had a DLCOc of 46%, 69% and 101.5% predicted, respectively, and lung volumes of 3.81, 6.2 and 4.23 litres, respectively. The loss of vascular tree capacity, i.e., a low intercept β and a flat slope α, is related to impaired gas transfer.

predicted α, β, voxel size and CT-derived lung volume were used as independent variables. A stepwise method was used for selecting significant independent predictors. The same analyses were performed on the subgroup of patients without PH (n=74), i.e. by excluding the three patients with PH confirmed by RHC. All statistical analyses were performed by using SPSS (version 20.0.0, Armonk, NY: IBM Corp.), and a 2-tailed p-value below 0.05 was considered statistically significant.

4.3   Results

The patient characteristics are shown in Table 4.1. In this study, 77 patients (mean age, 49.9 ± 14.2, including 67 females) were investigated, and the time difference between their CT and PFT is 1.19 ± 1.24 days. Among this studied patient group, three patients were confirmed with PH and were classified as pulmonary arterial hypertension (group 1), according to their CO, PVR and PAWP measurements. The average value of α and β were -1.44 ± 0.2 and 10.1 ± 0.62, respectively. Individually, age, α, β and sPAP were moderately but significantly correlated with DLCOc %predicted, as presented in Table 4.2. The age and sPAP were significantly and negatively correlated with DLCOc %predicted. The biomarker α had a significant negative correlation with DLCOc %predicted (R=-0.29, p-value=0.011), which implies that a less negative α (small-vessel pruning or large-vessel dilation) corresponds to a more impaired gas exchange (lower DLCOc %predicted). β had a positive significant correlation with DLCOc %predicted (R=0.32, p-value=0.004), which implies that a lower β (a low capacity of the vascular tree) corresponds to a more impaired gas exchange. The corresponding scatter plots are presented in Figure 4.2.

The results of the multivariable stepwise linear regression analysis for DLCOc %predicted as dependent variable are shown in Table 4.3. The multivariable step-wise regression analysis selected sPAP (coefficient=-0.78, 95%CI=[-1.07, -0.49], p-value<0.001), β (coefficient=8.6, 95%CI=[4.07, 13.12], p-value<0.001) and FEV1 %predicted (coefficient=0.3, 95%CI=[0.12, 0.48], p-value=0.001 as significant and independent predictors of DLCOc %predicted (R=0.71, p-value<0.001). By including β in the model, an additional 10% of variation in gas transfer could be explained (from R=0.56 to R=0.66).

For additional analysis, we evaluated the relationships between imaging biomarkers and pulmonary ventilation i.e. FVC % predicted. As presented in Table 2, the correlation between age, BMI, sPAP, α, β and FVC % predicted was not significant, whereas CT-derived lung volume was significantly correlated with FVC % predicted (R=0.41, p-value<0.001). Furthermore, the correlations between image biomarkers and sPAP were investigated. The correlation between sPAP and BMI (R=0.05, p-value=0.676), α (R=0.08, p-value=0.509), β (R=-0.01, p-value=0.92) and lung volume (R=-0.11, p-value=0.333) were not significant, while age had a significant
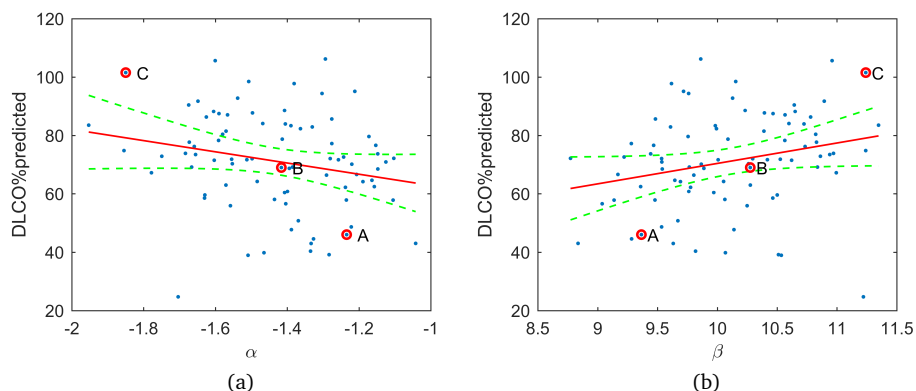
Figure 4.2: Correlation between imaging biomarkers and lung function (A, B and C are corresponding to patient A, B and C in Figure 1, respectively). (a) Correlation between α and DLCOc % predicted (R=-0.29, p-value=0.011); (b) Correlation between β and DLCOc % predicted (R=0.32, p-value=0.004)

Table 4.2: Correlations, R (p-value), between CT imaging biomarkers and PFTs.

	DLCOc % predicted	FVC % predicted
α	-0.29 (0.011)	-0.14 (0.243)
β	0.32 (0.004)	0.15 (0.187)
sPAP	-0.38 (0.001)	-0.01 (0.909)
BMI	0.19 (0.105)	0.26 (0.023)
Age	-0.29 (0.01)	0.14 (0.23)
Lung Volume	0.18 (0.12)	0.41 (<0.001)

correlation with sPAP (R=0.53, p-value<0.001). In the statistical analyses on the subgroup of patients without PH (n=74), α (R=-0.34, p-value=0.003) and β (R=0.42, p-value<0.001) were significantly correlated with DLCOc %predicted; β was the first selected independent predictor of DLCOc %predicted, followed by sPAP and FEV1 %predicted, in multivariable stepwise regression. The results of the subgroup analyses are shown in the online supplements.

4.4 Discussion

We studied the pulmonary vascular morphology among SSc patients without pulmonary fibrosis. An automatic method was applied to CT images (without contrast medium), for characterizing the pulmonary vasculature by quantifying the vascular system with a radius histogram analysis. To our knowledge, this is the first report on the relationship between pulmonary vascular tree capacity (the number of pulmonary

55

Table 4.3: Multivariable stepwise linear regression analysis for DLCOc %predicted (n=77).

| Parameter | Multivariable regression | |
	Regression Coefficient [95% CI]	p-value
Age	-	-
BMI	-	-
sPAP	-0.78 [-1.07, -0.49]	<0.001
FVC %predicted	-	-
FEV1 %predicted	0.3 [0.12, 0.48]	0.001
TLC %predicted	-	-
α	-	-
β	8.6 [4.07, 13.1]	<0.001
Voxel size	-	-
Lung Volume	-	-

capillaries estimated from CT) and gas transfer. Two CT-derived imaging biomarkers were introduced that are significantly correlated with DLCOc % predicted, demonstrating that gas transfer is associated with changes in vascular morphology. This may be useful in understanding the pathophysiology of this subgroup of SSc patients whose gas transfer deteriorates in the course of their disease without detectable pulmonary fibrosis.

Pulmonary vasculature was quantitatively assessed by two measurements, α and β. Biomarker α, the histogram slope, reflects the relative contribution of small vessels compared to large vessels, quantifying pruning of distal vessels and dilatation of the proximal vessels. Biomarker β, the histogram intercept, is estimated by extrapolation to radius 0 which provides an estimate of the vascular tree capacity, without actually detecting pulmonary capillaries. The biomarker α was significantly correlated with biomarker β (R=-0.91, p-value<0.001), implying that the reduction of vascular tree capacity could result in a change in the relative contribution of small vessels compared to large vessels. sPAP, β, FEV1 %predicted were selected by the stepwise method, whereas α, was excluded as it didn't explain additional DLCOc %predicted variation, probably due to the high correlation between α and β. To illustrate the effect of α and β (pruning/dilatation and vascular tree capacity), three patients are discussed in more detail (see Figure 4.1 and 4.2). Patient A with a low DLCOc % predicted obtained a flat slope α and a low intercept β, indicating vessel pruning/dilatation and a loss of vascular tree capacity, as compared to the other patients. This was confirmed by visual inspection of the vascular tree in Figure 4.1. Compared to patient B who had a moderate DLCOc %predicted, α and β, patient C had a higher DLCOc %

predicted, lower α value and higher β value, which implied that a better gas transfer corresponds to a lower vessel pruning/dilatation and higher vascular tree capacity. As the studied patient group consisted of SSc patients without pulmonary fibrosis, CT-derived lung volume was considered to reflect the total lung capacity. Since the voxel size might affect the vascular morphology measurements, voxel size was entered as independent variable in the multivariable linear regression. It proved, however, to be a non-significant factor in predicting gas transfer.

DLCOc % predicted and FEV1 % predicted correlated significantly in our study population (R=0.4, p-value=0.001). In the multivariable linear regression, the FEV1 % predicted was a significant independent predictor of DLCOc % predicted, which implies that pulmonary gas transfer was associated with pulmonary ventilation (air flow). The sPAP had a negative and significant correlation with DLCOc % predicted, and the sPAP was a significant predictor of DLCOc % predicted in the multivariable linear regression, which indicates that pulmonary pressure (blood flow) could affect gas transfer. In the subgroup of patients without PH, the performance of the biomarkers in predicting gas transfer was similar to those of the whole patient group, which implies that excluding or including these three PH patients did not change the validity of the biomarkers.

Several aspects of the correlation between β and DLCOc % predicted as well as the influence of FVC require some clarification. The correlation between DLCOc % predicted and β may be influenced by the position of the patient in both measurements (i.e. the sitting position during gas transfer studies and the supine position during chest CT). Two determinants of DLCO, membrane diffusing capacity (Dm) and capillary blood volume (Vc), have been known to be affected by posture and gravity. A postural change from sitting to the supine position in normal gravity, where some degree of heterogeneity between dependent and nondependent lung region persists, can result in an increase in Vc and not Dm, and an overall increase in DLCO up to 15% [105, 113]. Therefore, it seems plausible that this could have weakened the correlation between β and DLCOc % predicted. Furthermore, since α and β have not been evaluated in normal subjects, values between the "upper and lower limit of normal" of α and β may exist in our study population. This may be another factor that could have led to weakening the correlation between β and DLCOc % predicted. However, the protection of healthy individuals against radiation exposure prevents us from prospectively measuring α and β in CT images from normal controls, and retrospectively collecting negative CT examinations generally lacks confirmation by pulmonary function tests and these CT scans are usually contrast enhanced affecting the vascular morphology analysis.

Currently, studies on quantifying vascular tree morphology with CT imaging also showed promising results for assessing pulmonary vascular pathology associated with other pulmonary diseases. In COPD related studies [12, 60], the pulmonary vessel

morphology was quantified using CT scans without contrast as the percentage of small vessels i.e. vessels with cross-section area less than 5 mm^2 (%CSA<5 mm^2). The quantification had a weak but significant correlation with PFTs [60], and a significant negative correlation with mPAP [12]. Furthermore, smoking-related COPD is characterized by distal pruning of the small vessels which was assessed with the ratio between small vessel volume with CSA<5 mm^2 and total blood vessel volume (BV5/TBV) [62]. In one pulmonary hypertension study [66], pulmonary vascular morphology was quantified with contrast-enhanced chest CT in 24 patients (18 with and 6 without PH). Vascular remodelling characterized by vessel tortuosity and 3D fractal dimensions correlated significantly with RHC measurements. Furthermore, in chronic thromboembolic pulmonary hypertension (CTEPH), the disease was quantified as pulmonary morphologic changes with CT scans [65], including pruning of the distal vessel and dilation of the proximal vessels which were measured with the ratio BV5/TBV and the ratio BV>10/TBV (where BV>10 is the blood volume for all vessels with a CSA>10 mm^2), respectively. These biomarkers differed significantly between CTEPH patients and control individuals, and they correlated with RHC measures. In this study quantification on portions of pulmonary vascular system based on CSA or quantification of the pulmonary vascular fractal dimension was performed. In our study, however, we considered the pulmonary vessels as a continuous system, by quantifying vascular changes including all vessel radii by histogram analysis, instead of analysing only parts of the vascular tree. This yielded two biomarkers, α and β, that characterized the vascular tree in a more global approach and showing an association with gas transfer.

There are some limitations in our analysis. The automatic method used in the present study could not distinguish arteries from veins. As vascular changes may differ between arteries and veins, improved correlation may be expected with arteries evaluated separately from veins. However, even without this distinction, we already found a significant association with gas transfer. Also, we assessed both lungs together for each patient. More specific analysis of separate lungs or lung lobes may provide a more localized assessment of vascular changes. All patients in this study were scanned by the same scanner, thus, when adopting the automatic method to other CT scanners, the parameters for vessel extraction might need to be adjusted. The studied group only included SSc patients without a control group. Data on normal vasculature morphology of healthy people would enhance our understanding. Nevertheless, our method was still able to detect variances in the pulmonary vasculature. Due to a lack of pathology specimens in these SSc patients, validation of the imaging measurements against pathology was not possible. In the future, we aim to prospectively follow-up changes in the pulmonary vascular morphology in these patients over time, and evaluate if these subtle changes precede functional changes in pulmonary testing.

Studying the morphological changes of pulmonary vasculature in the patients with PH related diseases, such as chronic thromboembolic pulmonary hypertension, is also an interesting point of our future work, as the metric of morphological changes could help to predict an early development or monitor effects of treatment.

4.5   Conclusion

In conclusion, we characterized the pulmonary vasculature by two CT-derived imaging biomarkers from vascular radius analysis. These two imaging biomarkers, indicating small-vessel-pruning/large-vessel-dilation and loss of vascular tree's capacity, are associated with decreased gas transfer in the studied SSc patient group. The method may help understand the relationship between pulmonary vascular changes in SSc and lung function, in the absence of detectable fibrosis.

Supplementary

Segmentation methods

Three atlases that were labelled manually by pulmonary experts with Pulmo CMS software [114] were taken as moving image, and patient images were taken as fixed images. The torso masks were generated automatically using Pulmo-CMS, and were used to eliminate the influence of external objects on image registration quality. The registrations included an affine registration to tackle differences in the body positioning and a B-spline deformable registration to tackle anatomical differences in lung shape. The B-spline transformation model was subsequently used to transform the lung mask from the moving to the fixed image. After these procedures, three candidate lung masks corresponding to three atlases were fused by majority voting.

For lung vessels segmentation, a number of methods have been proposed in the literature. According to the challenge "Vessel Segmentation in the Lung 2012" (VESSEL12) [41], vesselness filters based on analysing the eigenvalues of the Hessian matrix were most successful. However, due to the low response at vessel boundaries and bifurcations, and the non-uniform response between vessels of different radii, extracting lung vessels by simply thresholding the vesselness is not sufficiently accurate for pulmonary vessel radius analysis. In this study, we therefore used a graph-cuts based method for the ultimate lung vessel segmentation, with a specifically designed cost function. The details on this vessel segmentation method have been described previously [111]. All image processing experiments were performed on a local PC with 24 GB RAM memory, Intel Xeon W3520 CPU with 4 cores, with 64-bit Windows 7 Professional OS.

Table A1. Evaluation of the multi-atlas based lung volume segmentation method.

ID	Dice	HausdorffD	AveSurfaceD	StdSurfaceD
1	0.987	23.431	0.355	0.895
2	0.986	23.791	0.431	1.077
3	0.986	27.677	0.466	1.210
4	0.960	39.064	1.468	2.521
5	0.986	19.672	0.515	0.986
6	0.989	24.062	0.423	1.015
7	0.984	23.622	0.490	1.061
8	0.982	23.087	0.593	1.410
9	0.988	21.633	0.497	1.056
10	0.987	32.265	0.508	1.150
11	0.987	21.749	0.435	0.929
12	0.977	30.887	0.905	2.135
13	0.977	26.926	0.818	1.982
14	0.989	22.226	0.403	0.894
15	0.980	24.000	0.643	1.259
16	0.987	24.352	0.394	1.132
17	0.988	20.518	0.455	1.166
18	0.987	23.043	0.442	1.092
19	0.986	27.586	0.458	1.075
20	0.987	23.622	0.491	0.986
Average	0.984	25.161	0.559	1.252

The unit of distance measurements is mm

Evaluation of lung segmentation

For the evaluation of our automatic lung segmentation method, 20 patients, who were randomly selected from SSc patients group, with manually labelled lung volume were used. Volume overlap similarity (Dice), maximum surface distance (Hausdorff distance HausdorffD), average surface distance (AveSurfaceD) and standard deviation of the surface distance (StdSurfaceD) were used for evaluating the multi-atlas-based lung segmentation method. As shown in Table A1, the average Dice of 20 patients was 0.984, the average Hausdorff distance was 25.161 mm, average AveSurfaceD was 0.559 mm and average StdSurfaceD was 1.252. From the Dice, AveSurfaceD and StdSurfaceD, it can be concluded that the segmentation method generally performed quite well. For the large Hausdorff distance, we visually checked the segmentation results and the maximum surface distance occurred at the border and corner of the lung region. Since vessels are rarely located at the lung boundary, these errors are not relevant and the ultimate segmentation results were reliable.

Evaluation of lung vessel segmentation

The public data-set of 20 CT scans from the VESSEL12 challenge was used for evaluating the vascular tree extraction method. The extracted lung vessels were submitted to the challenge organizer and evaluations were sent back. Our method obtained an area under the ROC curve (Az) of 0.975, which is a competitive performance on VESSEL12, especially among the binary submissions. The method performed well for the small vessels, medium vessels and large vessels, but for separating the airway wall, dense lesion and bronchi from the lung vessels, performance was less successful.

Results of subgroup (n=74) without PH

Among the patient group in this study, three patients out of 77 were confirmed in Pulmonary Hypertension (PH). To understand the biomarkers' effect in predicting gas transfer, the same statistical analyses were carried out in the subgroup (n=74) by excluding three PH patients. The results of Spearman's correlation analysis are presented in Table A3, where α (R=-0.34, p-value=0.003) and β (R=-0.42, p-value<0.001) were significantly correlated with DLCOc %predicted. From the results of multivariable stepwise regression, as demonstrated in Table A4, the biomarkers β (coefficient=8.33, 95% CI=[3.72, 12.9], p-value=0.001), was the firstly selected significant independent variables of DLCOc %predicted (R=0.65, p-value<0.001). Thus, in comparison with the statistical results of whole patient group, the performance of biomarkers in predicting gas transfer was the same, which implies that excluding or including three PH patients does not change the validity of biomarkers.

Discussion

For the automatic image processing methods used in this study, the atlas-based lung segmentation method was evaluated using 20 patients of in-house data against manually segmented lung fields labelled by experts. The results (Table A1) showed that the average Dice index was 0.984 and the average mean-surface-distance was 0.55 mm, which implies that our lung segmentation method is reliable. The lung segmentation method may be improved further by including more atlases. The graph-cuts based method, which was applied for vascular tree extraction, was evaluated with the public data set and obtained accurate results, especially among the binary vessel extraction methods. The graph-cuts method performed quite well for vessel segmentation for the small vessels, medium vessels and large vessels, but it failed to separate touching airway walls and vessels, which was caused mainly by similar intensity and adjacency between airway walls and vessels. Taking CT intensity into the cost function of the graph-cuts method made the detection of vascular boundaries and bifurcations more accurate, but the noise in CT produces a rough surface. To address this shortcoming, the subdivision method [115], which is a tube surface

Table A2. Characteristics of subgroup patients

Number of subjects	74
Female n [%]	65 [87.8]
Age (year)	49.2 ± 13.9
BMI (kg/m^2)	24.6 ± 5.34
sPAP (mmHg)	25.3 ± 5.95
MRSS	3.34 ± 4.36
Type of SSc n [%]	
DcSSc	8 [10.8]
LcSSc	48 [64.9]
LSSc	18 [24.3]
Autoantibodies, n [%]	
ANA	71 [95.9]
Anti-Scl-70 [#]	4 [5.5]
Anticentromere [*]	51 [68.9]
RNA polymerase III	1 [1.4]
Pulmonary function (% predicted)	
DLCO	71.9 ± 15.3
FVC	108 ± 16.6
FEV$_1$	100 ± 14.9
TLC	96.3 ± 11.7
CT-derived measurements	
α	-1.44 ± 0.2
β	10.1 ± 0.61
Lung Volume (L)	4.73 ± 1.23

[#] 1 patient with doubtful Anti-Scl-70. [*] 1 patient with missing data.

Table A3. Correlations, R (p-value) between CT imaging biomarkers and PFTs.

	DLCO % predicted	FVC % predicted
α	-0.34 (0.003)	-0.17 (0.154)
β	0.42 (<0.001)	0.24 (0.041)
sPAP	-0.30 (0.009)	0.11 (0.372)
BMI	0.22 (0.063)	0.29 (0.013)
Age	-0.22 (0.063)	0.24 (0.038)
Lung Volume	0.18 (0.133)	0.42 (<0.001)

Table A4. Multivariable stepwise linear regression analysis for
DLCOc %predicted (n=74).

| Parameter | Multivariable regression | |
	Regression Coefficient [95% CI]	p-value
Age	-	-
BMI	-	-
sPAP	-0.99 [-1.46, -0.53]	<0.001
FVC %predicted	-	-
FEV1 %predicted	0.33 [0.14, 0.52]	0.001
TLC %predicted	-	-
α	-	-
β	8.33 [3.72, 12.9]	0.001
Voxel size	-	-
Lung Volume	-	-

fitting algorithms with centreline as reference, might provide better surfaces and more accurate radius estimation. The skeletonisation method, which was carried out by a symmetric distance transform, would then provide accurate centres of the skeleton and estimate the radius reliably. However, with the current rough surface, some side branches may still remain, despite the removal of easily-distinguished side branches by the skeletonisation method [86]. Therefore, centreline tracing methods may be beneficial for removing these side branches.

5

Treatment Effect of Balloon Pulmonary Angioplasty in CTEPH, Quantified by Automatic Comparative Imaging in CTPA

This chapter was adapted from:

Abstract

Objectives Balloon pulmonary angioplasty (BPA) in patients with inoperable chronic thromboembolic pulmonary hypertension (CTEPH) can have variable outcomes. To gain more insight into this variation, we designed a method for visualizing and quantifying changes in pulmonary perfusion by automatically comparing CT pulmonary angiography (CTPA) before and after BPA treatment. We validated these quantifications of perfusion changes against hemodynamic changes measured with right-heart catheterization (RHC).

Materials and Methods We studied 14 consecutive CTEPH patients (12 females; age:70.5 ± 24), who underwent CTPA and RHC, before and after BPA. Post-treatment images were registered to pre-treatment CT scans (using the Elastix toolbox) to obtain corresponding locations. Pulmonary vascular trees and their centerlines were detected using a graph-cuts method and a distance transform method, respectively. Areas distal from vessels were defined as pulmonary parenchyma. Subsequently, the density changes within the vascular centerlines and parenchymal areas were calculated and corrected for inspiration level differences. For visualization, the densitometric changes were displayed in color-coded overlays. For quantification, the median and inter-quartile range (IQR) of the density changes in the vascular and parenchymal areas (ΔVD and ΔPD) were calculated. The recorded changes in hemodynamic parameters, including changes in systolic, diastolic, mean pulmonary artery pressure (ΔsPAP, ΔdPAP and ΔmPAP, respectively) and vascular resistance (ΔPVR), were used as reference assessments of the treatment effect. Spearman's correlation coefficients were employed to investigate the correlations between changes in perfusion and hemodynamic changes.

Results Comparative imaging maps showed distinct patterns in perfusion changes among patients. Within pulmonary vessels, the IQR of ΔVD correlated significantly with ΔsPAP (R=-0.58, p=0.03), ΔdPAP (R=-0.71, p=0.005), ΔmPAP (R=-0.71, p=0.005) and ΔPVR (R=-0.77, p=0.001). In the parenchyma, the median of ΔPD had significant correlations with ΔdPAP (R=-0.58, p=0.030) and ΔmPAP (R=-0.59, p=0.025).

Conclusions Comparative imaging analysis in CTEPH patients offers insight into differences in BPA treatment effect. Quantification of perfusion changes provides non-invasive measures that reflect hemodynamic changes.

5.1 Introduction

Chronic thromboembolic pulmonary hypertension (CTEPH) is caused by persistent obstruction of pulmonary arteries following pulmonary embolism [15]. The mechanical obstruction of pulmonary arterials is produced by fibrotic transformation of pulmonary thrombus [32], which could lead to pulmonary hypertension and increasing pulmonary vascular resistance (PVR). Without treatment, CTEPH patients have poor prognoses: 2-years survival rate is less than 50% in patients with mean pulmonary artery pressure (PAP) > 30 mmHg [18, 17]. The prognosis can be improved by pulmonary endarterectomy (PEA) [20] or balloon pulmonary angioplasty (BPA) [21], combined with optimal medications. PEA is the curative treatment for CTEPH, with nearly normalized hemodynamics in the majority of patients [22]. However, for patients with inoperable CTEPH, BPA can be an alternative treatment to improve the clinical status and hemodynamics with a low mortality [23].

Evaluation of disease severity and assessment of treatment effects play an important role in the therapy of CTEPH. In evaluating the severity of CTEPH and assessing treatment effects, invasive right-heart catheterization (RHC) serves as gold standard [31]. The 6-min walk distance (6MWD) [116] and the brain natriuretic peptide (BNP) level [117] are the most frequently used non-invasive measurements to quantify treatment effect. Non-invasive imaging techniques play a key role in both diagnosis of CTEPH and assessment of the treatment effect [32]. Radionuclide ventilation/perfusion (VQ) scans are recommended as an initial step in the diagnosis of CTEPH [31], but it is difficult to quantify treatment effects with VQ scans. CT pulmonary angiography (CTPA) is used in the evaluation of severity of CTEPH [34]. Compared with conventional pulmonary angiography, CTPA has benefits for providing additional details in high-resolution 3D images [118]. Recently, dual-energy CT has shown its capability in visualizing pulmonary vascular disease and assessing severity of CTEPH [119, 19].

BPA treatment can improve the hemodynamics of pulmonary vascular systems [23] and may contribute to the improvements of pulmonary vascular and parenchymal perfusion. We hypothesized that the perfusion changes achieved by BPA might reflect densitometric changes in CTPA. Thus, an objective and automatic method was designed to quantify the density changes in pulmonary vascular and parenchymal areas by comparatively analyzing CTPA before and after BPA. Moreover, we validated these image quantifications of perfusion changes against hemodynamic changes measured via RHC.

5.2   Materials and Methods

5.2.1   Patients

We studied a cohort of 14 consecutive patients (age, 70.5 ± 24, including 12 females) who were diagnosed with inoperable CTEPH and were treated with BPA between May 2013 and April 2016, referred to the Tohoku University Hospital. All studied patients underwent both CTPA and RHC examinations, before and after BPA treatment. All patients underwent several sessions of BPA procedures besides standard medication such as anticoagulants and vasodilators. As a vasodilator for symptoms prior to BPA, Riociguat, Tadarafil, Ambrisentan and Beraprost were used in 7, 5, 2 and 2 patients, respectively. During one procedure, the target lesion was limited to one or two segments in one lobe to minimize complications of BPA. We repeated BPA sessions at a 4–8 weeks interval [21]. Seven patients underwent the initial CTPA scan before the first BPA session; the other seven subjects had undergone a part of BPA sessions before the initial CTPA scan. The number of BPA sessions between the two CTPA exams ranged between 1 and 4 (median: 3). The intervals between CTPA and RHC were 0 to 37 days (median: 2 days). This prospective study was approved by the local ethics committee, and written informed consent was obtained from all patients.

All patients were scanned with a second generation dual-source CT scanner (SOMATOM Definition Flash; Siemens Healthcare GmbH, Forchheim, Germany) with inspirational breath-hold and contrast enhancement. Contrast enhancement containing 350 mg/mL iodine was injected at a speed of 0.075 mL/s/kg × body-weight (in kg) over a period of 6 s, and subsequently a 40 mL saline flush was delivered at the same injection speed via a 20-gauge intravenous catheter, placed in the right antecubital vein using a double-headed power injector. A test injection technique was used to determine the scan delay: 12 mL iodine-containing contrast medium followed by 20 mL saline. For each patient, a region of interest (ROI) was placed within main pulmonary artery and the time-density curve within the ROI was recorded. The dual-source CT scan commenced 1 s after the test injection-mediated enhancement peaked [19]. The X-ray tube settings (with automatic tube current modulation) were for tube A: voltage 80 kVp with a quality reference mAs of 141; and for tube B with a tin (Sn) filter: 140 kVp with a quality reference mAs of 60. Gantry rotation speed was 0.28 s per rotation, collimation 64 × 0.6 mm, pitch 1.00. Data was reconstructed with a slice thickness of 1 mm using a standard soft-tissue iterative reconstruction kernel (I30f, Sinogram Affirmed Iterative Reconstruction, [SAFIRE], strength 3). The 80 kVp and 140 kVp voltage images were fused into mixed images with a single energy of 120 kVp and with a mixing ratio of 0.6 : 0.4, using the dual-energy application software on a commercially available workstation (syngo CT Workplace, VA44A; Siemens Healthcare GmbH) [19]. Only the mixed CTPA images were investigated in this study.

The hemodynamic parameters were examined at the main pulmonary artery via RHC in all patients both before and after BPA treatment. These included PAP (systolic, diastolic and mean), systolic right ventricular pressure (RVP), right atrial pressure (RAP), cardiac output (CO), cardiac index (CI) and pulmonary capillary wedge pressure (PCWP). The PVR was calculated using the following formula: PVR = (mean PAP – PCWP)/CO × 80 (dyne·s/cm^5) [120]. The RHC examinations were used as gold standard to evaluate the severity of CTEPH [31], the changes in PAP (ΔsPAP, ΔdPAP and ΔmPAP) and in PVR (ΔPVR) after BPA treatment were calculated as the reference assessments for the treatment effects. 6MWD data were recorded for 13 out of 14 patients. BNP and mean transit time (MTT) were collected for all patients. The diameter of the pulmonary artery (PA) trunk was measured on axial images. Short axis measurements of the left and right ventricle (LV and RV, resp.) were performed in 4-chamber images, and the ratio between RV and LV short axes (RV/LV) was calculated. The interventricular septum was assessed on the mid-chamber short axis images. Interventricular septal angle (ISA) was measured by determining the angle between the mid-point of the interventricular septum and the two hinge points. These CT measurements were performed on a commercially available workstation (Aquarius Net; TeraRecon, San Mateo, CA).

5.2.2 Image analysis

CTPA scans were pre-processed with lung volume segmentation using multi-atlas based methods. Three atlases that were labeled semi-automatically by pulmonary experts using Pulmo-CMS software [114] were registered to each CTPA scan with Elastix [95]. Majority voting was used to fuse the labels and extract the final lung segmentation. Pulmonary vessels were extracted within the lung volume, using a graph-cuts based method [111], where the vessel-likelihood (so-called 'vesselness', measured by the strain-energy filter [68]) and CT intensity were combined into a single cost function. Both pulmonary arteries and veins were included as the entire pulmonary vascular trees.

For each patient, pairwise image registration was employed between CT images of post- and pre-BPA, using Elastix, as reported previously [121]. The volume correction in this method was originally designed for parenchymal areas only, as a measure to correctly assess emphysema progression, where a proportional local increase in volume (estimated by the determinant of the Jacobian) was compensated by a proportional decrease in density (called the 'dry sponge model'):

$$\Delta D(\boldsymbol{x}) = I_{post}(\boldsymbol{T}(\boldsymbol{x})) - I_{pre}(\boldsymbol{x}) \bullet [det \boldsymbol{J_T}(\boldsymbol{x})]^{-1} , \qquad (5.1)$$

where $\Delta D(\boldsymbol{x})$ is the estimated density change at position $\boldsymbol{x}$; $I_{pre}(\boldsymbol{x})$ and $I_{post}(\boldsymbol{x})$ are the image intensities of the pre- and post-BPA CT scan; $\boldsymbol{T}(\boldsymbol{x})$ is the transformation

function from the image registration, mapping the coordinate $\boldsymbol{x}$ in the pre-BPA scan to the corresponding position in the post-BPA scan; and $det\boldsymbol{J_T}(\boldsymbol{x})$ is the determinant of the Jacobian of the transformation field at position $\boldsymbol{x}$.

As the 'dry sponge model' is not applicable for the pulmonary areas with high density, where pure liquid in pulmonary vessels is not compressible, we modified the model to restrict the scaling factor ($det\boldsymbol{J_T}(\boldsymbol{x})$) depending on the density. This so-called 'restricted sponge model' considers a voxel as composed of two components, air and liquid. Then density can be increased by leaving out the air component, and the density is only allowed to decrease by a maximum of 4 times the original volume of the air component (see Figure 5.1 A). This means that the scaling factor is allowed to range from 0 to 4, if a voxel contains only air. For a voxel containing 100% water, blood or contrast agent (i.e. densities higher than 1000 gram/L) which is not compressible, then the scaling factor is set to 1. And for voxels with original densities between 0 and 1000 gram/L, linear lower and upper bounds for the scaling factor are used (see Figure 5.1 B). Therefore, the sponge model in Equation 5.1 was modified as follows:

$$\Delta D(\boldsymbol{x}) = I_{post}(\boldsymbol{T}(\boldsymbol{x})) - I_{pre}(\boldsymbol{x}) \bullet C(\boldsymbol{x})^{-1}$$
$$C(\boldsymbol{x}) = max\left\{\theta_{min}\left(I_{pre}(\boldsymbol{x})\right), min\left\{\theta_{max}\left(I_{pre}(\boldsymbol{x})\right), det\boldsymbol{J_T}(\boldsymbol{x})\right\}\right\}, \tag{5.2}$$

where θ_{min} and θ_{max} are the linear lower and upper bound, respectively.

In order to eliminate the dependence on a perfect matching quality between follow-up and baseline at the vascular boundary regions, we extracted only the centerlines of vessels by the symmetric distance transform method (DtSkeletonization method of Mevislab 2.7 [86]). Subsequently, only the voxels on the vascular centerlines were used for quantifying the density changes which were estimated with Equation 5.2. For visualization, the 'densitometric change' map was displayed as color-coded overlays as shown in Figure 5.2 (a, d) and 3D color-coded vascular centerlines were generated, as illustrated in Figure 5.2 (b, e). For quantification, the median and inter-quartile range (IQR) of the vascular densitometric changes (ΔVD) were calculated, as shown in Figure 5.2 (c, f), which were used to quantify the perfusion changes within vessels. The densitometric changes in parenchyma (ΔPD) were measured at the location of parenchymal 'centerlines' which are the parenchymal areas distal to pulmonary vessels. Similarly, the perfusion changes in pulmonary parenchyma were quantified by the median and IQR of the ΔPD.

5.2.3 Statistical analysis

Continuous variables of the patient characteristics are presented as the median and interquartile range, and categorical variables are presented as frequencies and percentages. The normality of each variable was tested with a Shapiro-Wilk test and a normal Q-Q plot. The changes in RHC parameters, 6MWD, BNP levels, MTT,
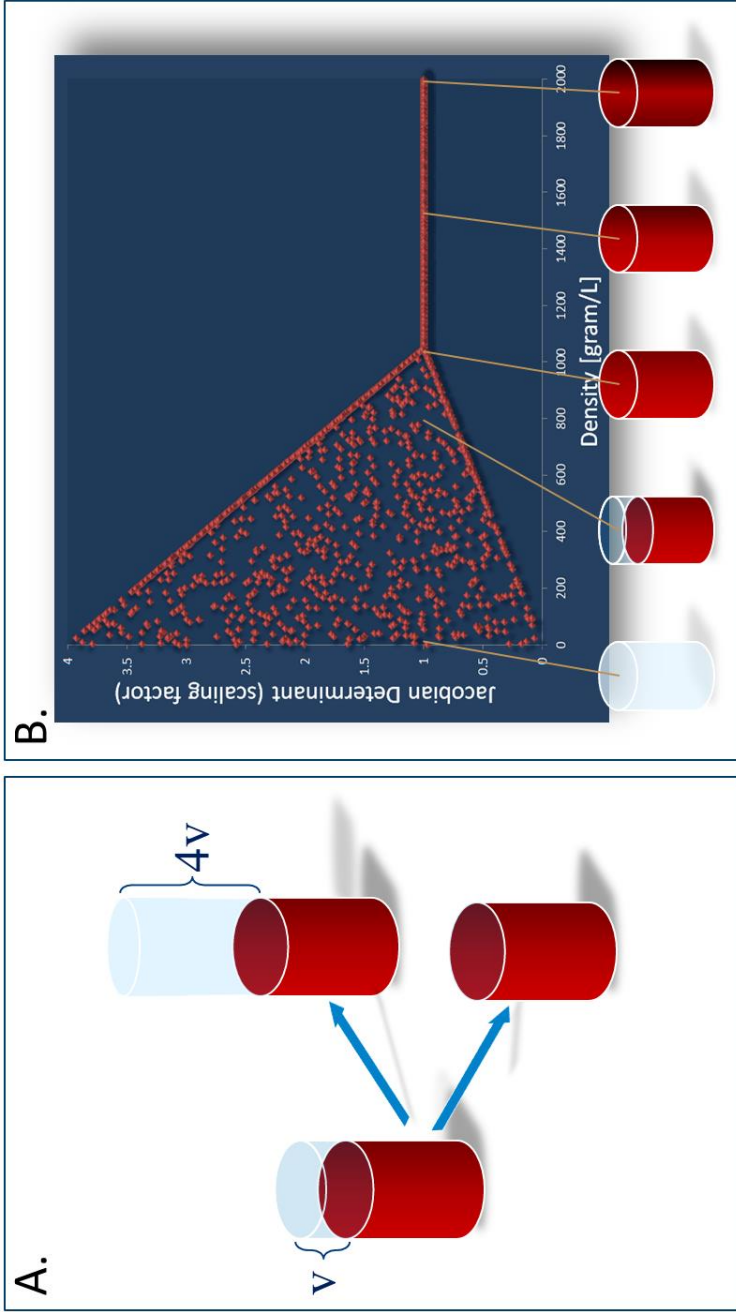
Figure 5.1: A) Two-component model: a voxel is composed of an air and blood compartment (or water or contrast agent), where density increase is restricted to the situation where all air has been expired, or where there is a 4 fold increase of the amount of inspired air. B) The scaling factor from the determinant of the Jacobian is thus restricted by an upper and lower limit depending on the density of a voxel.
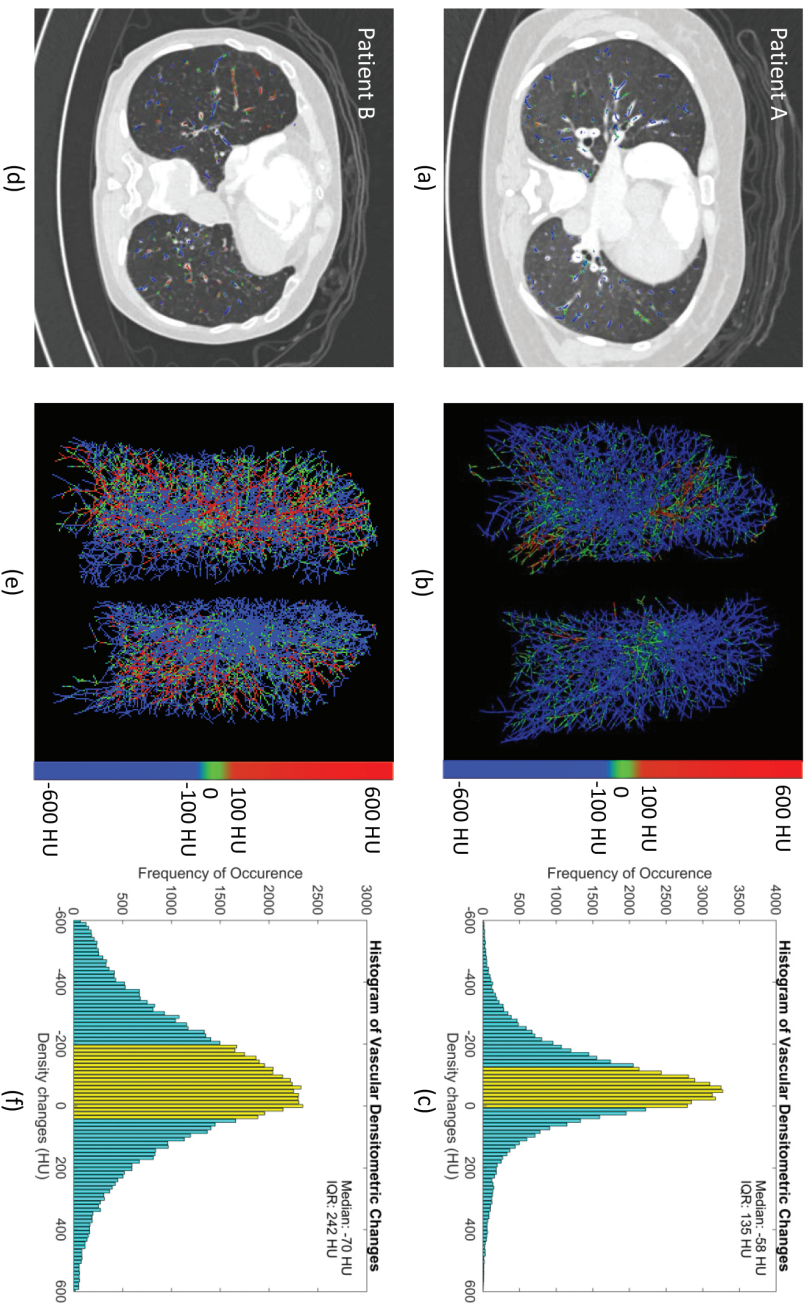
Figure 5.2: Vascular densitometric changes of two patients. (a, d) one slice of CTPA with color-coded overlay of vascular densitometric changes; (b, e) 3D color-coded visualization of vascular centerlines; (c, f) histogram of vascular densitometric changes and yellow bins representing vascular densitometric changes within the IQR. Patient A and B had a decrease in mPAP by -3 and -34 mmHg, respectively and a decrease in PVR by -39 and -734 dyne·s/cm^5, respectively.

Table 5.1: Changes in hemodynamic parameters, 6MWD, BNP, MTT, RV/LV ratio, PA diameter, ISA and densitometry.

	Pre-BPA	Post-BPA	Change	p-value
RHC parameters				
sPAP (mmHg)	60.5 ± 33	36 ± 19	23 ± 19	0.002
dPAP (mmHg)	20 ± 16	12.5 ± 11	-5 ± 11	0.006
mPAP (mmHg)	34.5 ± 17	21.5 ± 15	-12.5 ± 14	0.003
PVR (dyne·s/cm^5)	496 ± 396	246 ± 185	-185 ± 409	0.004
6MWD (m)	450 ± 159	510 ± 95	50 ± 115	0.004
BNP (pg/ml)	80.4 ± 160	26.8 ± 32.7	-53.2 ± 146	0.01
MTT (seconds)	10.1 ± 2.95	9.95 ± 2.1	-0.05 ± 2.08	0.31
RV/LV ratio	1.21 ± 0.53	1.05 ± 0.1	-0.09 ± 0.28	0.005
PA diameter (mm)	30.1 ± 6.22	28.6 ± 5.54	-1.9 ± 3.43	0.024
ISA (degree)	131 ± 11.8	130 ± 16.2	-2.5 ± 27.5	0.397
Density measurements (HU)				
Median VD	-415 ± 101	-433 ± 114	-51.5 ± 20.8	<0.001
IQR of VD	437± 73	475 ± 67	182 ± 60	<0.001
Median PD	-864 ± 47	-861 ± 54	-3.5 ± 22.5	0.379
IQR of PD	437 ± 73	475 ± 67	45 ± 15	<0.001

BPA indicates balloon pulmonary angioplasty; sPAP, systolic pulmonary artery pressure; dPAP, diastolic pulmonary artery pressure; mPAP, mean pulmonary artery pressure; 6MWD, 6-minute walk distance; BNP, brain natriuretic peptide; MTT, mean transit time; RV/LV ratio, right ventricular short axis to left ventricular short axis ratio; PA diameter, diameter of pulmonary artery trunk; ISA, interventricular septal angle; VD, vascular density; PD, parenchymal density.

RV/LV ratio, PA diameter, ISA and density measurements between pre- and post-BPA were tested using the paired t-test or the Wilcoxon signed-rank test, as appropriate. Correlations between hemodynamic changes, 6MWD, BNP and densitometric changes were evaluated using Spearman's correlation coefficient. All statistical computations were performed in SPSS (Version 20.0. Armonk, NY: IBM Corp.). A 2-tailed p-value<0.05 was considered to be statistically significant.

5.3 Results

The changes in RHC parameters, 6MWD, BNP, MTT, RV/LV ratio, PA diameter, ISA and perfusional quantifications between pre- and post-BPA are shown in Table 5.1. The hemodynamic parameters were improved by the BPA treatment, with a statistically significant decrease in sPAP, dPAP, mPAP and PVR. The 6MWD, BNP, RV/LV ratio and PA diameter were also significantly improved by the BPA treatment. The median densities decreased within the vascular trees after BPA, as quantified by automatic

Table 5.2: Correlation R (p-value) analysis between RHC parameters, 6MWD, BNP and image-derived perfusion changes.

	Median of ΔVD	IQR of ΔVD	Median of ΔPD	IQR of ΔPD
ΔsPAP	0.53 (0.054)	-0.58 (0.031)	-0.32 (0.263)	-0.18 (0.529)
ΔdPAP	0.18 (0.536)	-0.71 (0.005)	-0.58 (0.030)	-0.40 (0.152)
ΔmPAP	0.46 (0.095)	-0.71 (0.005)	-0.59 (0.025)	-0.37 (0.190)
ΔPVR	0.28 (0.325)	-0.77 (0.001)*	-0.43 (0.121)	-0.36 (0.201)
Δ6MWD	-0.67 (0.012)	-0.011 (0.817)	-0.011 (0.971)	0.48 (0.093)
ΔBNP	0.10 (0.725)	-0.53 (0.052)	-0.39 (0.163)	-0.65 (0.013)

* significance level obtained after Bonferroni correction for multiple testing.

comparative imaging analysis (see Table 5.1). In the parenchyma on the other hand, the median densities did not change significantly.

The results of Spearman's correlation analysis between change in RHC parameters and change in densities are provided in Table 5.2. The IQR of ΔVD was significantly negatively correlated with all RHC parameters: ΔsPAP (R=-0.58, p=0.03), ΔdPAP (R=-0.71, p=0.005), ΔmPAP (R=-0.71, p=0.005) and ΔPVR (R=-0.77, p=0.001), which indicates that a wider inter-quartile range of ΔVD histogram corresponds to a larger decrease in both PAP and PVR after BPA treatment. Scatter plots of the hemodynamic changes and IQR of ΔVD are presented in Figure 6.3, among which the significant association between ΔPVR and IQR of ΔVD was particularly strong. Besides, the median of ΔPD was significantly correlated with both ΔdPAP (R=-0.58, p=0.030) and ΔmPAP (R=-0.59, p=0.025), which implies that the perfusion changes of pulmonary parenchyma could partly reflect the hemodynamic parameters changes. The Δ6MWD was significantly correlated with the Median of ΔVD (R=-0.67, p=0.012), and ΔBNP had a significant correlation with the IQR of ΔPD (R=-0.645, p=0.013).

5.4 Discussion

We studied the pulmonary perfusion changes in CTPA of CTEPH patients before and after BPA treatment. The CTPA before and after BPA treatment were compared by an automatic and objective method for identifying the perfusion changes in pulmonary vessels and parenchyma. The median and IQR of perfusion changes in pulmonary vessels and parenchyma were validated against RHC parameters changes. The IQR of ΔVD were significantly correlated with all PAP measurements and PVR, indicating that the hemodynamic changes could be reflected by perfusion changes. Furthermore, the color-coded visualization can offer insight into localized differences in BPA treatment effect.

The variety in perfusion changes in pulmonary vessels was quantitatively assessed
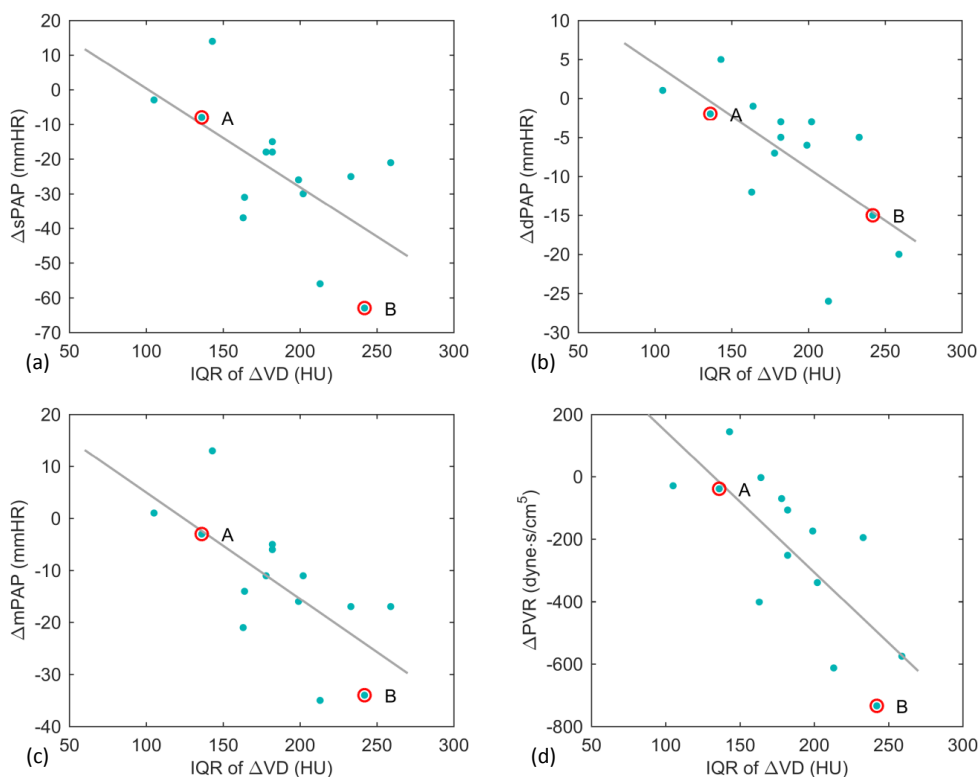
Figure 5.3: Correlation between IQR of ΔVD and RHC parameters (A and B are corresponding to patient A and B in Figure 5.2, respectively). (a) Correlation between IQR of ΔVD and ΔsPAP (R=-0.58, p-value=0.031); (b) Correlation between IQR of ΔVD and ΔdPAP (R=-0.71, p-value=0.005); (c) Correlation between IQR of ΔVD and ΔmPAP (R=-0.71, p-value=0.005); (d) Correlation between IQR of ΔVD and ΔPVR (R=-0.77, p-value=0.001).

by IQR of ΔVD, as it reflects the spread of both decrease and increase in density within pulmonary vessels. Vessels proximal to an obstruction ('upstream vessels') react differently to BPA treatment than vessels distal to obstruction ('downstream vessels'). Due to the obstructions in pulmonary arteries before treatment, contrast medium would accumulate in the 'upstream vessels' where hypertension leads to dilation and increased density in CTPA. The 'downstream vessels', however, are initially not reached by contrast medium and their densities in CTPA would therefore be lower than normal. When obstructions have been treated by BPA, the distribution of contrast medium through the pulmonary vascular system may be normalized. Therefore, the contrast medium is distributed more homogeneously after BPA, i.e. the densities in 'upstream vessel' would have decreased and densities in 'downstream vessels' would

have increased after treatment. Thus, a wider range in ΔVD implies more equalization of contrast medium in vessels, i.e. more hemodynamic improvements.

In order to demonstrate the visualization of the changes in the quantified parameters, two patients with different outcomes after BPA were selected. According to RHC assessments, patient B had a larger decline in PAP and PVR after BPA treatment in comparison with patient A. As shown in the histogram of vascular densitometric changes, the IQR of patient B is wider than patient A. In the color-coded 2D visualization (Figure 5.2 a and d), most of the vascular tree in patient A is coded in green, whereas in patient B more blue- and red-coded vessels are displayed. This implies that perfusion changes in patient B are more widely spread, i.e. a better treatment effect.

In the pulmonary parenchyma, the hemodynamic changes obtained from RHC were reflected by the median ΔPD, not by the IQR of ΔPD. Due to the poor performance of the pulmonary vascular system before BPA treatment, transport of contrast medium to the parenchymal areas may be limited. After the BPA treatment, the performance of the vascular system might have been improved. Thus, instead of the variation in ΔPD, the median of ΔPD will provide insights into the perfusion changes in pulmonary parenchyma. The median of ΔPD was not significantly different from 0, while it was significantly correlated with ΔdPAP and ΔmPAP. The median of ΔPD did not change on average, however, its increases/decreases in an individual patient might moderately reflect the changes in RHC parameters. Although the information from ΔPD quantifications is not as clear as that from ΔVD, investigating changes in the pulmonary parenchyma shows potential.

Recently, several studies demonstrated the significant treatment effect of BPA by cautiously limiting the number of balloon inflations and target segments per session, and thus reducing the incidence of adverse complications, such as reperfusion edema and pulmonary bleeding [15]. This procedure was added to treatment algorithms in the ESC/ERS guideline [29]. However, its efficacy for long-term prognosis has not been established yet. In our clinical setting as an experienced CTEPH center, though rare, there are patients demonstrating re-exacerbation of CTEPH, year(s) after completion of BPA treatment courses. Considering the features of BPA procedure and patients' clinical course, several follow-ups are necessary in the management of patients with CTEPH. Our results provided objective and quantitative changes of pulmonary perfusion after BPA along with densitometry information on CTPA, which were correlated with invasive RHC exams.

Some previous studies have reported methods for estimating the severity of CTEPH. A study [122] validated automatic quantification of pulmonary perfused blood volume (PBV) with cardiac index, PAP, PVR, and 6MWD in 25 CTEPH patients. The PBV had negative significant correlations with sPAP and mPAP, but not significant with PVR, CI

and 6MWD. In another study [19], authors manually measured lung PBV to correct the influence of artifacts and evaluated the PBV with PAP, PVR and RVP for 46 CTEPH patients. The lung PBV was significantly correlated with sPAP, dPAP, mPAP and PVR. The manually measured PBV might be used as a non-invasive estimator of clinical CTEPH severity, however, reproducibility and objectivity of manual visual evaluations are generally poor. The pulmonary vascular morphology was investigated as an imaging biomarker for CTEPH in a recent study [63], in which the ratio of small-vessels volume (blood volume of vessels with a cross-sectional area of $\leq$ 5mm^2 , BV5) and total blood vessel volume (TBV) was measured for small-vessels pruning, and the ratio of large-vessels (a cross-sectional area of >10mm^2 , BV>10) and TBV was quantified for large-vessels dilation. The measurements were extracted in CTPA for 18 patients with CTEPH and 15 control patients. The quantifications of BV5/TBV and BV>10/TBV were significantly different between the CTEPH and control group, implying that pulmonary vascular morphology was remodeled by CTEPH. The pulmonary vascular morphology may be used as an imaging biomarker to assess disease severity. In another study [123], the lung PBV was quantified by dual-energy CT in 8 female patients with CTEPH pre- and post-BPA treatment and corrected with pulmonary artery enhancement (lung PBV/PAenh). The pre- to post-BPA improvements in both-lung PBV/PAenh had significant positive correlations with PAP, PVR and 6-minute walking distance, which implied that the lung PBV might be an indicator of BPA treatment effect. Optical Coherence Tomography (OCT) was used to classify the morphologies of 43 lesions in 17 patients pre- and post-BPA in another study [124]. The newly proposed OCT-based morphologic lesion classification was evaluated to the pressure ratio and compared with conventional angiographic findings, which proved to be promising to predict accurate estimation of lesion responsiveness to BPA. In this study, the IQR of ΔVD can be used as a measurement to assess the treatment effect and additionally offers color-coded visualization back to CTPA. Furthermore, we compared CTPA before and after treatment, which offers insight into the treatment effect.

There are some limitations in our study. The quantifications were performed on both lungs together. More specific analysis of separate lungs or lung lobes may provide a more localized and accurate assessment of perfusion changes. We did not obtain an echocardiogram or MRI data along with the CT exam to evaluate cardiac output. The post contrast attenuation was not normalized for intra-individual variations that might be influenced by cardiac output. In the present study, the arteries and veins were not analyzed separately with an automatic method, whereas perfusion changes may differ between arteries and veins. A separated analysis of arteries and veins may therefore further improve the correlation. Nevertheless, even without these particular analyses, we already found a highly significant association between perfusion changes and hemodynamic changes. In the future, quantifying the vessels with lesions treated by

BPA would be an interesting research topic, as automatic and objective quantifications of the lesion morphology could provide specific benefits for planning or assessing BPA treatment. The studied group was relatively small and only included CTEPH patients without a control group. The normal vascular perfusion in healthy people might contribute to enhance the understanding of relations between pulmonary vascular perfusion and hemodynamic parameters. However, the method still offers insight into the variance in BPA treatment effects.

5.5 Conclusion

In conclusion, PAP and PVR were significantly improved after BPA, in the studied patient group with inoperable CTEPH. We assessed the perfusion changes in pulmonary vasculature achieved by BPA using an automatic comparison of CTPAs acquired before and after treatment. The IQR of ΔVD is associated with hemodynamic changes and can be used as a non-invasive measurement for assessing BPA treatment effects. The color-coded visualization provides insight into local differences in BPA treatment effects.

6

Pulmonary vessel tree matching for quantifying changes in vascular morphology

Abstract

Invasive right-sided heart catheterization (RHC) is currently the gold standard for assessing treatment effects in pulmonary vascular diseases, such as chronic thromboembolic pulmonary hypertension (CTEPH). Quantifying morphological changes by matching vascular trees (pre- and post-treatment) may provide a non-invasive alternative for assessing hemodynamic changes. In this work, we propose a method for quantifying morphological changes, consisting of three steps: constructing vascular trees from the detected pulmonary vessels, matching vascular trees with preserving local tree topology, and quantifying local morphological changes based on Poiseuille's law (changes in $radius^{-4}$, $\triangle r^{-4}$). Subsequently, median and interquartile range (IQR) of all local $\triangle r^{-4}$ were calculated as global measurements for assessing morphological changes. The vascular tree matching method was validated with 10 synthetic trees and the relation between clinical RHC parameters and quantifications of morphological changes was investigated in 14 CTEPH patients, pre- and post-treatment. In the evaluation with synthetic trees, the proposed method achieved an average residual distance of 3.09 ± 1.28 mm, which is a substantial improvement over the coherent point drift method (4.32 ± 1.89 mm) and a method with global-local topology preservation (3.92 ± 1.59 mm). In the clinical evaluation, the morphological changes (IQR of $\triangle r^{-4}$) was significantly correlated with the changes in RHC examinations, $\triangle$sPAP (R=-0.62, p-value=0.019) and $\triangle$mPAP (R=-0.56, p-value=0.038). Quantifying morphological changes may provide a non-invasive assessment of treatment effects in CTEPH patients, consistent with hemodynamic changes from invasive RHC.

6.1 Introduction

Computed tomography (CT) pulmonary angiography (CTPA) is an important modality for assessing the severity and treatment effects of pulmonary vascular diseases, such as chronic thromboembolic pulmonary hypertension (CTEPH) [34]. Quantifying density changes in pulmonary vessels, by automatically comparing CTPA scans of pre- and post-treatment with image registration, can assess treatment effects of CTEPH [16]. CT measurements of pulmonary vascular morphology could reflect the severity of CTEPH disease [125]. However, invasive right-sided heart catheterization (RHC) serves as the gold standard for assessing disease severity and treatment effects of CTEPH [31], since it directly measures blood pressure at the main pulmonary artery. Quantifying morphological changes by matching pulmonary vessel trees of pre- and post-treatment CT scans may provide a non-invasive assessment of treatment effects.

Vascular tree matching can be treated as a point set registration task, in which the point sets represent the vessel trees. Myronenko et al. [126] proposed a coherent point drift (CPD) method for point sets registration based on a Gaussian mixture model (GMM), and with a regularization term for enforcing the motion coherence and preserving the global topology. The regularization is useful to constrain the global topology, however, its capacity to handle local deformation is low. Ge et al. [127] proposed a method with global-local topology preservation (GLTP), where a local topology term was used for regularization, based on a local linear embedding of the K nearest neighbors of each point. The main idea of local topology preservation is that local neighbors in the original point set should be preserved after transformation. The method works well with dense point sets in computer vision, such as data obtained from the Kinect depth sensor, however, the local topology constraint may induce errors in tree-like structures. This is because leaf points, that belong to different sub-trees, may still be located closely to each other. This method would then consider them as genuine neighbors, therefore over-regularizing the deformations of sub-trees.

In this paper, we propose, therefore, a method that preserves the local tree topology during vascular tree matching, and apply this method to quantify morphological changes of pulmonary vessel trees between pre- and post-treatment. The proposed method consists of three steps: 1) pre-processing for converting the detected vessels into tree structures; 2) vascular tree matching with geodesic paths for local tree topology preservation; and 3) quantification of vascular morphological changes on the basis of Poiseuille's law [128]. The vascular tree matching method was validated with a synthetic data set, and a clinical data set consisting of 14 CTEPH patients, with CT scans and invasive RHC examinations before and after treatment.

Algorithm 1 Constructing vascular trees

1: **procedure** CONSTRUCTVASCULARTREES(g)   ▷ a graph object g
2:      Initial tree T as empty
3:      **for** node_i in g.allNodes() **do**
4:          Initial node nd as empty
5:          nd.ID = node_i.getID()
6:          [nd.px, nd.py, nd.pz] = node_i.getPosition()
7:          **if** node_i has no InEdges **then**
8:              nd.PreID = -1; nd.Radius = node_i.getRadius()
9:          **else**
10:             e = node_i.getInEdge()
11:             nd.PreID = ID of e.getStartNode(); nd.Radius = average radius of e
12:         Attach nd to T
13:     **return** T

6.2   Methods

We aim to align trees T^x and T^y, which can be treated as a point set registration, with reference point set X $= [x_1, ..., x_N]^T$ corresponding to nodes in T^x and template point set Y $= [y_1, ..., y_M]^T$ corresponding to those in T^y, $x_n, y_m \in \mathbb{R}^3$.

6.2.1   Vascular tree construction

For each CT scan, pulmonary vessels were segmented with a graph-cuts method [111]. The skeletons of the pulmonary vessels were extracted with a skeletonization method based on a distance transform [53] ('DtfSkeletonization' of MeVisLab), and the radius was recorded at the corresponding voxels on the skeleton. The skeletons were converted into a directed graph g. In the directed graph, an edge e from a start-node a to end-node b, is called an out-edge of node a and an in-edge of node b. The graph g was processed by stripping cyclic edges, so that each node (except for root node) has only one in-edge, and was converted to a tree T. A node, then, represents a bifurcation point or a leaf point, and an edge represents a branch. For each node, the average radius of the in-edge was calculated by iterating along the voxels on that in-edge and was assigned to the corresponding node. The pseudo-code of the algorithm for constructing vascular trees is given in Algorithm 1.

6.2.2   Vascular tree matching

In GMM-based methods, point sets X and Y can be registered by maximizing the likelihood function and an additional regularization term $R(\Theta)$ where Θ represents the deformation parameters. This framework minimizes the energy function:

$$E = -\log\big(p(X)\big) + R(\Theta). \tag{6.1}$$

X is considered to be distributed from a GMM with centroids Y′ and all Gaussians are equally-weighted with the same isotropic variance σ^2, where Y′ is deformed from Y, Y′ = Y + GW, G is a Gaussian kernel matrix with elements $g_{ij} = exp(-\frac{\|y_i - y_j\|^2}{2\beta^2})$ and W is $M \times D$ weight matrix of the Gaussian kernel. W can be calculated by minimizing Eq. (6.1) when fitting the GMM to X.

The CPD [126] and GLTP [127] use this GMM framework, with different regularization terms. CPD uses a global regularization term $R_{cpd}(W) = \frac{\lambda}{2}Tr(W^T GW)$ and GLTP [127] adapted the regularization term by adding a term for preserving local topology:

$$R(W) = \frac{\lambda}{2}Tr(W^T GW) + \frac{\alpha}{2}Tr\{(Y + GW)^T M(Y + GW)\}, \tag{6.2}$$

where M is an $M \times M$ kernel matrix for preserving local deformation obtained by minimizing local linear cost function embedded with K nearest neighbors [129]. Instead of using K nearest neighbors, we compute a geodesic path with K connected nodes N^g for local topology preservation, which is more suitable for the vascular trees' deformation. $M = (I - H)^T(I - H)$, where H_{ij} is calculated by minimizing: $\Phi(Y) = \sum_i |y_i - \sum_{j \in N_i^g} H_{ij} y_j|^2$ [129]. For each node, a geodesic path is generated by iteratively searching the parent node and child node with a depth-first strategy, the pseudo-code is described in Algorithm 2. E is optimized with the EM algorithm, by minimizing its upper bound is:

$$Q = \sum_{n=1}^{N}\sum_{m=1}^{M} p^{prev}(y'_m|x_n)\frac{\| x_n - y_m - G(m,.)W \|^2}{2\sigma^2} + R(W), \tag{6.3}$$

where $p^{prev}(y'_m|x_n) = p(y'_m)p(x_n|y'_m)/p(x_n)$ is the posterior probability computed with the parameters from the previous step. For optimizing Eq. (6.3), the derivative of Q with respect to W is:

$$\frac{\partial Q}{\partial W} = \frac{1}{\sigma^2}G(diag(P \cdot 1)(Y + GW) - PX) + \lambda GW + \alpha GM(Y + GW), \tag{6.4}$$

in which P is an $M \times N$ matrix with elements $p^{prev}(y'_m|x_n)$. By setting the function 6.4 to zero and right multiplying it by $\sigma^2 G^{-1}$, we have:

$$\{diag(P \cdot 1) + \sigma^2\lambda I + \sigma^2\alpha MG\}W = PX - diag(P \cdot 1)Y + \sigma^2\alpha MY. \tag{6.5}$$

In the M-step of the EM algorithm, W is calculated by solving Eq. (6.5). In the E-step, P is updated with the weight W. After optimizing the energy function, the matching pair C between X and Y can be built by searching point x_n that maximizes the posterior probability, $C(m) = \underset{n}{argmax}\{p(y'_m|x_n)\}$.

6.2.3 Quantitative analysis

The nodes of the vascular trees in pre-treatment CT scans can be compared with those in post-treatment CT scans based on C. As the average radius of a branch is assigned

Algorithm 2 Searching geodesic paths with a deep first strategy

1: **procedure** GEODESICPATHSEARCHING(T, K)
2:    Initial N with the number of nodes in T; $Neighbors$ as an $N \times K$ zeros matrix
3:    **for** $i = 1$ to N **do**
4:       $kfind = 0$
5:       ID $= T(i)$.ID; PreID $= T(i)$.PreID
6:       **while** $kfind < K$ & not (PreID==-1& ID==0) **do**
7:          **if** PreID $\neq$ -1 **then**
8:             [preind, PreID]=findPreID(T,PreID)   ▷ find the ID of pre-Node
9:             $kfind = kfind + 1$; $Neighbors(i, kfind)$=preind
10:         [postind, ID]=findPostID(T, ID)   ▷ randomly pick a post-Node
11:         **if** ID $\neq 0$ **then**
12:            $kfind = kfind + 1$; $Neighbors(i, kfind)$=postind
13:    **return** $Neighbors$ as N^g

---

to its end-node, morphological changes in each branch can be quantified based on C between vascular trees. Poiseuille's law [128] describes the relation between the resistance (ratio between pressure difference and flow rate, $\triangle P/F$) and the radius r in a tube:

$$\triangle P/F = \frac{8\eta L}{\pi r^4},\tag{6.6}$$

where L is the length of the tube and η is the fluid viscosity. Assuming that L and η of a local branch do not change after treatment, its resistance changes can be estimated by the changes in r^{-4} ($\triangle r^{-4}$). Thus, the morphological changes of vascular trees are quantified based on $\triangle r^{-4}$ of matched branches. The median and interquartile range (IQR) of the $\triangle r^{-4}$ are calculated over all branches and are used as global assessments of morphological changes.

6.3 Experiment

The method for constructing pulmonary vascular trees was implemented as a module in MeVisLab 2.7.1, the methods for matching vascular trees and quantifying morphological changes were implemented in Matlab, which is benefiting from the open source tools of CPD [126]. The sourece code and the synthetic data set of vascular tree matching method were made publicly available [1]. The experiments were performed on a local PC, with a 2.67 GHz CPU, 24 GB memory and a 64-bit Windows 7 system.

To evaluate the performance of vascular tree matching, synthetic vascular trees were obtained with a tree editing method [130]. In short, an initial tree T^0 with 3176 nodes was obtained from the left lung of a clinical CT scan and 10 synthetic trees $T^i, i = 1, ..., 10$ were generated by randomly removing $30 * i$ leaf nodes and deformed

---

[1] https://github.com/chushan89/pulmonary-vascular-tree-matching

with Elastix using different non-rigid transformation parameters[131]. To simulate both deletions and additions, the synthetic tree T^5 and T^i were matched with the proposed method (settings: MaxIteration $= 100$, $\beta = 1, \lambda = 3, \text{outlier} = 0.05, \alpha = 100, K = 5$), furthermore, CPD [126] (MaxIteration $= 100$, $\beta = 1, \lambda = 3, \text{outlier} = 0.05$) and GLTP [127] (MaxIteration $= 100$, $\beta = 1, \lambda = 3, \text{outlier} = 0.05, \alpha = 100, K = 5$) were adopted for comparison. The Euclidean distance between nodes in T^5 and T^i were calculated, based on the corresponding point pairs. The average and standard deviation (STD) of the residual distances were used for evaluation.

The quantification of morphological changes was validated with 14 CTEPH patients [16], who were treated with balloon pulmonary angioplasty (BPA), referred to the Tohoku University Hospital. All patients underwent both CTPA scans and RHC examinations, pre- and post-BPA treatment. The invasive RHC examinations, including pulmonary artery pressure (PAP, systolic, diastolic and mean; sPAP, dPAP and mPAP) and pulmonary vascular resistance (PVR), are examined at the main pulmonary artery. The RHC parameters changes ($\triangle$PAP and $\triangle$PVR) were used as reference measurements for assessing treatment effects. The morphological changes in vascular trees were quantified with the proposed method. The relation between the quantifications of morphological changes and hemodynamic changes ($\triangle$sPAP, $\triangle$dPAP, $\triangle$mPAP, $\triangle$PVR) were validated with Pearson's correlation.

6.4 Results

The proposed method obtained an average residual distance of 3.09 ± 1.28 mm, while CPD and GLTP obtained an average distance of 4.32 ± 1.89 mm and 3.92 ± 1.59 mm, respectively. In comparison with CPD and GLTP, the proposed method achieved a substantial improvement, as shown in Fig. 6.1. The 3D visualization of vascular tree matching and evaluations based on the correct correspondences can be found in the supplement.

The relation between morphological changes in pulmonary vascular trees and changes in RHC measurements were investigated with 14 CTEPH patients. The IQR of $\triangle r^{-4}$ significantly correlated with $\triangle$sPAP (R=-0.62, p-value=0.019) and $\triangle$mPAP (R=-0.56, p-value=0.038), but the median of $\triangle r^{-4}$ did not have a significant correlation with hemodynamic changes. Quantitative analysis of vascular morphological changes in two selected patients are shown in Fig. 6.2. Pearson's correlation results are given in Table 6.1, and scatter plots are shown in Fig. 6.3.

6.5 Discussion and Conclusion

We present a method for quantifying morphological changes in pulmonary vascular trees, pre- and post-treatment, using vascular tree matching. The vascular tree matching method with geodesic paths for local topology preservation showed a
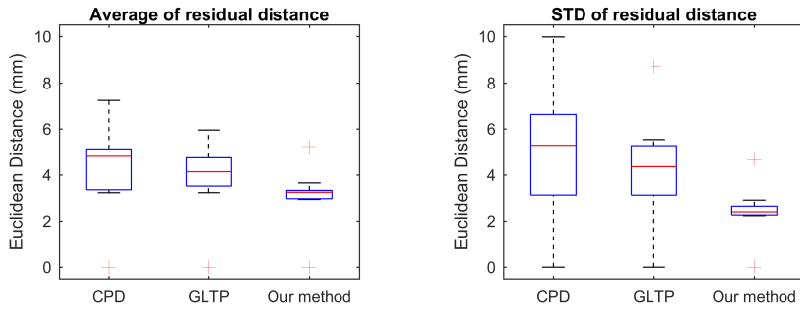
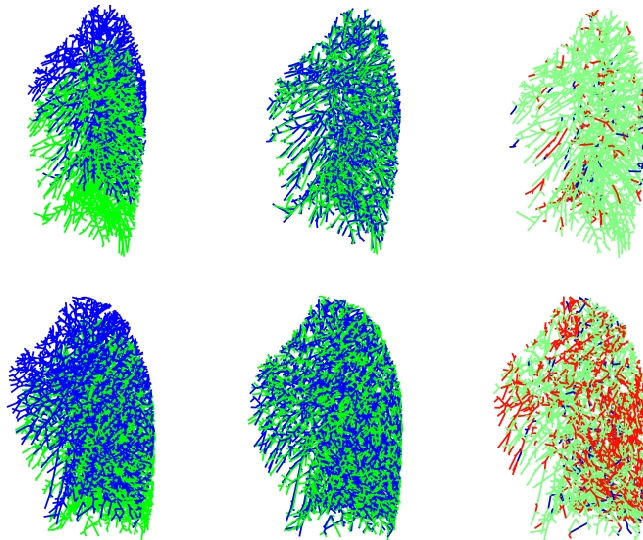Figure 6.1: Evaluation for vascular tree matching, average and STD of distance.

Figure 6.2: Morphological changes of pulmonary vessels for two patients, patient A in the first row and B in the second row. Left column, initial position of vascular trees; middle column, matched vascular trees; right column, color-coded vascular trees, based on morphological changes (red: a large increase in r^{-4}; blue: a large decrease; green small changes).

better performance, in comparison with methods of CPD and GLTP. The IQR of $\triangle r^{-4}$, calculated based on Poiseuille's law, had a significant negative correlation with the $\triangle sPAP$ and $\triangle mPAP$, which implies that a higher variation in $\triangle r^{-4}$ corresponds to a bigger treatment effect of decreasing pulmonary arterial pressure. This finding is consistent with a previous observation that a higher variation in density changes was related to bigger drop in pressure. In future work, we will focus on a more detailed
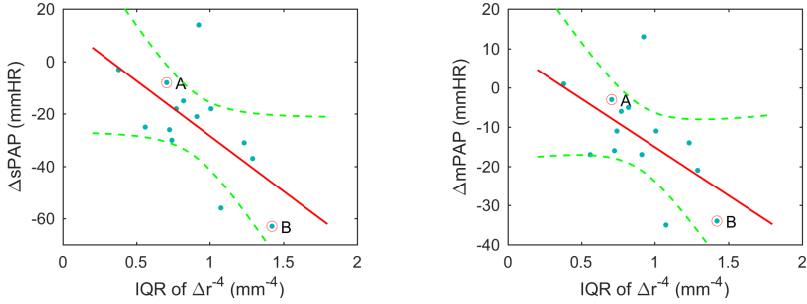
Figure 6.3: Scatter plot for IQR of $\triangle r^{-4}$ against $\triangle$sPAP and $\triangle$mPAP (A and B are corresponding to patient A and B in Fig. 6.2).

Table 6.1: Pearson's correlation R (p-value) between morphological changes and hemodynamic changes.

	$\triangle$sPAP	$\triangle$dPAP	$\triangle$mPAP	$\triangle$PVR
median of $\triangle r^{-4}$	0.19 (0.506)	0.04 (0.901)	0.16 (0.576)	0.07 (0.815)
IQR of $\triangle r^{-4}$	-0.62 (0.019)	-0.46 (0.097)	-0.56 (0.038)	-0.47 (0.088)

validation of the vascular tree matching with manually annotated corresponding point pairs. By applying methods of artery-vein separation, the quantification of morphological changes may become more specific for CTEPH, since that is an arterial disease.

In conclusion, morphological changes can reflect hemodynamic changes, and quantifying morphological changes by matching vascular trees can provide a non-invasive assessment of treatment effects in CTEPH patients.

Supplementary

In the experiment of synthetic vascular trees, the matching pairs were validated based on the nodes ID (described in Algorithm 1). The correct matches are considered as true positives, the incorrect ones are corresponding to false positives and the missed ones are false negatives. The number of true positives, false positives and false negatives were counted and expressed as TP, FP and FN, respectively. The evaluation metrics F1, precision and recall were calculated based on the TP, FP and FN. The proposed method obtained an average F1 of 0.80 ± 0.09, comparing to 0.74 ± 0.11 for CPD and 0.76 ± 0.10 for GLTP, as illustrated in Fig. 6.5, where the proposed method obtained a better F1 score, in comparison with methods CPD and GLTP.

In the clinical experiment, Pearson correlation analysis of the methods CPD and GLTP were calculated, where quantifications in vascular morphological changes

Table 6.2: Pearson's correlation R (p-value) between morphological changes and hemodynamic changes, for CPD and GLTP.

	$\triangle$sPAP	$\triangle$dPAP	$\triangle$mPAP	$\triangle$PVR
m of $\triangle r^{-4}$ #	-0.08 (0.786)	-0.30 (0.291)	-0.18 (0.54)	-0.20 (0.498)
IQR of $\triangle r^{-4}$ #	-0.66 (0.011)	-0.54 (0.046)	-0.61 (0.020)	-0.54 (0.047)
m of $\triangle r^{-4}$ *	-0.07 (0.803)	-0.23 (0.429)	-0.11 (0.719)	-0.16 (0.586)
IQR of $\triangle r^{-4}$ *	-0.68 (0.007)	-0.55 (0.041)	-0.64 (0.013)	-0.53 (0.049)

results of method CPD; * results of method GLTP; m, median, IQR interquartile range;

were calculated based on their corresponding mapping pairs. The non-invasive measurements calculated with CPD or GLTP were also significantly correlated with the invasive RHC changes, as demonstrated in Table 6.2. The correlations between $\triangle$sPAP, $\triangle$mPAP and IQR of $\triangle r^{-4}$ of CPD or GLTP were significant, which demonstrated that these non-invasive measurements based on Poiseuille's law were significantly correlated with the invasive RHC parameters. Estimating pressure changes based on Poiseuille's law is promising to calculate non-invasive measurements. As there are only 14 patients involved in this study, the Pearson correlations of the CPD, GLTP and proposed method were considered in similar level, although the performance of CPD and GLTP was a bit better.

$$F1 = \frac{2TP}{2TP + FN + FP} \tag{6.7}$$

$$precision = \frac{TP}{TP + FP} \tag{6.8}$$

$$recall = \frac{TP}{TP + FN} \tag{6.9}$$

(a) CPD T^5 T^1 (b) GLPT T^5 T^1 (c) Our method T^5 T^1

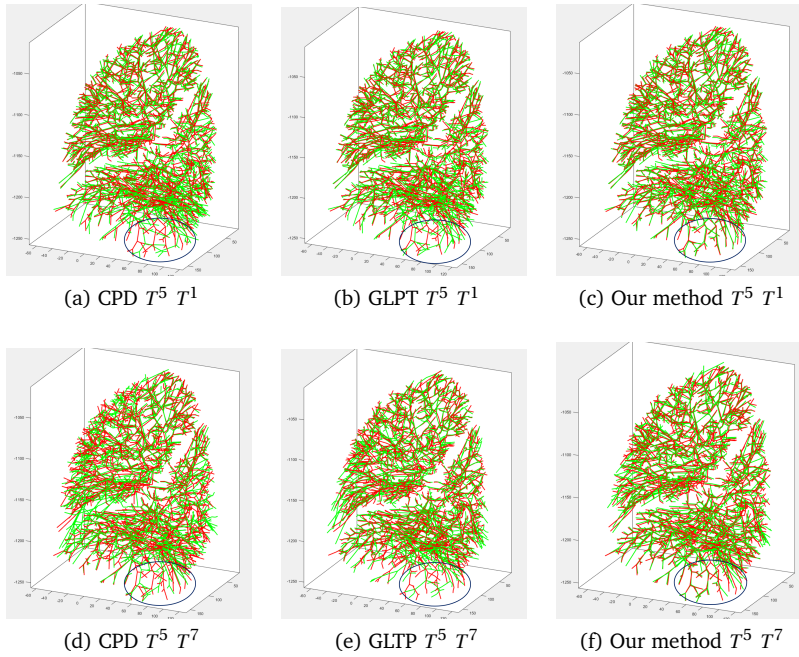(d) CPD T^5 T^7 (e) GLTP T^5 T^7 (f) Our method T^5 T^7

Figure 6.4: 3D visualization of vascular tree matching for two cases, first row is for a good case: matching T^5 and T^1, CPD 5.26 ± 6.85 mm, GLTP 4.01 ± 4.13 mm and our method 3.17 ± 2.64 mm; second row is for a bad case: matching T^5 and T^7, CPD 7.25 ± 9.98 mm, GLTP 5.96 ± 8.74 mm and our method 2.97 ± 2.41 mm.
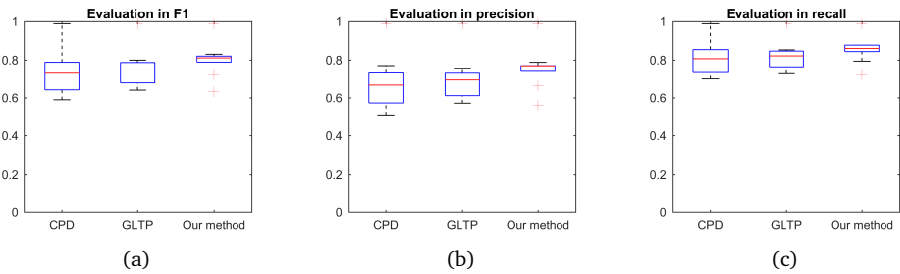

(a)   (b)   (c)

Figure 6.5: Evaluations with the number of correct correspodences, (a) F1 score: 0.80 ± 0.09 for the proposed method, 0.74 ± 0.11 for CPD and 0.76 ± 0.10 for GLTP; (b)precision: 0.76 ± 0.11 for the proposed method, 0.68 ± 0.13 for CPD and 0.70 ± 0.12 for GLTP; (c)recall: 0.85 ± 0.07 for the proposed methond, 0.81 ± 0.08 for CPD and 0.82 ± 0.07 for GLTP.

7

Summary and Future Work

High-resolution CT is an important modality to non-invasively diagnose pulmonary diseases and assess treatment effects. In this thesis, we developed automatic methods to quantify pulmonary vasculature and assess treatment effects of CTEPH disease, based on high-resolution CT images. Within an HRCT scan, pulmonary vessels are automatically extracted with a graph-cuts based method, and subsequently the extracted pulmonary vessels are objectively quantified with quantification methods. In this chapter, we summarize the previous chapters and discuss interesting directions of future research.

7.1   Summary

In this thesis, we first provided a general introduction in Chapter 1 about pulmonary anatomy, diseases, clinical assessments, and chest CT scans. A lung vessel segmentation method was proposed in Chapter 2, as accurately extracting lung vessels is an essential step for pulmonary vessel analysis. An automatic method for pulmonary vessel quantification was developed in Chapter 3, where two imaging biomarkers α and β were proposed for quantifying the vascular morphology. In Chapter 4, the relation between these imaging biomarkers and pulmonary function were investigated in a selected SSc patient group, who had reductions in gas transfer but did not have fibrosis. The densitometry changes in pulmonary vasculature and parenchyma were studied by comparing CTPA scans before and after treatment for CTEPH patients treated with BPA, in Chapter 5. A vascular tree matching method was proposed for matching pulmonary vasculature trees, for quantifying changes in vascular morphology for CTEPH patients in Chapter 6.

    Chapter 2 For lung CT image analysis, lung vessel segmentation is an important processing step. Filters that are based on analyzing the eigenvalues of the Hessian matrix are popular for enhancing pulmonary vessels. However, due to their low

response at vessel bifurcations and vessel boundaries, extracting lung vessels by thresholding the vesselness response is not sufficiently accurate. The graph-cuts method could provide more accurate segmentations, as it considers neighborhood information when determining the label of a voxel. We propose a new graph-cuts based method, where the appearance (CT intensity) and shape (vesselness) are combined into one cost function. As the number of voxels in high-resolution CT image is large, building the corresponding graph structure requires a lot of memory and is time consuming. Therefore, an efficient and low memory cost strategy is proposed for constructing the graph structure. Then, the lung vessels are segmented by minimizing the energy cost function with the graph-cuts optimization framework, where the energy cost function is calculated based on the constructed graph. The proposed method is trained and validated by an in-house data set, and independently evaluated with a public data set of the VESSEL12 challenge. According to the evaluation results, the proposed method is accurate, and obtains a competitive performance in VESSEL12.

Chapter 3 Pulmonary vascular remodeling is a significant pathological feature of various pulmonary diseases. In this chapter, we propose an automatic method for quantifying pulmonary vascular morphology in CT images. There are two processing steps in the proposed method: pulmonary vessel extraction and vessel quantification. The vessels are extracted with an improved graph-cuts based method, which incorporates the appearance (CT intensity) and shape features (vesselness from a Hessian-based filter), and considers distance to airways into the cost function. For quantifying the extracted pulmonary vessels, a radius histogram is generated by counting the occurrence of vessel radii, calculated from a distance transform based method. Subsequently, two biomarkers, slope α and intercept β, are calculated by linear regression on the radius histogram. A public data set of VESSEL12, a data set of 3D printed vessel phantom and a clinical data set of scleroderma patients are involved for evaluating and validating the proposed method. Based on the results, the proposed method is highly accurate, by validating with a public data set and a 3D printed vessel phantom data set. The correlation between imaging biomarkers and diffusion capacity in clinical data confirms an association between lung structure and function.

Chapter 4 For systemic sclerosis (SSc), gas transfer is known to be affected by fibrotic changes in the pulmonary parenchyma. However, SSc patients without detectable fibrosis can still have impaired gas exchange. We investigate the pulmonary vascular changes of a patient group in SSc without fibrosis, where remodeling of pulmonary vasculature may partly explain the reduction of gas transfer. Seventy-seven SSc patients were selected who underwent pulmonary function tests and CT scanning, that showed no visible fibrosis. The pulmonary vascular morphology was quantified into two imaging biomarkers, with a primary method to the one in Chapter 3. The association between imaging biomarkers and gas transfer (DLCOc %predicted)

was investigated, which showed a moderate but significant correlation between pulmonary vascular morphology and gas transfer. In conclusion, in SSc patients without pulmonary fibrosis, impaired gas exchange is associated with alterations in pulmonary vascular morphology.

Chapter 5 Patients with inoperable CTPEH, BPA can be an alternative treatment to improve the clinical status and hemodynamics. The invasive right heart catheterization serves as gold standard in evaluating the severity and assessing the treatment effects of CTEPH. In this chapter, we proposed an objective and automatic method to non-invasively assess treatment effects, by comparatively analyzing CTPA of pre- and post-BPA treatment. A cohort of 14 patients in CTEPH, who underwent both CTPA and RHC, before and after BPA, are involved in this study. The densitometric changes in pulmonary vessels and parenchyma are automatically quantified, where the vessels and parenchyma are separated by the graph-cuts based method. The association between perfusion changes and hemodynamic changes are investigated, where the densitometric parameter are significantly correlated with RHC measurements. Based on the CTPA, quantifying the perfusion changes provides non-invasive measures that reflect hemodynamic changes.

In **Chapter 6**, we propose a pulmonary vessel tree matching method, which enables the quantification of pulmonary morphological changes, longitudinally. In the proposed method, first, the pulmonary vessels are simplified and constructed into a directed graph, a vascular tree is structured by stripping cyclic edges, which makes the quantification at the branch level possible. Then, a tree matching method is proposed, by considering a geodesic path for local topology preservation. In the last processing step, the resistance changes of each branch are analyzed, based on the Poiseulle's law. Two datasets, a synthetic data set and a clinical data set, are used to validate the accuracy and clinical relevance of the proposed method, respectively. In the results, the proposed vessel tree matching method performs better than two exist methods, and the resistance changes of pulmonary vessels is correlated with hemodynamic changes.

7.2 Future Work

The work presented in this thesis was aimed at developing methods to quantify pulmonary vessels, based on the CT images. The entire pulmonary vascular trees, both arteries and veins, are automatically extracted and subsequently investigated. It is known, however, that pulmonary diseases may affect arteries or veins in a different way. Investigating the pulmonary arteries and veins separately will be of great help in evaluating pulmonary diseases. Separating and classifying pulmonary arteries and veins is, however, a challenging project. With the classification power of deep learning, it would be possible to develop deep-learning based methods to separate arteries

and veins. By preparing a large amount of manually annotated data for training, developing deep learning based method for separating pulmonary arteries and veins would be an interesting topic for future. If the pulmonary arteries and veins are successfully separated, there will be multiple interesting clinical applications, such as separately quantifying morphological changes of pulmonary arteries or veins of patients in SSc, quantifying the A/V perfusion changes of BPA treatment for patients in CTEPH, etc.

For the studies on SSc (Chapter 3 and 4), only baseline CT images of patients were investigated. Exploring vascular morphology longitudinally will also be an interesting future topic. According to the protocol of the biobank of the Leiden Combined Care in SSc (CISS), patients are scanned at both full-inspiration and full-expiration level. For patients with SSc, the elasticity of lungs can be influenced significantly by pulmonary fibrosis. Developing methods, by mapping the inspired and expired CT scans, may provide a way to investigate the elasticity of pulmonary parenchyma, which may help to evaluate the severity of SSc-related pulmonary diseases.

7.3   General conclusions

In conclusion, this thesis proposes automatic methods for quantifying pulmonary vessels. An accurate and well-validated lung vessel segmentation method is developed and open source online. Investigating changes in pulmonary vascular morphology may be helpful in understanding the pathophysiology of the SSc patients whose gas transfer deteriorates in the course of their disease without detectable pulmonary fibrosis. Assessing the perfusion changes in pulmonary vasculature using automatic comparison of CTPAs acquired before and after treatment could reflect the hemodynamic changes. Quantifying pulmonary vascular changes in morphology or densitometry may provide non-invasively diagnosis of pulmonary diseases and assessments of treatment effects, based on CT.

Samenvatting en toekomstig werk

Hoge-resolutie CT (HRCT) is een belangrijke modaliteit om longziekten non-invasief te diagnosticeren en behandeleffecten te beoordelen. In dit proefschrift hebben we automatische methoden ontwikkeld om de pulmonale vasculatuur te kwantificeren en effecten van de behandeling van CTEPH te beoordelen, gebaseerd op HRCT. In een HRCT scan worden longvaten automatisch geëxtraheerd met een methode, die gebaseerd is op 'graph-cuts' (graaf-sneden), en vervolgens worden de geëxtraheerde longvaten objectief gemeten met kwantitatieve methoden. In dit hoofdstuk, vatten we de eerdere hoofdstukken samen en bediscussiëren interessante richtingen voor vervolgonderzoek.

Samenvatting

In dit proefschrift gaven we in Hoofdstuk 1 eerst een algemene inleiding over de longanatomie, longziekten, klinische beoordelingen en thorax CT scans. Een pulmonale vaatsegmentatie-methode werd gepresenteerd in Hoofdstuk 2, aangezien een nauwkeurige extractie van longvaten een essentiële stap is in de pulmonale vaatanalyse. Een automatische methode om longvaten te kwantificeren was ontwikkeld in Hoofdstuk 3, waar twee beeld-biomarkers α en β waren geïntroduceerd voor de kwantificatie van de vasculaire morfologie. In Hoofdstuk 4 was de relatie onderzocht tussen deze beeld-biomarkers en longfunctie in een groep van geselecteerde SSc patiënten, die een verminderde gasuitwisseling hadden maar geen fibrose lieten zien. De densitometrische veranderingen in de pulmonale vasculatuur en parenchym waren onderzocht in CTEPH patiënten door CTPA scans te vergelijken tussen voor en na behandeling met BPA (Hoofdstuk 5). In Hoofdstuk 6 was een methode voorgesteld om pulmonale vaatbomen op elkaar te passen, zodat veranderingen in de vasculaire morfologie lokaal kan worden bepaald in CTEPH patiënten.

Hoofdstuk 2 Pulmonale vaatsegmentatie is een belangrijke verwerkingsstap voor long CT beeldanalyse. Filters, die gebaseerd zijn op het analyseren van de eigenwaarden van de Hessiaan, zijn populair bij het accentueren van de longvaten. Door hun lage respons op bifurcaties en vaatranden, is het drempelen van de vaatrespons niet nauwkeurig genoeg om de longvaten te extraheren. De 'graph-cuts' methode zou een nauwkeuriger segmentatie kunnen geven, omdat deze informatie over de omgeving

meeneemt bij het bepalen van het label van een voxel. We presenteren een nieuwe methode gebaseerd op 'graph-cuts', waarin de verschijning (CT intensiteit) en vorm ('vesselness', vaatachtigheid) gecombineerd worden in één kostenfunctie. Omdat het aantal voxels in HRCT beelden groot is, vergt het bouwen van een graafstructuur erg veel geheugen en rekentijd. Daarom is een efficiënte strategie met een laag geheugenverbruik voorgesteld om de graafstructuur te construeren. Daarna worden de longvaten gesegmenteerd door de energie-kostenfunctie te minimaliseren met het raamwerk van de 'graph-cuts' optimalisatie, waar de energie-kostenfunctie is berekend uit de geconstrueerde graaf. De voorgestelde methode is getraind en gevalideerd met een in-huis dataset en onafhankelijke geëvalueerd met een publieke dataset van de 'VESSEL12 challenge'. Uit de evaluatieresultaten blijkt de voorgestelde methode nauwkeurig en behaalde het een competitief resultaat in VESSEL12.

Hoofdstuk 3 Vaat-remodelering in de longen is een belangrijk pathologisch kenmerk van verschillende longziekten. In dit hoofdstuk introduceren we een automatische methode om de morfologie van de longvaten in CT-beelden te kwantificeren. De vaten worden geëxtraheerd met een verbeterde 'graph-cuts' methode, die de verschijning (CT intensiteit) en vormkenmerken ('vesselness' uit het Hessiaan-filter) maar ook de afstand tot de luchtwegen in de kostenfunctie opneemt. Voor het kwantificeren van de gedetecteerde longvaten is een radius-histogram gemaakt door het aantal keren te tellen dat een bepaalde vaatradius voorkomt, berekend uit een afstandstransformatie-methode. Vervolgens worden twee biomarkers, helling α en intercept β, berekend door middel van lineaire regressie op het radius-histogram. De publieke dataset van VESSEL12, een dataset van een 3D-geprint vaatfantoom en een klinische dataset van sclerodermiepatiënten waren gebruikt bij de evaluatie en validatie van de voorgestelde methode. Uit de resultaten van de validatie met de publieke dataset en het vaatfantoom blijkt dat de voorgestelde methode zeer nauwkeurig is. De correlatie tussen de beeld-biomarkers en diffusiecapaciteit in de klinische dataset bevestigt de associatie tussen longstructuur en functie.

Hoofdstuk 4 Van systemische sclerose (SSc) is bekend dat de gasuitwisseling is aangetast door fibrotische veranderingen in het longparenchym. SSc-patiënten zonder detecteerbare fibrose kunnen echter toch een verminderde gasuitwisseling hebben. We onderzochten de veranderingen in de longvaten in een patiëntgroep zonder fibrose, om uit te zoeken of remodelering van de pulmonale vasculatuur de vermindering in gastuitwisseling deels zou kunnen verklaren. Zevenzeventig SSc-patiënten waren geselecteerd, die longfunctietests hadden ondergaan samen met CT scans, waarin geen zichtbare fibrose aanwezig was. De morfologie van de longvaten was gekwantificeerd met de twee beeld-biomarkers, zoals beschreven in Hoofdstuk 3. De associatie tussen de beeld-biomarkers en gasuitwisseling (DLCOc %voorspeld) was onderzocht, hetgeen een bescheiden maar significante correlatie tussen de vasculaire

morfologie en gasuitwisseling liet zien. In SSc-patiënten zonder longfibrose is de verminderde gasuitwisseling dus geassocieerd met veranderingen in de morfologie van de longvaten.

Hoofdstuk 5 Bij patiënten met inoperabele CTEPH kan BPA een alternatieve behandeling zijn om de klinische toestand en hemodynamica te verbeteren. De invasieve rechts hartkatheterisatie (RHC) dient als gouden standaard bij het evalueren van de ernst van CTEPH en het beoordelen van het behandeleffect van BPA. In dit hoofdstuk presenteren we een objectieve en automatische methode om behandeleffecten niet-invasief te beoordelen door CTPA scans van pre- en post-BPA vergelijkenderwijs te analyseren. Een cohort van 14 CTEPH patiënten was betrokken in deze studie, die zowel CTPA als RHC hadden ondergaan, voor en na BPA. De densitometrische veranderingen in de longvaten en parenchym waren automatisch gekwantificeerd, waar de vaten en parenchym gescheiden waren door de 'graph-cuts' methode. De associatie tussen perfusieveranderingen en hemodynamische veranderingen was onderzocht, waarbij de densitometrische parameters significant gecorreleerd waren met de RHC metingen. Het kwantificeren van perfusieveranderingen gebaseerd op CTPA, biedt daarom niet-invasieve metingen, die hemodynamische veranderingen weerspiegelen.

In **Hoofdstuk 6** stellen we een methode voor om longvaatbomen op elkaar te passen, die het mogelijk maakt om longitudinaal morfologische veranderingen in de long te kwantificeren. In de voorgestelde methode worden de gedetecteerde longvaten eerst versimpeld en geconstrueerd tot een gerichte graaf, en een vaatboom wordt gestructureerd door het verwijderen van cykels, zodat de kwantificatie op tak-niveau mogelijk wordt. Vervolgens is een methode voorgesteld om boomstructuren op elkaar te passen, door het geodetische pad te beschouwen, zodat de lokale topologie wordt behouden. In de laatste verwerkingsstap worden de veranderingen in weerstand in elke tak geanalyseerd op grond van de wet van Poiseulle. Twee datasets, een synthetische en een klinische dataset, waren gebruikt om respectievelijk de nauwkeurigheid en klinische relevantie van de voorgestelde methode te valideren. Uit de resultaten bleek dat de voorgestelde methode om vaatbomen op elkaar te passen het beter deed dan twee bestaande methoden, en de veranderingen in weerstand in de longvaten gecorreleerd was met hemodynamische veranderingen.

Vervolgonderzoek

Het werk dat in dit proefschrift is gepresenteerd, was gericht op het ontwikkelen van methoden om longvaten te kwantificeren, op grond van CT-opnames. De volledige longvaatboom, d.w.z. arteriën en venen tezamen, zijn automatisch geëxtraheerd en vervolgens onderzocht. Het is echter bekend, dat longziekten de arteriën en venen op een verschillende manier kunnen aantasten. Het apart onderzoeken van

arteriën en venen zal daarom helpen om longziekten te beoordelen. Het scheiden en classificeren van arteriën en venen is echter een uitdagend project. Met het vermogen van deep learning om te classificeren, zou het mogelijk kunnen zijn om methoden te ontwikkelen met deep-learning om arteriën en venen te scheiden. Door het creëren van grote hoeveelheden van handmatig getekende long-arteriën en -vaten zou het ontwikkelen van deep-learning-gebaseerde methoden om arteriën en venen te scheiden een interessante onderwerp zijn in de toekomst. Als de long-arteriën en -venen succesvol gescheiden kunnen worden, zullen er een grote hoeveelheid klinische toepassingen zijn, zoals het apart kwantificeren van de morfologische veranderingen in long-arteriën en venen van SSc patiënten, het kwantificeren van A/V perfusieveranderingen door BPA behandeling van patiënten met CTEPH, etc.

In de onderzoeken naar SSc (Hoofdstukken 3 en 4) zijn alleen de baseline CT-opnames van patiënten onderzocht. Longitudinaal onderzoek naar veranderingen in de vasculaire morfologie zal ook een interessant toekomstig onderwerp zijn. Volgens het protocol van het zorgpad systemische sclerose van het LUMC worden patiënten gescand in zowel vol-inspiratie als vol-expiratie. In SSc patiënten kan de elasticiteit van de longen significant beïnvloed worden door longfibrose. Het ontwikkelen van methoden door de inspiratie en expiratie scans op elkaar te passen, kunnen een manier verschaffen om de elasticiteit van het longparenchym te onderzoeken, wat kan helpen bij het evalueren van de ernst van de SSc-gerelateerde longziekten.

In de studies over BPA behandeling van CTEPH-patiënten (Hoofdstukken 5 en 6), zijn de globale veranderingen in perfusie en morfologie van de longvaten onderzocht. Omdat BPA behandeling een lokale behandeling is van een pulmonale arterieel segment met een trombus, zou een lokale kwantificatie van het corresponderende vaatsegment of omliggende parenchym meer specifieke informatie kunnen leveren. Het bestuderen van de veranderingen in de behandelde en niet-behandelde longarteriën zal meer inzicht geven in de lokale behandeleffecten van BPA. Hoewel BPA behandeling gericht is op longarteriën, zal de densiteit in de longvenen ook veranderen met de verbeterde perfusie van contrast. Daarom is het begrijpen van perfusieveranderingen in longvenen een interessante uitdaging.

Algemene conclusies

Samengevat stelt dit proefschrift automatische methoden voor om longvaten te kwantificeren. Een nauwkeurige en goed-gevalideerde pulmonale vaatsegmentatie-methode is ontwikkeld en als open-source online beschikbaar gesteld. Onderzoek naar de veranderingen in de morfologie van longvaten kan behulpzaam zijn bij het begrijpen van de pathofysiologie van SSc waarin gasuitwisseling achteruitgaat gedurende het verloop van de ziekte, zonder detecteerbare longfibrose. Het beoordelen van perfusieveranderingen in pulmonale vasculatuur door middel van automatische

vergelijking van CTPAs, verkregen voor en na behandeling, kunnen hemodynamische veranderingen weerspiegelen. Het kwantificeren van veranderingen in de morfologie en densitometrie in longvaten kan een niet-invasieve beoordeling van longziekten en behandeleffecten bieden, gebaseerd op CT.

Bibliography

[1] R. L. R. L. Drake, W. Vogl, A. W. M. Mitchell, and H. Gray. *Gray's anatomy for students*, page 1161.

[2] S. Standring. *Gray's Anatomy : the Anatomical Basis of Clinical Practice.* Elsevier Health Sciences UK, 2008, page 1574.

[3] J. Tu, K. Inthavong, and G. Ahmadi. *Computational Fluid and Particle Dynamics in the Human Respiratory System*. Biological and Medical Physics, Biomedical Engineering. Dordrecht: Springer Netherlands, 2013. URL: http://link.springer.com/10.1007/978-94-007-4488-2.

[4] G. Pocock and C. D. Richards. *Human physiology : the basis of medicine*. Oxford University Press, 2006, page 638.

[5] B. M. Koeppen and B. A. Stanton. *Berne & Levy physiology*, page 829.

[6] M. G. Levitzky. *Pulmonary physiology*. Volume 7. McGraw-Hill Medical New York, 2007.

[7] A. T. Society. "Standards for the diagnosis and care of patients with chronic obstructive pulmonary disease (COPD) and asthma." In: *Am Rev Respir Dis* 136 (1987), pages 225–244. URL: https://ci.nii.ac.jp/naid/10005111964/.

[8] G. S. Vijeyaratnam and B. Corrin. "Pulmonary alveolar proteinosis developing from desquamative interstitial pneumonia in long term toxicity studies of iprindole in the rat". In: *Virchows Archiv A Pathologische Anatomie* 358.1 (1973), pages 1–10. URL: http://link.springer.com/10.1007/BF00555550.

[9] M. Hinchcliff and J. Varga. "Systemic sclerosis/scleroderma: a treatable multisystem disease". In: *Am Fam Physician* 78.8 (2008), pages 961–968.

[10] S. Cappelli, S. B. Randone, G. Camiciottoli, et al. "Interstitial lung disease in systemic sclerosis: where do we stand?" In: *European Respiratory Review* 24.137 (2015), pages 411–419.

[11] N. S. Goh, S. R. Desai, S. Veeraraghavan, et al. "Interstitial lung disease in systemic sclerosis: a simple staging system". In: *American journal of respiratory and critical care medicine* 177.11 (2008), pages 1248–1254.

[12] S. Matsuoka, G. R. Washko, T. Yamashiro, et al. "Pulmonary Hypertension and Computed Tomography Measurement of Small Pulmonary Vessels in Severe Emphysema". In: *American Journal of Respiratory and Critical Care Medicine* 181.3 (Feb. 2010), pages 218–225.

[13] D. Mukerjee, D. St. George, C. Knight, et al. "Echocardiography and pulmonary function as screening tests for pulmonary arterial hypertension in systemic sclerosis". In: *Rheumatology* 43.4 (2004), pages 461–466.

[14] M. Delcroix, A. V. Noordegraaf, E. Fadel, et al. "Vascular and right ventricular remodelling in chronic thromboembolic pulmonary hypertension". In: *European Respiratory Journal* 41.1 (Jan. 2013), pages 224–232.

[15] M. M. Hoeper, E. Mayer, G. Simonneau, and L. J. Rubin. "Chronic thromboembolic pulmonary hypertension". In: *Circulation* 113.16 (2006), pages 2011–2020.

[16] Z. Zhai, H. Ota, M. Staring, et al. "Treatment Effect of Balloon Pulmonary Angioplasty in Chronic Thromboembolic Pulmonary Hypertension Quantified by Automatic Comparative Imaging in Computed Tomography Pulmonary Angiography". In: *Investigative radiology* 53.5 (2018), pages 286–292.

[17] M. Riedel, V. Stanek, J. Widimsky, and I. Prerovsky. "Longterm follow-up of patients with pulmonary thromboembolism: late prognosis and evolution of hemodynamic and respiratory data". In: *Chest* 81.2 (1982), pages 151–158.

[18] J. Lewczuk, P. Piszko, J. Jagas, et al. "Prognostic factors in medically treated patients with chronic pulmonary embolism". In: *Chest* 119.3 (2001), pages 818–823.

[19] H. Takagi, H. Ota, K. Sugimura, et al. "Dual-energy CT to estimate clinical severity of chronic thromboembolic pulmonary hypertension: Comparison with invasive right heart catheterization". In: *European journal of radiology* 85.9 (2016), pages 1574–1580.

[20] E. Mayer, D. Jenkins, J. Lindner, et al. "Surgical management and outcome of patients with chronic thromboembolic pulmonary hypertension: results from an international prospective registry". In: *The Journal of thoracic and cardiovascular surgery* 141.3 (2011), pages 702–710.

[21] K. Sugimura, Y. Fukumoto, K. Satoh, et al. "Percutaneous Transluminal Pulmonary Angioplasty Markedly Improves Pulmonary Hemodynamics and Long-Term Prognosis in Patients With Chronic Thromboembolic Pulmonary Hypertension". In: *Circulation Journal* 76.2 (2012), pages 485–488.

[22] M. M. Madani, W. R. Auger, V. Pretorius, et al. "Pulmonary endarterectomy: recent changes in a single institution's experience of more than 2,700 patients". In: *The Annals of thoracic surgery* 94.1 (2012), pages 97–103.

[23] H. Mizoguchi, A. Ogawa, M. Munemasa, et al. "Refined balloon pulmonary angioplasty for inoperable patients with chronic thromboembolic pulmonary hypertension". In: *Circulation: Cardiovascular Interventions* 5.6 (2012), pages 748–755.

[24] D. Fontein, M Klinten Grand, J. W. Nortier, et al. "Dynamic prediction in breast cancer: proving feasibility in clinical practice using the TEAM trial". In: *Annals of Oncology* 26.6 (2015), pages 1254–1262.

[25] M. K. Ninaber, J. Stolk, J. Smit, et al. "Lung structure and function relation in systemic sclerosis: Application of lung densitometry". In: *European Journal of Radiology* 84.5 (May 2015), pages 975–979.

[26] D. Y. Sue, A. Oren, J. E. Hansen, and K. Wasserman. "Diffusing capacity for carbon monoxide as a predictor of gas exchange during exercise". In: *New England Journal of Medicine* 316.21 (1987), pages 1301–1306.

[27] L. L. Pérez. "Office spirometry". In: *Osteopathic Family Physician* 5.2 (2013), pages 65 – 69. URL: `http://www.sciencedirect.com/science/article/pii/S1877573X12001554`.

[28] P. Callan and A. L. Clark. "Right heart catheterisation: indications and interpretation". In: *Heart* 102.2 (2016), pages 147–157.

[29] N. Galiè, M. Humbert, J.-L. Vachiery, et al. "2015 ESC/ERS Guidelines for the diagnosis and treatment of pulmonary hypertension". In: *European Heart Journal* 37.1 (Jan. 2016), pages 67–119.

[30] S. Rosenkranz and I. R. Preston. "Right heart catheterisation: best practice and pitfalls in pulmonary hypertension". In: *European Respiratory Review* 24.138 (2015), pages 642–652.

[31] N. H. Kim, M. Delcroix, D. P. Jenkins, et al. "Chronic thromboembolic pulmonary hypertension". In: *Journal of the American College of Cardiology* 62.25 Supplement (2013), pages D92–D99.

[32] I. M. Lang and M. Madani. "Update on chronic thromboembolic pulmonary hypertension". In: *Circulation* 130.6 (2014), pages 508–518.

[33] E. A. Kazerooni, F. J. Martinez, A. Flint, et al. "Thin-section CT obtained at 10-mm increments versus limited three-level thin-section CT for idiopathic pulmonary fibrosis: correlation with pathologic scoring." In: *AJR. American journal of roentgenology* 169.4 (1997), pages 977–983.

[34] M. Liu, Z. Ma, X. Guo, et al. "Computed tomographic pulmonary angiography in the assessment of severity of chronic thromboembolic pulmonary hypertension and right ventricular dysfunction". In: *European journal of radiology* 80.3 (2011), e462–e469.

[35] W. R. Webb, W. E. Brant, and N. M. Major. *Fundamentals of body CT*. Elsevier Health Sciences, 2014.

[36] R. K. Kaza, J. F. Platt, R. H. Cohan, et al. "Dual-energy CT with single-and dual-source scanners: current applications in evaluating the genitourinary tract". In: *Radiographics* 32.2 (2012), pages 353–369.

[37] G. M. Lu, Y. Zhao, L. J. Zhang, and U. J. Schoepf. "Dual-energy CT of the lung". In: *American Journal of Roentgenology* 199.5_supplement (2012), S40–S53.

[38] C. A. Coursey, R. C. Nelson, D. T. Boll, et al. "Dual-energy multidetector CT: how does it work, what can it tell us, and when can we use it in abdominopelvic imaging?" In: *Radiographics* 30.4 (2010), pages 1037–1055.

[39] M.-J. Kang, C. M. Park, C.-H. Lee, et al. "Dual-energy CT: clinical applications in various pulmonary diseases". In: *Radiographics* 30.3 (2010), pages 685–698.

[40] E. Hachulla, V. Gressin, L. Guillevin, et al. "Early detection of pulmonary arterial hypertension in systemic sclerosis: a French nationwide prospective multicenter study". In: *Arthritis & Rheumatism* 52.12 (2005), pages 3792–3800.

[41] R. D. Rudyanto, S. Kerkstra, E. M. Van Rikxoort, et al. "Comparing algorithms for automated vessel segmentation in computed tomography scans of the lung: the VESSEL12 study". In: *Medical image analysis* 18.7 (2014), pages 1217–1232.

[42] A. F. Frangi, W. J. Niessen, K. L. Vincken, and M. A. Viergever. "Multiscale vessel enhancement filtering". In: *Medical Image Computing and Computer-Assisted Intervention*. Springer, 1998, pages 130–137.

[43] Y. Sato, S. Nakajima, N. Shiraga, et al. "Three-dimensional multi-scale line filter for segmentation and visualization of curvilinear structures in medical images". In: *Medical image analysis* 2.2 (1998), pages 143–168.

[44] C. Xiao, M. Staring, D. Shamonin, et al. "A strain energy filter for 3D vessel enhancement with application to pulmonary CT images". In: *Medical image analysis* 15.1 (2011), pages 112–124.

[45] Y. Boykov and V. Kolmogorov. "An experimental comparison of min-cut/max-flow algorithms for energy minimization in vision". In: *Energy minimization methods in computer vision and pattern recognition*. Springer. 2001, pages 359–374.

[46] Y. Y. Boykov and M.-P. Jolly. "Interactive graph cuts for optimal boundary & region segmentation of objects in ND images". In: *Computer Vision, 2001. ICCV 2001. Proceedings. Eighth IEEE International Conference on*. Volume 1. IEEE. 2001, pages 105–112.

[47] Y. Boykov, O. Veksler, and R. Zabih. "Fast approximate energy minimization via graph cuts". In: *Pattern Analysis and Machine Intelligence, IEEE Transactions on* 23.11 (2001), pages 1222–1239.

[48] M. B. Salah, A. Mitiche, and I. B. Ayed. "Multiregion image segmentation by parametric kernel graph cuts". In: *Image Processing, IEEE Transactions on* 20.2 (2011), pages 545–557.

[49] B. Chen, Y. Sun, and S. H. Ong. "Liver Vessel Segmentation Using Graph Cuts with Quick Shift Initialization". In: *The 15th International Conference on Biomedical Engineering*. Springer. 2014, pages 188–191.

[50] C. Bauer, T. Pock, E. Sorantin, et al. "Segmentation of interwoven 3d tubular tree structures utilizing shape priors and graph cuts". In: *Medical image analysis* 14.2 (2010), pages 172–184.

[51] M. Freiman, N. Broide, M. Natanzon, et al. "Vessels-cut: a graph based approach to patient-specific carotid arteries modeling". In: *Modelling the Physiological Human*. Springer, 2009, pages 1–12.

[52] P. A. Yushkevich, J. Piven, H. C. Hazlett, et al. "User-guided 3D active contour segmentation of anatomical structures: significantly improved efficiency and reliability". In: *Neuroimage* 31.3 (2006), pages 1116–1128.

[53] D. Selle, B. Preim, A. Schenk, and H.-O. Peitgen. "Analysis of vasculature for liver surgical planning". In: *Medical Imaging, IEEE Transactions on* 21.11 (2002), pages 1344–1357.

[54] J. A. Barberà, A. Riverola, J. Roca, et al. "Pulmonary vascular abnormalities and ventilation-perfusion relationships in mild chronic obstructive pulmonary disease." In: *American Journal of Respiratory and Critical Care Medicine* 149.2 (Feb. 1994), pages 423–429.

[55] R. A. Pauwels, A. S. Buist, P. M. Calverley, et al. "Global Strategy for the Diagnosis, Management, and Prevention of Chronic Obstructive Pulmonary Disease". In: *American Journal of Respiratory and Critical Care Medicine* 163.5 (Apr. 2001), pages 1256–1276.

[56] R. Quarck, M. Wynants, A. Ronisz, et al. "Characterization of proximal pulmonary arterial cells from chronic thromboembolic pulmonary hypertension patients." In: *Respiratory research* 13.1 (Mar. 2012), page 27.

[57] Y. Suzuki, Y. Suzuki, T. Uto, et al. "Morphological changes in small pulmonary vessels are associated with severe acute exacerbation in chronic obstructive pulmonary disease". In: *International Journal of Chronic Obstructive Pulmonary Disease* 11 (June 2016), pages 1435–1445.

[58] F. Coste, G. Dournes, C. Dromer, et al. "CT evaluation of small pulmonary vessels area in patients with COPD with severe pulmonary hypertension". In: *Thorax* 71.9 (Sept. 2016), pages 830–837.

[59] Z. Zhai, M. Staring, M. K. Ninaber, et al. "Pulmonary Vascular Morphology Associated With Gas Exchange in Systemic Sclerosis Without Lung Fibrosis." In: *Journal of thoracic imaging* (2019).

[60] S. Matsuoka, G. R. Washko, M. T. Dransfield, et al. "Quantitative CT measurement of cross-sectional area of small pulmonary vessel in COPD: correlations with emphysema and airflow limitation". In: *Academic radiology* 17.1 (Jan. 2010), pages 93–99.

[61] K. Kubo, R.-L. Ge, T. Koizumi, et al. "Pulmonary artery remodeling modifies pulmonary hypertension during exercise in severe emphysema". In: *Respiration Physiology* 120.1 (Mar. 2000), pages 71–79.

[62] R. S. J. Estépar, G. L. Kinney, J. L. Black-Shinn, et al. "Computed Tomographic Measures of Pulmonary Vascular Morphology in Smokers and Their Clinical Implications". In: *American Journal of Respiratory and Critical Care Medicine* 188.2 (July 2013), pages 231–239.

[63] F. N. Rahaghi, J. Ross, M Agarwal, G González, et al. "Pulmonary Vascular Morphology as an Imaging Biomarker in Chronic Thromboembolic Pulmonary Hypertension". In: *Pulmonary Circulation* 6.1 (Mar. 2016), pages 70–81.

[64] R. S. J. Estépar, J. C. Ross, K. Russian, et al. "Computational vascular morphometry for the assessment of pulmonary vascular disease based on scale-space particles". In: *2012 9th IEEE International Symposium on Biomedical Imaging (ISBI)*. IEEE, May 2012, pages 1479–1482.

[65]   F. N. Rahaghi, C. E. Come, J. C. Ross, et al. "Morphologic Response of the Pulmonary Vasculature to Endoscopic Lung Volume Reduction". In: *Chronic Obstructive Pulmonary Diseases: Journal of the COPD Foundation* 2.3 (2015), pages 214–222.

[66]   M. Helmberger, M. Pienn, M. Urschler, et al. "Quantification of Tortuosity and Fractal Dimension of the Lung Vessels in Pulmonary Hypertension Patients". In: *PLoS ONE* 9.1 (Jan. 2014). Edited by G. Frati, e87515.

[67]   E. M. van Rikxoort and B. van Ginneken. "Automated segmentation of pulmonary structures in thoracic computed tomography scans: a review". In: *Physics in Medicine and Biology* 58.17 (Sept. 2013), R187–R220.

[68]   C. Xiao, M. Staring, D. Shamonin, et al. "A strain energy filter for 3D vessel enhancement with application to pulmonary CT images". In: *Medical Image Analysis* 15.1 (Feb. 2011), pages 112–124.

[69]   R. D. Rudyanto, S. Kerkstra, E. M. Van Rikxoort, et al. "Comparing algorithms for automated vessel segmentation in computed tomography scans of the lung: the VESSEL12 study". In: *Medical Image Analysis* 18.7 (Oct. 2014), pages 1217–1232.

[70]   A. F. Frangi, W. J. Niessen, K. L. Vincken, and M. A. Viergever. "Multiscale vessel enhancement filtering". In: *International Conference on Medical Image Computing and Computer-Assisted Intervention*. Springer, 1998, pages 130–137.

[71]   Y. Sato, S. Nakajima, N. Shiraga, et al. "Three-dimensional multi-scale line filter for segmentation and visualization of curvilinear structures in medical images". In: *Medical Image Analysis* 2.2 (June 1998), pages 143–168.

[72]   T. Jerman, F. Pernuš, B. Likar, and Ž. Špiclin. "Beyond Frangi: an improved multiscale vesselness filter". In: *Medical Imaging 2015: Image Processing*. Volume 9413. International Society for Optics and Photonics. 2015, 94132A.

[73]   E. van Dongen and B. van Ginneken. "Automatic segmentation of pulmonary vasculature in thoracic CT scans with local thresholding and airway wall removal". In: *2010 IEEE International Symposium on Biomedical Imaging: From Nano to Macro*. IEEE, 2010, pages 668–671.

[74]   Z. Zhai, M. Staring, and B. C. Stoel. "Lung vessel segmentation in CT images using graph-cuts". In: *Medical Imaging 2016: Image Processing*. Volume 9784. International Society for Optics and Photonics. 2016, 97842K.

[75]   L. A. DeWerd and M. Kissick. *The phantoms of medical and health physics*. Springer, 2014.

[76]   V. Filippou and C. Tsoumpas. "Recent advances on the development of phantoms using 3D printing for imaging with CT, MRI, PET, SPECT, and ultrasound". In: *Medical physics* 45.9 (2018), e740–e760.

[77]   W. G. O'dell, A. K. Gormaley, and D. A. Prida. "Validation of the Gatortail method for accurate sizing of pulmonary vessels from 3D medical images". In: *Medical Physics* 44.12 (Dec. 2017), pages 6314–6328.

[78]   D. Mitsouras, T. C. Lee, P. Liacouras, et al. "Three-dimensional printing of MRI-visible phantoms and MR image-guided therapy simulation". In: *Magnetic resonance in medicine* 77.2 (2017), pages 613–622.

[79]   S. Shen, H. Wang, Y. Xue, et al. "Freeform fabrication of tissue-simulating phantom for potential use of surgical planning in conjoined twins separation surgery". In: *Scientific reports* 7.1 (2017), page 11048.

[80]   M. Toepker, G. Euller, E. Unger, et al. "Stenosis quantification of coronary arteries in coronary vessel phantoms with second-generation dual-source CT: influence of measurement parameters and limitations". In: *American Journal of Roentgenology* 201.2 (2013), W227–W234.

[81]   M. B. Salah, A. Mitiche, and I. B. Ayed. "Multiregion Image Segmentation by Parametric Kernel Graph Cuts". In: *IEEE Transactions on Image Processing* 20.2 (Feb. 2011), pages 545–557.

[82]   Y. Boykov, O. Veksler, and R. Zabih. "Fast approximate energy minimization via graph cuts". In: *IEEE Transactions on Pattern Analysis and Machine Intelligence* 23.11 (2001), pages 1222–1239.

[83]   Y. Boykov and V. Kolmogorov. "An experimental comparison of min-cut/max-flow algorithms for energy minimization in vision". In: *IEEE Transactions on Pattern Analysis and Machine Intelligence* 26.9 (Sept. 2004), pages 1124–1137.

[84]   B. van Ginneken, W. Baggerman, and E. M. van Rikxoort. "Robust segmentation and anatomical labeling of the airway tree from thoracic CT scans". In: *International Conference on Medical Image Computing and Computer-Assisted Intervention*. Springer. 2008, pages 219–226.

[85]   E. Pompe, E. M. Van Rikxoort, O. M. Mets, et al. "Follow-up of CT-derived airway wall thickness: Correcting for changes in inspiration level improves reliability". In: *European Journal of Radiology* 85.11 (Nov. 2016), pages 2008–2013.

[86]   D. Selle, B. Preim, A. Schenk, and H.-O. Peitgen. "Analysis of vasculature for liver surgical planning". In: *IEEE Transactions on Medical Imaging* 21.11 (Nov. 2002), pages 1344–1357.

[87]   W. Dumouchel and F. O'Brien. "Integrating a robust option into a multiple regression computing environment". In: *Computing and graphics in statistics*. Springer-Verlag New York, Inc. 1992, pages 41–48.

[88]   E. R. Weibel and D. M. Gomez. "Architecture of the Human Lung: Use of quantitative methods establishes fundamental relations between size and number of lung structures". In: *Science* 137.3530 (Aug. 1962), pages 577–585.

[89]   E. R. Weibel. "What makes a good lung". In: *Swiss Med Wkly* 139.27-28 (2009), pages 375–386.

[90]   R. M. S. Joemai and J. Geleijns. "Assessment of structural similarity in CT using filtered backprojection and iterative reconstruction: a phantom study with 3D printed lung vessels". In: *The British Journal of Radiology* 90.1079 (Nov. 2017), page 20160519.

[91] I. Hernandez-Giron, J. M. den Harder, G. J. Streekstra, et al. "Development of a 3D printed anthropomorphic lung phantom for image quality assessment in CT". In: *Physica Medica* 57 (2019), pages 47–57.

[92] J. Meijs, A. A. Schouffoer, N. A. Marsan, et al. "Therapeutic and diagnostic outcomes of a standardised, comprehensive care pathway for patients with systemic sclerosis". In: *RMD Open* 2.1 (Mar. 2016), e000159.

[93] M. R. Miller, J. Hankinson, V Brusasco, et al. "Standardisation of spirometry". In: *European Respiratory Journal* 26.2 (2005), pages 319–338.

[94] B. L. Graham, V. Brusasco, F. Burgos, et al. "2017 ERS/ATS standards for single-breath carbon monoxide uptake in the lung". In: *European Respiratory Journal* 49.1 (Jan. 2017), page 1600016.

[95] S. Klein, M. Staring, K. Murphy, et al. "elastix: A Toolbox for Intensity-Based Medical Image Registration". In: *IEEE Transactions on Medical Imaging* 29.1 (Jan. 2010), pages 196–205.

[96] J. Solomon and E. Samei. "Quantum noise properties of CT images with anatomical textured backgrounds across reconstruction algorithms: FBP and SAFIRE". In: *Medical physics* 41.9 (2014).

[97] P. Nardelli, D. Jimenez-Carretero, D. Bermejo-Pelaez, et al. "Pulmonary Artery-Vein Classification in CT Images Using Deep Learning". In: *IEEE Transactions on Medical Imaging* 0062.c (2018), pages 1–1.

[98] C. Payer, M. Pienn, Z. Bálint, et al. "Automated integer programming based separation of arteries and veins from thoracic CT images". In: *Medical Image Analysis* 34 (Dec. 2016), pages 109–122.

[99] J.-P. Charbonnier, M. Brink, F. Ciompi, et al. "Automatic Pulmonary Artery-Vein Separation and Classification in Computed Tomography Using Tree Partitioning and Peripheral Vessel Matching". In: *IEEE Transactions on Medical Imaging* 35.3 (Mar. 2016), pages 882–892.

[100] N. S. Goh, R. K. Hoyles, C. P. Denton, et al. "Short-term pulmonary function trends are predictive of mortality in interstitial lung disease associated with systemic sclerosis". In: *Arthritis & Rheumatology* 69.8 (2017), pages 1670–1678.

[101] G. Bussone and L. Mouthon. "Interstitial lung disease in systemic sclerosis". In: *Autoimmunity Reviews* 10.5 (2011), pages 248 –255. URL: http://www.sciencedirect.com/science/article/pii/S1568997210002089.

[102] E. L. Herzog, A. Mathur, A. M. Tager, et al. "interstitial lung disease associated with systemic sclerosis and idiopathic pulmonary fibrosis: how similar and distinct?" In: *Arthritis & rheumatology* 66.8 (2014), pages 1967–1978.

[103] D. Manners, P. Wong, C. Murray, et al. "Correlation of ultra-low dose chest CT findings with physiologic measures of asbestosis". In: *European radiology* 27.8 (2017), pages 3485–3490.

[104] H. J. Kim, M. S. Brown, R. Elashoff, et al. "Quantitative texture-based assessment of one-year changes in fibrotic reticular patterns on HRCT in scleroderma lung disease treated with oral cyclophosphamide". In: *European radiology* 21.12 (2011), pages 2455–2465.

[105] J. B. West. *Respiratory physiology: the essentials*. Lippincott Williams & Wilkins, 2012.

[106] S. G. Martin, L.-P. Kronek, D. Valeyre, et al. "High-resolution computed tomography to differentiate chronic diffuse interstitial lung diseases with predominant ground-glass pattern using logical analysis of data". In: *European radiology* 20.6 (2010), pages 1297–1310.

[107] J. Meijs, A. A. Schouffoer, N. A. Marsan, et al. "A prediction model for progressive disease in systemic sclerosis". In: *RMD open* 1.1 (2015), e000113.

[108] B. J. Kircher, R. B. Himelman, and N. B. Schiller. "Noninvasive estimation of right atrial pressure from the inspiratory collapse of the inferior vena cava". In: *The American journal of cardiology* 66.4 (1990), pages 493–496.

[109] K. H. Yiu, M. K. Ninaber, L. J. Kroft, et al. "Impact of pulmonary fibrosis and elevated pulmonary pressures on right ventricular function in patients with systemic sclerosis". In: *Rheumatology* 55.3 (2015), pages 504–512.

[110] M. E. Bakker, M. K. Ninaber, J. Stolk, et al. "Lung Density and Pulmonary Artery Diameter are Predictors of Pulmonary Hypertension in Systemic Sclerosis". In: *Journal of thoracic imaging* 32.6 (2017), pages 391–397.

[111] Z. Zhai, M. Staring, and B. C. Stoel. "Lung vessel segmentation in CT images using graph-cuts". In: *Medical Imaging 2016: Image Processing*. Volume 9784. International Society for Optics and Photonics. 2016, 97842K.

[112] W. G. O'Dell, S. T. Govindarajan, A. Salgia, et al. "Traversing and labeling interconnected vascular tree structures from 3D medical images". In: *Medical Imaging 2014: Image Processing*. Volume 9034. International Society for Optics and Photonics. 2014, page 90343C.

[113] C. Terzano, V. Conti, A. Petroianni, et al. "Effect of postural variations on carbon monoxide diffusing capacity in healthy subjects and patients with chronic obstructive pulmonary disease". In: *Respiration* 77.1 (2009), pages 51–57.

[114] B. C. Stoel and J. Stolk. "Optimization and standardization of lung densitometry in the assessment of pulmonary emphysema". In: *Investigative radiology* 39.11 (2004), pages 681–688.

[115] P. H. Kitslaar, R. van't Klooster, M. Staring, et al. "Segmentation of branching vascular structures using adaptive subdivision surface fitting". In: *Medical Imaging 2015: Image Processing*. Volume 9413. International Society for Optics and Photonics. 2015, 94133Z.

[116] H. J. Reesink, M. N. van der Plas, N. E. Verhey, et al. "Six-minute walk distance as parameter of functional outcome after pulmonary endarterectomy for chronic thromboembolic pulmonary hypertension". In: *The Journal of thoracic and cardiovascular surgery* 133.2 (2007), pages 510–516.

[117] H. J. Reesink, I. I. Tulevski, J. T. Marcus, et al. "Brain natriuretic peptide as noninvasive marker of the severity of right ventricular dysfunction in chronic thromboembolic pulmonary hypertension". In: *The Annals of thoracic surgery* 84.2 (2007), pages 537–543.

[118] S. Ley, J. Ley-Zaporozhan, M. B. Pitton, et al. "Diagnostic performance of state-of-the-art imaging techniques for morphological assessment of vascular abnormalities in patients with chronic thromboembolic pulmonary hypertension (CTEPH)". In: *European radiology* 22.3 (2012), pages 607–616.

[119] R. Krissak, T. Henzler, M. Reichert, et al. "Enhanced visualization of lung vessels for diagnosis of pulmonary embolism using dual energy CT angiography". In: *Investigative radiology* 45.6 (2010), pages 341–346.

[120] F. Valentin. *Hurst's the Heart*. McGraw-Hill, 2008.

[121] M Staring, M. Bakker, J Stolk, et al. "Towards local progression estimation of pulmonary emphysema using CT". In: *Medical physics* 41.2 (2014).

[122] F. Meinel, A Graef, K. Thierfelder, et al. "Automated quantification of pulmonary perfused blood volume by dual-energy CTPA in chronic thromboembolic pulmonary hypertension". In: *RöFo-Fortschritte auf dem Gebiet der Röntgenstrahlen und der bildgebenden Verfahren*. Volume 186. 02. © Georg Thieme Verlag KG. 2014, pages 151–156.

[123] H. Koike, E. Sueyoshi, I. Sakamoto, et al. "Quantification of lung perfusion blood volume (lung PBV) by dual-energy CT in patients with chronic thromboembolic pulmonary hypertension (CTEPH) before and after balloon pulmonary angioplasty (BPA): preliminary results". In: *European journal of radiology* 85.9 (2016), pages 1607–1612.

[124] T. Inohara, T. Kawakami, M. Kataoka, et al. "Lesion morphological classification by OCT to predict therapeutic efficacy after balloon pulmonary angioplasty in CTEPH". In: *International journal of cardiology* 197 (2015), pages 23–25.

[125] F. Rahaghi, J. Ross, M Agarwal, et al. "Pulmonary vascular morphology as an imaging biomarker in chronic thromboembolic pulmonary hypertension". In: *Pulmonary circulation* 6.1 (2016), pages 70–81.

[126] A. Myronenko and X. Song. "Point set registration: Coherent point drift". In: *IEEE transactions on pattern analysis and machine intelligence* 32.12 (2010), pages 2262–2275.

[127] S. Ge, G. Fan, and M. Ding. "Non-rigid point set registration with global-local topology preservation". In: *Computer Vision and Pattern Recognition Workshops (CVPRW), 2014 IEEE Conference on*. IEEE. 2014, pages 245–251.

[128] B. J. Kirby. *Micro-and nanoscale fluid mechanics: transport in microfluidic devices*. Cambridge university press, 2010.

[129] L. K. Saul and S. T. Roweis. "An introduction to locally linear embedding". In: *unpublished. Available at: http://www. cs. toronto. edu/˜ roweis/lle/publications. html* (2000).

[130]   A. M. Pinzón, M. H. Hoyos, J.-C. Richard, et al. "A tree-matching algorithm: Application to airways in CT images of subjects with the acute respiratory distress syndrome". In: *Medical image analysis* 35 (2017), pages 101–115.

[131]   S. Klein, M. Staring, K. Murphy, et al. "Elastix: a toolbox for intensity-based medical image registration". In: *IEEE transactions on medical imaging* 29.1 (2010), pages 196–205.

Publications

Journal articles

Z. Zhai, H. Ota, M. Staring, J. Stolk, K. Sugimura, K. Takase, and B. C. Stoel. Treatment effect of balloon pulmonary angioplasty in chronic thromboembolic pulmonary hypertension quantified by automatic comparative imaging in computed tomography pulmonary angiography, *Investigative Radiology*, Volume 53(5), Page 286-292, 2018 May.

Z. Zhai, M. Staring, M. K. Ninaber, J. K. de Vries-Bouwstra, A. A. Schouffoer, L. J. Kroft, J. Stolk, and B. C. Stoel. Pulmonary Vascular Morphology Associated With Gas Exchange in Systemic Sclerosis Without Lung Fibrosis, *Journal of Thoracic Imaging*, Volume 34(6), Page 373-379, 2019 November.

Z. Zhai, M. Staring , I. Hernandez-Giron , W. J. H. Veldkamp , L. J Kroft , M. K Ninaber , B. C. Stoel. Automatic quantitative analysis of pulmonary vascular morphology in CT images, *Medical Physics*, Volume 46(9), Page 3985-3997, 2019 September.

S. Bayer, **Z. Zhai**, M. Strumia, X. Tong, Y. Gao, M. Staring, B. C. Stoel, R. Fahrig, A. Nabavi, A. Maier, N. Ravikumar. Registration of vascular structures using a hybrid mixture model, *International journal of computer assisted radiology and surgery*, Volume 14(9), Page 1507-1516, 2019 September.

International conference proceedings

Z. Zhai, M. Staring and B. C. Stoel. Lung vessel segmentation in CT images using graph-cuts, *International Society for Optics and Photonics Medical Imaging*, Volume 9784, Pages 97842k, 2016 March.

Z. Zhai, M. Staring, H. Ota, and B. C. Stoel. Pulmonary vessel tree matching for quantifying changes in vascular morphology, *International Conference on Medical Image Computing and Computer-Assisted Intervention* Page 517-524, Springer Cham, 2018 September.

Z. Zhai, M. Staring, X. Zhou, Q. Xie, X. Xiao, M. E. Bakker, L. J. Kroft, B. P.F. Lelieveldt, G. J.A.M. Boon, F. A. Klok, and B. C. Stoel. Linking convolutional neural networks with graph convolutional networks: application in pulmonary artery-vein separation, *Graph Learning in Medical Imaging, MICCAI (Shenzhen) workshop*, 2019 October.

Abstracts

Z. Zhai, H. Ota, M. Staring, J. Stolk, K. Sugimura, K. Takase, and B. C. Stoel. Treatment Effect of Balloon Pulmonary Angioplasty in CTEPH, Quantified by Automatic Comparative Imaging in CTPA, *Radiological Society of North America - RSNA*, 2017.

Acknowledgements

sharing the cutting-edge technologies and the group discussions. Patrick, Jeroen, Niels, Alexander and Oleh, thanks for your invitation for lunch every working day. Baldur, Evgeni, Thomas, Floris, Antonios, Ahmed and Arlin, thank you very much for your nice greetings. Thanks to all desk mates of mine, Gorkem, Nora, Baas and etc, who shared the 'student island' with me.

I would also like to give my thanks to colleagues in Rotterdam, Yuanyuan, Hua, Yao, Chaoping, Bo, Gokhan, Zahra; and colleagues in Leiden, Ling, Yingguang, Yuchuan, Shengnan, Zhuo, Qing, Xiaowu, Jingnan, Xinpei, Lu, Yuanbo and Chenghong. Thanks to my friend, Xiaoyu, Xiaoyao, Zhongwu Hannah, Kun, Yang, Quanchi, Gangqi and his wife Yan; and my ex-housemates Haoyu, and his wife Tianran, Renjiang, Guiying, Wangyang and Hui.

I would like to thanks my families. 感谢我的爸爸妈妈，对我支持和理解，感谢您们的无私的爱；感谢我的岳母，大哥，大嫂以及可爱的多多，谢谢您们的支持；感谢我的姑姑，姑父，舅舅，妹妹，姐姐，哥哥，感谢您们的帮助和支持。 Special thanks to my wife Ningning, you make me happy. You make me special, and you let me know what love is. Thank you for your love and selfless supports.

116

Curriculum Vitae

Zhiwei Zhai was born in Shandong, China in 1989. In 2008, he started his studying in the major of Information and Computing Science at Harbin Institute of Technology (Weihai) and obtained a Bachelor degree of Science in 2012. He obtained a 'top ten outstanding students' award (10/5000) and several 'national scholarship' awards. In 2012, he did a summer internship in Jinhe Company of Information and Technology (Weihai). At the same year, he began his master study in the major of Computer Science and Technology with an exemption. During the master study, he involved in the research of automatic detection and diagnosis of lung nodules based on CT images. In summer of 2013, he practiced in the Alibaba Company (Hangzhou) as an algorithm engineer. In 2014, he got his master degree of Engineering.

From September 2014, he started his PhD study in the Division of Image Processing (LKEB) under the Department of Radiology at Leiden University Medical Center in the Netherlands. His PhD project mainly focuses on pulmonary vessel analysis and quantification based on CT images, which results this thesis.

From September 2018, he works as a post-doctoral researcher in the LKEB, with the project of pulmonary artery-vein separation and quantification, based on deep learning and geometric deep learning.